

Laser nitriding of metals:

Influences of the ambient pressure and the pulse duration

Dissertation

zur Erlangung des Doktorgrades

der Mathematisch-Naturwissenschaften Fakultäten

der Georg-August-Universität zu Göttingen

vorgelegt von

Meng Han

aus Ruzhou, V.R. China

Göttingen 2001

D 7

Referent: Prof. Dr. K. P. Lieb

Korreferent: Prof. Dr. H. U. Krebs

Tag der mündlichen Prüfung: 17. 12. 2001

let there be light.....

Contents

Abstract	1
1 Introduction	3
1.1 Motivations	6
1.2 Thesis organization	7
2 Experimental Methods	9
2.1 Laser nitriding setup	9
2.2 Analysis of laser nitrated samples	12
2.2.1 Rutherford backscattering spectroscopy	13
2.2.2 Resonant nuclear reaction analysis	17
2.2.3 Mössbauer spectroscopy	19
2.2.4 X-ray diffraction	23
2.2.5 Characterization of surface properties	26
3 Influence of ambient nitrogen pressure on laser nitriding	27
3.1 Laser-metal interactions	27
3.2 Experimental findings	31
3.2.1 Nitrogen concentration depth profile	31
3.2.2 Phase analysis	38
3.2.3 Surface morphology	45
3.3 Discussion of laser plume dynamics	50

3.4	Summary	59
4	Influence of laser pulse duration on laser nitriding	61
4.1	Physics on different time scales	61
4.2	Description of pulsed laser types	63
4.3	Nitriding efficiency comparison	70
4.3.1	Nitrogen depth profile	70
4.3.2	Surface phase composition	72
4.4	Discussion of laser nitriding mechanisms	77
4.5	Laser nitriding of titanium	80
4.6	Summary	86
5	Thermal stability of laser produced iron/titanium nitrides	88
5.1	Iron/titanium nitrides phase evolution during annealing treatment . .	89
5.1.1	In vacuum environment	89
5.1.2	In air atmosphere	95
6	Conclusions and outlook	102
6.1	Conclusions	102
6.2	Outlook	104
	Bibliography	107

List of Figures

1-1	Fe-N phase diagram [1].	4
1-2	Schematic drawing of a ns excimer laser nitriding process.	7
2-1	Schematic drawing of the laser nitriding experimental setup.	10
2-2	Spatial intensity profile of the raw laser pulse of the Siemens XP2020 excimer laser ($a_0 = 55$ mm, $b_0 = 45$ mm), operated at 30 kV.	11
2-3	Spatial intensity profile of the homogenized laser pulse after the fly eye cylindrical microlens ($a = b = 5$ mm).	12
2-4	Schematic drawing of the Rutherford backscattering spectroscopy.	13
2-5	RBS measurment of the iron sample with Au marker layer [1]: (a) RBS spectra before and after laser irradiation ($H = 4\text{J}/\text{cm}^2$, $p_0 = 1$ bar), (b) Au concentration depth profiles derived by RUMP.	16
2-6	Schematic drawing of the resonant nuclear reaction analysis.	17
2-7	Energy splitting due to hyperfine electronic field gradient.	21
2-8	Energy splitting due to hyperfine magnet field.	21
2-9	5° GIXRD spectrum of excimer laser nitrided iron ($p_0 = 2$ bar).	24
3-1	Schematic diagram of the solid/liquid and vapor/liquid interfaces and the temperature profile in the near surface region during laser irradiation.	29

3-2	Nitrogen depth profiles of excimer laser nitrided iron after single pulse irradiation, the nitrogen pressures range from 0.05 bar to 10 bar. The insert shows the fitting of the nitrogen depth profile with the superposition of two exponential functions ($p_0 = 1$ bar).	32
3-3	Characteristic parameters of the nitrogen depth profiles after single pulse laser irradiation as the functions of the nitrogen pressure. . . .	33
3-4	Nitrogen depth profile evolution in the ^{15}N isotopic multipulse experiments ($p_0 = 1$ bar).	36
3-5	Nitrogen depth profiles of laser nitrided iron and stainless steel at different nitrogen pressures from 0.2 bar to 10 bar.	39
3-6	(a) GIXRD spectra of laser nitrided stainless steel at different nitrogen pressures. (b) Diffraction spectrum as the superposition of two subspectra with different lattice constants.	40
3-7	CEMS spectra of (a) virgin stainless steel, (b) stainless steel nitrided at 0.5 bar, (c) at 1 bar and (d) at 4.5 bar.	41
3-8	Comparison of the mean nitrogen concentrations in stainless steel deduced from CEMS, GIXRD and RNRA measurements, respectively. . .	44
3-9	GIXRD spectra of laser nitrided iron at different nitrogen pressures.	45
3-10	(a) CEMS spectra of laser nitrided iron at the nitrogen pressure of 4.5 bar and 0.5 bar, respectively. (b) Phase composition deduced from CEMS spectra.	46
3-11	Surface profiles of stainless steel after excimer laser irradiation (64 pulses) at different nitrogen pressures.	47
3-12	Schematic illustration of the piston effect induced by the plasma pressure p_{plasma} and the recoil pressure of surface evaporation p_r [102]. . .	48
3-13	Material redistribution deduced from the surface profiles after laser treatment. The curves are plotted to guide the eye.	49
3-14	Schematic diagram of laser supported combustion wave.	53

3-15	Schematic drawing of the spatial structure of laser plume.	56
3-16	Schematic drawing of the plasma pressure as a function of time. . . .	57
4-1	Schematic drawing of the photon energy dissipation mechanisms on different time scales [102].	62
4-2	Schematic drawing of the laser-plasma-metal system under the irradi- ations of different pulsed lasers.	63
4-3	Energy levels and lasing mechanism of a XeCl excimer laser.	64
4-4	Time structure of FEL macro- and micropulses in Jefferson Lab. . . .	68
4-5	Chirped laser amplification technique for ultra short fs Ti:sapphire laser.	69
4-6	Nitrogen depth profiles of excimer laser, Nd-YAG laser, FEL and Ti:sapphire laser nitrided iron samples ($p_0 = 1$ bar). One sample is also treated by Nd-YAG laser in air.	71
4-7	GIXRD spectra of excimer laser (in N_2) and Nd-YAG laser (in air) nitrided iron samples.	72
4-8	GIXRD spectra of FEL and Ti:sapphire laser nitrided iron samples. . . .	73
4-9	CEMS spectra of excimer laser (in N_2) and Nd-YAG laser (in air) nitrided iron samples.	74
4-10	CEMS spectra of FEL and Ti:sapphire laser nitrided iron samples. . . .	75
4-11	Surface hardness profiles of different types of pulsed laser nitrided iron and titanium.	77
4-12	Simulation of the surface temperature and the molten depth of iron as the functions of time (Excimer laser: $H = 4$ J/cm ² , Nd-YAG laser: H $= 2.34$ J/cm ²).	78
4-13	Nitrogen concentration profiles of excimer laser nitrided titanium at different nitrogen pressures.	81
4-14	Comparison of normalized yield of γ -ray in RNRA among FEL nitrided titanium, iron and stainless steel.	82

4-15	GIXRD spectra of excimer laser and FEL nitrated titanium.	83
4-16	GIXRD spectrum of FEL nitrated titanium and rocking curve measurement of TiN <200> peak for excimer laser and FEL nitrated titanium.	84
4-17	Surface hardness profile of excimer laser and FEL nitrated titanium compared to virgin titanium.	85
5-1	Nitrogen depth profiles for excimer laser nitrated iron and stainless steel annealed in vacuum (2 hours at each temperature).	90
5-2	CEMS spectra of excimer laser irradiated iron and stainless steel with subspectra.	91
5-3	(a) Phase composition of excimer laser nitrated iron and (b) subspectral area fraction of excimer laser nitrated stainless steel revealed by CEMS as functions of annealing temperature.	92
5-4	GIXRD spectra of excimer laser nitrated iron (a) and stainless steel (b) annealed in vacuum.	93
5-5	Microhardness measurement of excimer laser nitrated iron and stainless steel annealed in vacuum.	94
5-6	Nitrogen depth profiles for excimer laser nitrated iron and stainless steel annealed in air.	96
5-7	GIXRD spectra of excimer laser nitrated stainless steel annealed in air.	97
5-8	GIXRD spectra of excimer laser nitrated iron annealed in air.	98
5-9	(a) Phase composition of excimer laser nitrated iron annealed in air as revealed by CEMS analysis; (b) CEMS spectrum of the excimer laser nitrated iron annealed in air at 673 K.	99
5-10	The evolution of the nitrogen depth profile of excimer laser nitrated titanium (annealed in air at 873 K for 2 hours) and Ti:sapphire laser nitrated iron (2 years in RT air atmosphere).	100

6-1 Schematic drawing of *in situ* experimental configurations with the aim of probing plasma properties and metal surface state during laser nitriding process. 105

6-2 Schematic drawing of the idea of multi-beam pulsed laser nitriding for optimal laser-metal energy coupling. 106

Symbols

a, b, c	lattice constants
a_0, b_0	dimensions of the raw unfocused laser beam
a, b	dimensions of focused laser beam
A	area of laser spot
α	absorption coefficient
B_{hf}	magnetic hyperfine field
V_S	sound velocity
c	light constant
C_l, C_s	specific heat capacity of liquid or solid metal
C_N	nitrogen concentration
C_L, C_S	long range, short range component of nitrogen depth profile
$C_L(0), C_S(0)$	coefficient of long and short range component of nitrogen profile
D	diffusion constant
δ	isomer shift (IS)
e	elementary charge
eQ	electric quadrupole moment of a nucleus
E, E_R	energy, resonance energy
E_0	electric field amplitude
E_p	proton energy
E_P	laser pulse energy
E_γ	γ -ray energy
E_p	laser pulse energy
E_i, E_f	initial and final energy of particle
E_{in}, E_{out}	energy of particle entering or leaving the material
E_q, E_m	energy shift induced by hyperfine electric gradient, magnetic field

E_R	recoil energy
E_M, E_V	laser energy distribution between melting and evaporation
dE/dx	stopping power
ϵ_{det}	detector efficiency
ϵ_0	dielectric constant
η	asymmetry parameter of the electric field gradient
ΔE_q	quadrupole splitting
f_p	pulse frequency
f	focal length
f_D	Debye-Waller factor
F, F_{max}	force, maximum force
g_N	Landé factor
γ	damping coefficient
γ	adiabatic coefficient of laser plume
γ_s	adiabatic coefficient of shocked gas
Γ	full width at half maximum (FWHM)
Γ^H	Heisenberg natural line width
h	planck constant
h_{plasma}, h_{shock}	enthalpy of laser plasma or shocked nitrogen gas
H	laser energy density
I_0	incident laser intensity
I_V, I_C, I_D	threshold intensity of evaporation, LSC wave, LSD wave
I_a	laser intensity absorbed by the laser plasma
I_p	laser intensity after passing the laser plasma
k	kinetic factor
K_S, K_l	thermal conductivity of solid or molten metal
k_B	Boltzmann constant

L_L, L_S	long, short range nitrogen diffusion length
L_l, L_v	latent heat of per unit volume of the liquid, vapor
λ	wavelength of radiation
m	mass
M	total nitrogen amount
m,n	meandering parameters (n \times m)
m_I	magnetic quantum number
M, M_a, M_t, M_p	atomic mass, mass number, mass number of target and projectile
μ	magnetic dipole moment
μ_N	Bohr magneton
n	number of laser pulses hitting the metal surface
N_T	total number of evaporated particles
ω, ω_p	angular frequency, plasma frequency
Ω	solid angle
P	Polarization of free electrons
p_0	ambient nitrogen pressure
$p_{plasma}, p_{shock}, p_r$	plasma pressure, shocked gas pressure, recoil pressure
P_6^n	probability of ^{57}Fe site in austenite with n nitrogen neighbors
p_v	vapor pressure
Ψ_A, Ψ_S	electron wave function for absorber and source
r	laser spot radius
R	reflectivity
R	radius of laser plume
R_e, R_g	radius of electron cloud around nucleus at excited and ground state
ρ_0	ambient nitrogen gas density
$\rho_{plasma}, \rho_{shock}$	density of plasma, density of shocked gas
σ	cross section

t, t_v, t_m, t_c	time, evaporation time, melting time, plasma-metal coupling time
τ	laser pulse duration
τ_{2D}, τ_Z	lateral, vertical relaxation time of laser plasma
S_{sl}, S_{vl}	position of solid/liquid, vapor/liquid interface
S_N	solubility of nitrogen
T, T_m, T_b, T_{plasma}	temperature, melting , boiling, plasma temperature
T_l, T_s	temperature of metal in liquid, solid state
θ	angle
Θ	Debye temperature
u_{shock}	shock wave velocity
u_{piston}	piston velocity
v	Doppler velocity
V	volume of laser plume
$V, V_{xx}, V_{yy}, V_{zz}$	electrical potential, tensor of electric field gradient, principal values
V_+, V_-	amount of redistributed material outside and inside the laser spot
V_{piston}	amount of redistributed material due to piston effect
V_v	amount of redistributed material due to evaporation
V_W	velocity of laser absorption wave
W	dimensionless particle velocity
x	nitrogen distribution depth
x_{ev}	evaporation depth
$X Y Z$	dimensional of laser plume
Y	yield or normalized yield
z	position of free electron
Z, Z_p, Z_t	atomic number, atomic number of projectile, target particle

Abstract

Laser nitriding of metals such as iron, stainless steel, aluminum or titanium is an interesting phenomenon both in physics and industry. On a time scale of hundreds nanoseconds, high intensity pulsed laser irradiation ($I_0 \approx 10^8 \text{ W/cm}^2$) in ambient nitrogen atmosphere transforms the surface of metals to micron thick metal nitride layer, which greatly improve the metal surface mechanical properties. Since laser plume dynamics and incident pulsed laser are two most crucial factors determining the laser nitriding efficiency, the experiments focus on the influences of the ambient nitrogen pressure and the pulsed laser duration on laser nitriding. It is found that as nitrogen pressure increases from 0.05 bar to 2 bar, the nitriding efficiency increases rapidly, then remains nearly constant up to 10 bar. The optimal nitrogen pressure window lies between 2 and 3 bar. The nitrogen pressure series clearly demonstrated the transition from laser ablation to nitrogen diffusion dominated regime. The characteristic parameters of the nitrogen profile are extracted and qualitatively interpreted based on the laser supported combustion model.

The investigations of the influence of the pulse duration on laser nitriding with nanosecond (ns) excimer and Nd-YAG laser, picosecond (ps) free electron laser and femtosecond (fs) Ti:sapphire lasers, have revealed that ns laser is superior compared to ps or fs laser. Nitrogen diffusion in molten metals is believed to be the primary mechanism of efficient laser nitriding. The competing process resulting in the depletion of nitrogen is a degassing process, which is confirmed by the annealing experiments and the comparison between iron and titanium nitrided by free electron laser. Due to

the enhanced laser-metal thermal coupling induced by the laser plasma, the nitriding efficiency is more or less independent of the wavelength of the incident laser. The thermal stability of laser produced metal nitrides and the iron nitride phase evolution are investigated in a series of annealing treatments conducted in vacuum and air. The results revealed that 973 K is the maximum temperature for laser produced iron nitrides, above 973 K, nitrogen escapes from the surface due to degassing. Titanium nitride is more stable than iron nitrides, which makes titanium an excellent candidate for effective laser nitriding.

Chapter 1

Introduction

Iron is the most abundant metal on earth and one of the best known materials in society. It was discovered in prehistoric times and even gave its name to a period of time in history: the iron age. However, the main drawback of iron is that the pure iron is soft and fragile to chemical corrosion and mechanical erosion.

Surface modification of metal, such as applying a iron nitride layer at the surface [2, 3, 4] is the widely used methods to improve the surface's mechanical and tribological properties, such as corrosion and erosion resistance. The enhancement of corrosion or wear resistance is generally ascribed to the iron nitride layer itself, while the increase in hardness is supposed to be improved by a diffusion zone below the nitride layer.

As indicated by the Fe-N phase diagram [5, 6] in Figure 1-1, the Fe-N system consists of several solid solutions of N (α , γ , ϵ), stable chemical compounds (γ' - Fe_4N , ζ - Fe_2N) and metastable phases (α' -martensite, α'' - Fe_{16}N_2) [7]. The nitrogen content in the solid solution of b.c.c. α -Fe phase is below 0.4 at.% at $T = 873$ K. The b.c.c. martensitic α' - Fe(N) can be regarded as a supersaturated α - Fe, with a maximum solution of 10 at.%. The f.c.c. γ - Fe(N) is stable above 873 K, it can also be retained at room temperature after fast cooling. N can be dissolved in γ - Fe(N) to a maximum of 10.3 at.%. Recently, the b.c.t. α'' - Fe_{16}N_2 has attracted

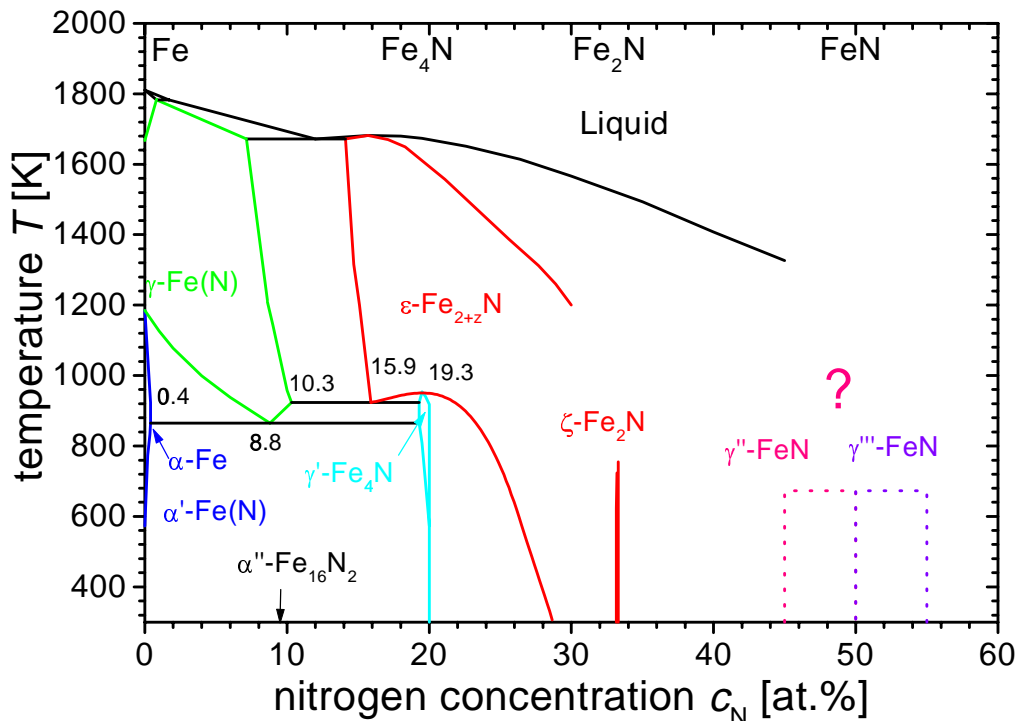


Figure 1-1: Fe-N phase diagram [1].

interests due to its giant magnetic moment, in which the N atoms are on an ordered sublattice. The f.c.c. γ' - Fe₄N phase is nearly a stoichiometric line compound with a narrow nitrogen concentration range between 19.3 at.% and 20.0 at.%. The ϵ - Fe_{2+x}N phase has an h.c.p. structure and nitrogen is soluble between 15 at.% and 33 at.%, depending strongly on temperature. The ϵ and γ' phases are favorable phases for coatings, because of their good tribological and corrosion resistance properties. At 33 at.% an orthorhombic ζ - Fe₂N line compound phase is formed. Recently, increasing number of reports have been published about a new FeN compound prepared by sputtering methods. As illustrated in Figure 1-1, the FeN compound could have two phases, one is γ'' - FeN with ZnS structure, the other is NaCl structure γ''' - FeN. However, the question of the stability and exact structure of these FeN phases is still open [36, 131].

Traditional nitriding methods include gas nitriding, salt bath nitriding, ion im-

plantation and plasma nitriding. Gas nitriding is the most widely used industrial process. An ammonia or ammonia/hydrogen mixture is used to increase nitrogen activity, as described by the following equation:



However, normally the gas nitriding process is conducted at high temperatures of $500 \sim 600^\circ\text{C}$, the formed iron nitride layers are porous due to the thermal instability of the iron nitrides with respect to iron and nitrogen gas.

Salt bath nitriding is similar to the gas nitriding, except that the nitrogen activity comes from liquid salt baths containing reactive nitrogen such as cyanides or cyanates.

Ion implantation utilizes a beam of nitrogen ions in the energy range of 40 keV - 1 MeV range, which penetrate into the iron surface to form an iron nitride layer at low temperature [8, 9, 10, 11, 12, 13, 14]. It is possible to synthesize a continuous, micron thick nitride layer by a two stage MeV nitrogen ion implantation process [15, 95].

Recently, plasma nitriding [16, 17, 18] has become a promising nitriding method. Compared to traditional gas or salt bath nitriding, plasma nitriding imparts a hard wear resistant surface without brittleness, galling or spalling. Furthermore, plasma nitriding affects less the surface finish of the product. Salt bath and gas nitriding, which use ammonia and phosphate for activation, will roughen the polished surface. Plasma nitriding also provides a higher surface hardness and maintains materials core properties due to lower nitriding temperatures. Finally, plasma nitriding is environment friendly because a non-toxic ($H_2 + N_2$) mixture is used. Traditional gas and salt bath nitriding use toxic gases, salts or ammonia which are hard to control and harmful to the workers and the environment.

1.1 Motivations

The traditional nitriding methods [19, 20] of iron normally need a quite high temperature and long treatment time. The samples with complicated shape or with the neighboring undesirable region composed of material sensitive to heat, would be difficult to be treated [25]. Finding alternative methods in these situations would be an interesting challenge. In the past two decades, pulsed lasers have attracted lots of attentions. First, short and ultra short pulsed lasers open a new door to the ps and fs ultra fast processes [21], even chemical reaction can be monitored. On the other hand, the ultra high power density provided by short pulsed laser triggers various dynamical processes, such as laser ablation (LA), pulsed laser deposition (PLD) of thin films, laser cutting and micro-machining [22], particularly, in the field of PLD [23, 24]. PLD is able to deposit nearly all of the materials, including ceramics or superconductor materials, with the advantages of simple experimental setup, high deposition rates, flexible tuning of the laser energy or wavelength and avoid of intersource pollution which is a general problem in CVD or MBE. Generally, high intensity pulsed laser and low ambient pressure below 10^{-3} mbar are two fundamental conditions for PLD to ensure the production of laser plume and transport of ablated material from the target to the substrate. If the gas pressure increases to air atmosphere, the expansion speed of the laser plume is reduced and the hot region of the laser plume confines longer time above the target due to the shock wave induced by the ambient gas. For ns XeCl laser, inside the laser plume, the plume temperature (T) can reach thousands degrees at a pressure (p) of hundreds bars, which resemble the environment of traditional plasma nitriding, but on a different spatial and time scale, as illustrated in Figure 1-2. The nitrogen is incorporated into the molten metal by nitrogen diffusion and laser plasma condensing. The laser plume located in the laser focused region lasts typically around nanoseconds. Even materials sensitive to heat could be treated [1, 26, 27, 28].

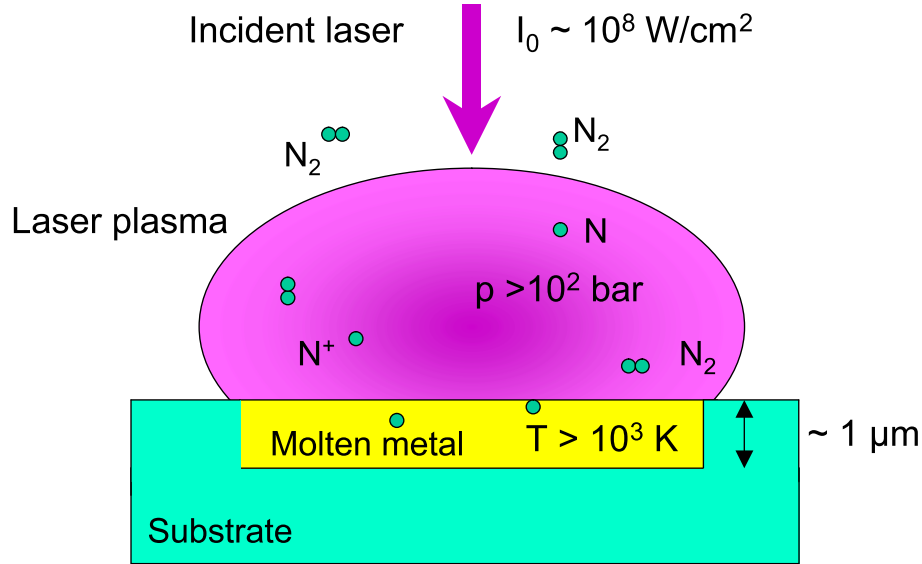


Figure 1-2: Schematic drawing of a ns excimer laser nitriding process.

1.2 Thesis organization

Understanding the fundamental mechanisms of pulsed laser nitriding of metals is the primary goal of this work. Since a high nitrogen pressure ($p_0 \approx 1 \text{ bar}$) and a high laser intensity ($I_0 \approx 10^8 \text{ W/cm}^2$) are the most crucial conditions for laser nitriding, the investigations focus on the influences of the ambient nitrogen environment and the incident pulsed laser on the nitriding process, more specifically, the ambient nitrogen pressure series and the pulsed laser series, which are expected to lead to a better understanding of laser plume dynamics and laser nitriding mechanisms. The optimal configuration of the most efficient laser nitriding is also of interest. The specific metals under investigations are iron, stainless steel and titanium, which are most popularly used metals but with the drawbacks of poor erosion and corrosion resistance.

After a introduction to the gas, plasma and laser nitriding techniques, the remainder of the thesis is organized as follows. Chapter 2 gives a brief description of the laser nitriding experimental setup, adopted in most of the nitriding experiments. Further, Chapter 2 describes the analysis methods in this thesis, particularly the ion beam and nuclear physics analysis technique, such as Rutherford Backscattering

Spectroscopy (RBS), Nuclear Reaction Analysis (NRA) and Mössbauer spectroscopy, which are excellent techniques to carry out an analysis of the thin film composition and phases.

In chapter 3 the ambient nitrogen gas pressure dependence of laser nitriding is discussed, with the emphasis on the laser plume dynamics. The investigated nitrogen pressures range from 0.05 bar to 10 bar. Through isotopic experiments with enriched ^{15}N , the evolution of the nitrogen depth profile with the number of laser pulses is derived. A qualitative interpretation of the characteristic parameters of the nitrogen depth profile based on laser plume dynamics is included. The phase composition and surface profiles at different nitrogen pressures are also briefly discussed.

Chapter 4 describes the laser pulse duration dependence of laser nitriding, with the concentration on the laser nitriding mechanisms. Comparisons of nitrogen concentration depth profiles, surface phase compositions and hardness among ns UV excimer laser, IR Nd-YAG laser, ps free electron laser and fs Ti:sapphire laser nitrated iron and titanium are presented. Together with a thermal simulation, the primary laser nitriding mechanism is determined. Also elucidated are two competing processes determining the nitriding efficiency.

The thermal stability of laser produced iron, stainless steel or titanium nitrides is presented in chapter 5. A series of annealing experiments are conducted in vacuum and air. The phase diagrams of laser irradiated iron or stainless steel at different temperatures and the maximum temperature for future applications are derived.

Chapter 6 summarizes the conclusions of the thesis and gives an outlook for the future researches.

Chapter 2

Experimental Methods

2.1 Laser nitriding setup

The experimental set up of laser nitriding is illustrated schematically in Figure 2-1: High power pulsed laser employed in the experiment is a XeCl excimer laser, a Nd-YAG laser, a fs Ti:sapphire laser or a free electron laser. After the optical unit, the pulsed laser beam is focused on the metal surface inside the laser nitriding chamber, which is filled with nitrogen gas with a purity of 99.999% after evacuation to a pressure below 10^{-6} mbar.

Since most of our experiments are conducted with excimer laser, the detailed description of this experimental setup is given. If other pulsed lasers are used, only minor modifications of this system are needed.

The raw beam of excimer laser was focused onto the metal sample through a $f = 200$ mm concave quartz lens. The laser energy density H is determined by the focus area and the pulse energy E_p :

$$H = \frac{E_P}{a_0 b_0} \frac{f^2}{d^2} \quad (2.1)$$

where d is the distance between sample surface and focusing plane, a_0 , b_0 describe the dimension of the laser beam aperture.

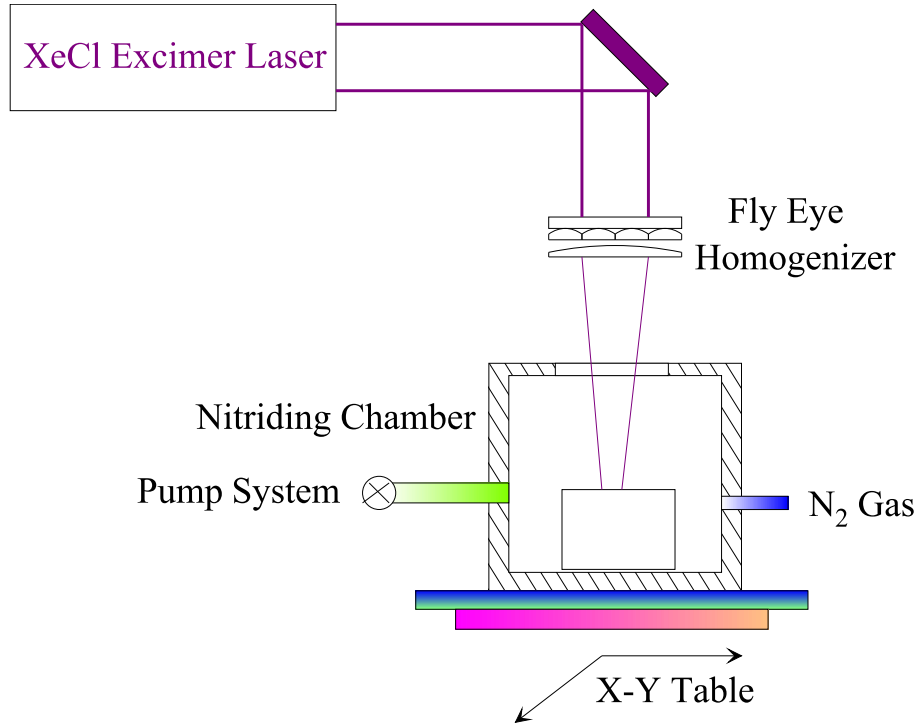


Figure 2-1: Schematic drawing of the laser nitriding experimental setup.

The energy of single pulse E_P is measured by a pyroelectric joulemeter with a black ceramic absorption layer (SpectroLas/GenTec with measuring head PEM50K). E_P equals the mean value of 10 measurements results with same optical path as real sample treatment, with an error below 4%. The size of the laser spot on the samples was measured by the black area of the photoactive paper after laser irradiation. The spatial intensity profile of the raw beam of XP2020 XeCl excimer laser was obtained from a CCD device, which is shown in Figure 2-2. The energy density of the raw beam laser varies significantly over the spot, with maximum value in the centre and lower intensities around the borders. Such kind of inhomogeneity would result in rough sample surface and thermal instability during the laser nitriding process. In order to homogenize the incident raw laser beam, a 5×5 fly eye cylindrical microlens (10 mm width and 50 mm length) array with a focal length of 50 mm is employed. There is exactly one position (45 mm from the focusing lens) where the laser beam redistribute its spatial energy density and produce a homogeneous top-hat flat energy profile, as

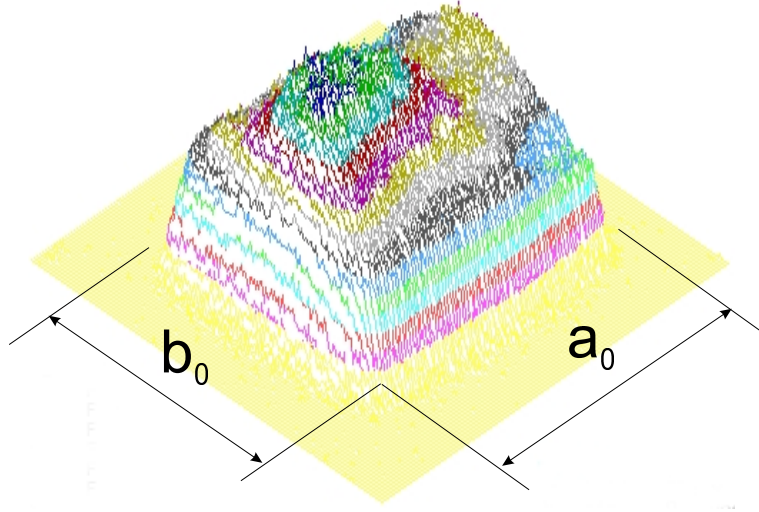


Figure 2-2: Spatial intensity profile of the raw laser pulse of the Siemens XP2020 excimer laser ($a_0 = 55$ mm, $b_0 = 45$ mm), operated at 30 kV.

indicated in Figure 2-3.

The whole laser nitriding chamber was evacuated with rotation pump and molecular pump until 10^{-6} mbar, then filled with nitrogen gas N_2 to desired pressure p_0 . The chamber was designed to withstand a pressure of 10 bar so the pressure region between 10^{-6} mbar and 10 bar was available for the laser treatment.

In order to make large area treatment maintaining nice surface morphology, the nitriding chamber was mounted on a numerical controlled X-Y table, which allows programmed movement of the chamber. The same area of the metal surface was irradiated $m \times n$ times by moving the sample in x direction with each step of $\Delta = a/m$ and in Y direction with step of $\Delta = b/n$, where a, b describes the size of the laser spot. Therefore the whole metal surface can be treated with the desired number of pulses.

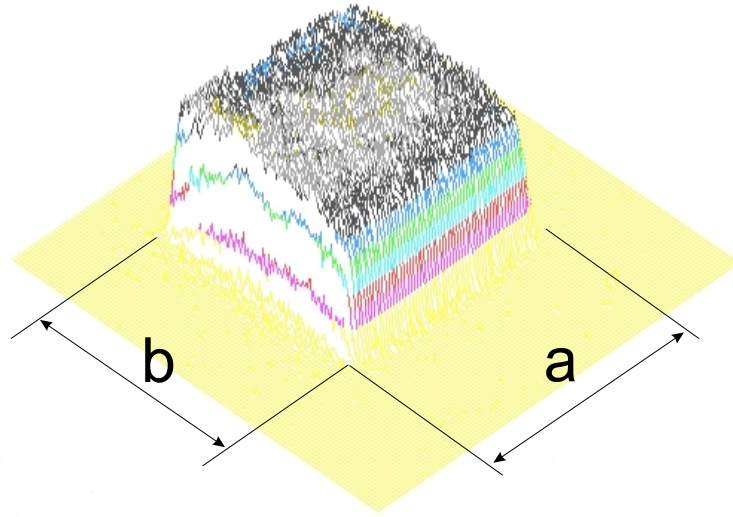


Figure 2-3: Spatial intensity profile of the homogenized laser pulse after the fly eye cylindrical microlens ($a = b = 5$ mm).

2.2 Analysis of laser nitrided samples

Due to the technical difficulties involved in the ultra fast process, most investigation of the laser nitriding process concentrate on the analysis of the nitrided metals after laser treatment instead of the *in situ* monitoring of the nitriding process.

For laser nitrided metals, nitrogen depth profile and surface phase composition are important informations to characterize the nitriding efficiency. Surface morphology and microhardness are crucial properties for real applications.

Besides the widely used surface processing applications such as ion implantation and ion beam mixing, ion beam technique also highlights itself in the field of non destructive analysis of elemental compositions and depth profiles with high sensibility and resolution [38, 39, 40]. Ion beam analysis is based either on the Coulomb interaction between the ion beam and the target nuclei or the nuclear reaction between the incident energetic ion and target nuclei. The former leads to the development of the Rutherford Backscattering Spectroscopy (RBS), the latter forms the basis for Nuclear Reaction Analysis (NRA). They are described in detail as follows. All of the ion beam analyses were performed at the 530 keV heavy ion implanter IONAS in

Göttingen [41].

2.2.1 Rutherford backscattering spectroscopy

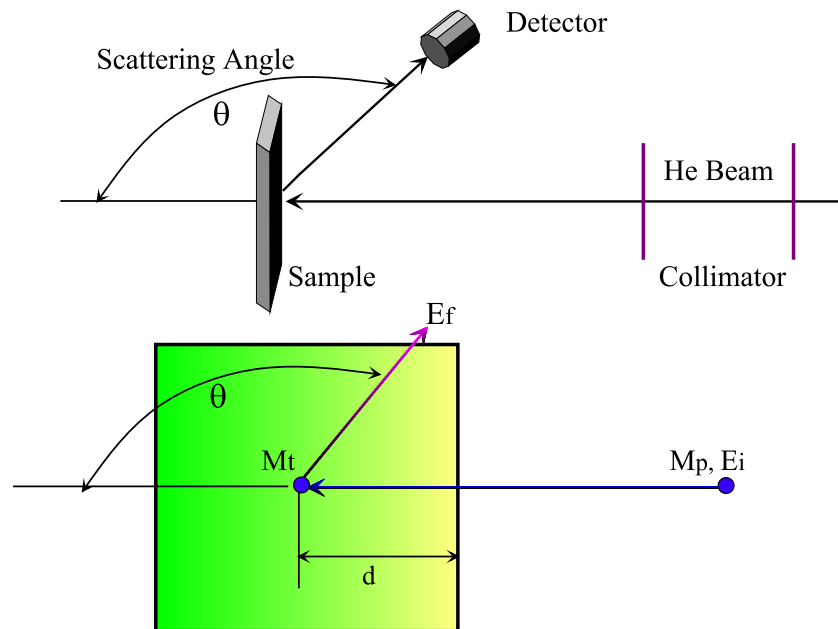


Figure 2-4: Schematic drawing of the Rutherford backscattering spectroscopy.

RBS [42] is based on a simple phenomenon: the elastic collisions between beam particles and the nuclei of the target at energies well below the Coulomb barrier. There are three basic factors which determine the energy spectrum of RBS. A schematic drawing of RBS is illustrated in Figure 2-4.

Initially, backscattering results in an energy change due to collision kinematics. The spectrum is further altered by energy loss of incoming and backscattered particles emerged from below the target's surface. The intensity of backscattered particles reflects the concentration of target atoms. Therefore, a single RBS spectrum contains the information of target's atom masses, their concentrations, and depth profiles.

From an analytical point of view, RBS compatible materials are heavy thin films on lighter substrate materials. Heavier thin film give high intensity RBS signals free

of background. Normally, RBS measurement of light element are more difficult due to low signal to background ratio.

However, for a number of important light elements (carbon, nitrogen, oxygen), a special technique - elastic resonance scattering can be used to boost sensitivity. Such measurements are done at specific resonance energies at which the backscattering yield from the light element greatly exceeds standard RBS yields.

The RBS yield depends on the number of target atoms encountered by the penetrating particles along their path. For single-crystal target materials, the incoming beam direction can be aligned with one of the major crystallographic axes of the substrate. At such conditions, called channeling, the backscattering yield drastically reduces. Channeling provides information on the crystallinity of the target as well as determining whether an impurity atom occupies a substitutional lattice location.

In a typical RBS spectrum, the abscissa corresponds to the energy of the backscattered He ions E_f , which is determined by the incidence energy, the scattering angle and the energy loss of He ions when they travel through the target materials. The backscattering process when approximated by the Rutherford point charge model is illustrated in Figure 2-4:

$$E_f = k \cdot (E_i - \Delta E_{in}) - \Delta E_{out} = k \cdot \left(E_i - \int_0^d \frac{dE}{dx}(x) dx \right) - \int_0^d \frac{dE}{dx}(x) \frac{dx}{\cos(\theta)} \quad (2.2)$$

where E_i is the He ion incidence energy, d denotes the depth where the backscattering happens, θ is the backscattering angle and k is the kinematic factor.

$$k = \frac{\left[M_p \cos(\theta) + \sqrt{M_t^2 - M_p^2 \sin^2(\theta)} \right]^2}{(M_p + M_t)^2} \quad (2.3)$$

where M_p and M_t are the masses of the incident He ion and target nuclei, respectively.

The stopping power dE/dx or energy loss of the incident ions depends on ion

velocity and the charge state of ion and target atom. If the ion velocity is below the Bohr velocity $v_0 = e^2/h$, the nuclear stopping is the dominant mechanism contributing to the energy loss, since ion tends to be neutralized by electron capture. For high energetic ion or $v \gg v_0$, some electrons are stripped from the ions, and the electronic stopping dominates. The energy range for our RBS and NRA belongs to the nuclear stopping dominated regime. The stopping power has been theoretically investigated [39, 43] as well as experimentally measured and phenomenologically parameterized for many incident ions and targets combinations [44, 45, 46, 47, 48].

The Y-axis of the RBS spectrum corresponds to the yield of the He ions or the intensity of the RBS spectrum, which is determined by the differential cross section at the specific backscattering angle θ where the detector is located, as illustrated in equation 2.4 and 2.5:

$$\frac{d\sigma}{d\Omega} = \left(\frac{Z_p Z_t e^2}{16\pi\epsilon_0 E_i} \right)^2 \frac{4}{\sin^4(\theta)} \frac{[\sqrt{1 - [(M_p/M_t)\sin(\theta)]^2} + \cos(\theta)]^2}{\sqrt{(M_p/M_t)\sin(\theta)]^2}} \quad (2.4)$$

Equation 2.5 can be simplified for $M_p \ll M_t$ to the well known Rutherford relation

$$\frac{d\sigma}{d\Omega} = \left(\frac{Z_p Z_t e^2}{16\pi\epsilon_0 E_i} \right)^2 \frac{1}{\sin^4(\theta/2)} \quad (2.5)$$

All of these most important equations and parameterization of the cross section, stopping power and energy straggling are included in the various of software packages for RBS analysis, such as RUMP [49, 50], GISA [51], IBA [52], RBX [53] and SIMNRA [54] or WinNDF. RUMP is adopted for all of the RBS analysis in this work.

Looking a real example, in order to trace the material transport and intermixing, a 10 nm thick Au marker layer was deposited at a depth of 60 nm in an iron sample. The sample was prepared by electron-gun evaporation and then irradiated with excimer laser pulses (raw beam). The RBS spectra and Au concentration profiles deduced from RUMP are illustrated in Figure 2-5. Before the laser irradiation, the Au layer

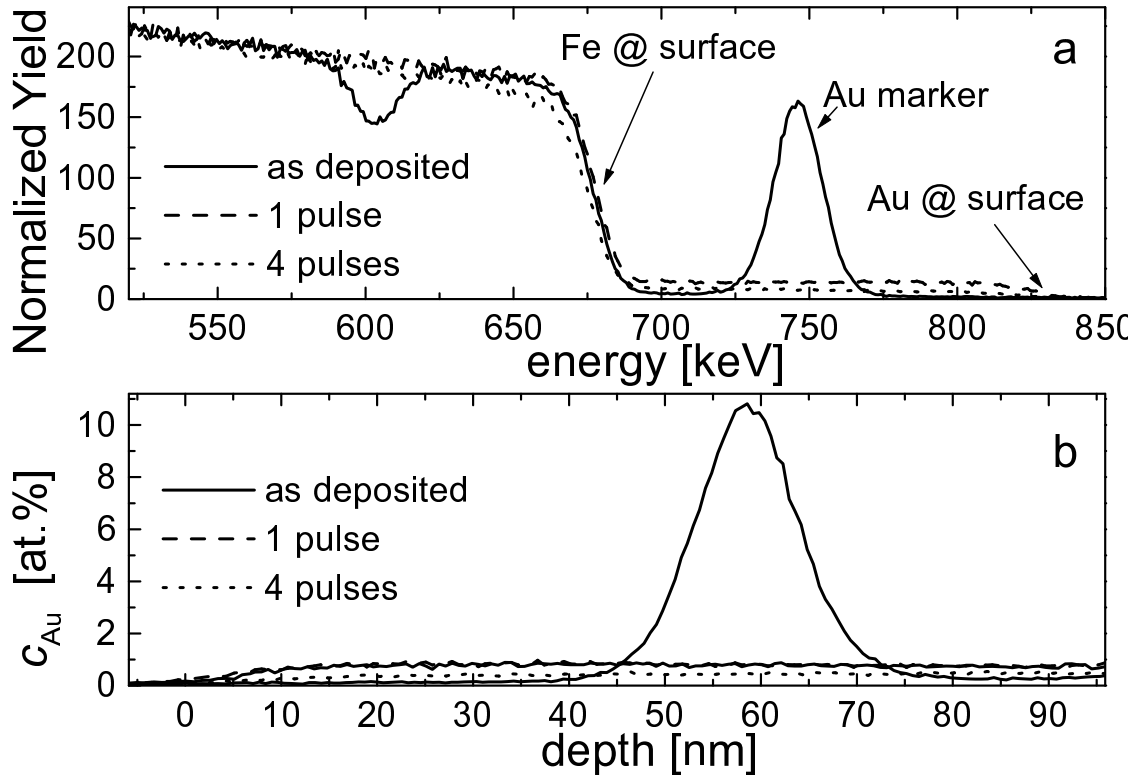


Figure 2-5: RBS measurement of the iron sample with Au marker layer [1]: (a) RBS spectra before and after laser irradiation ($H = 4\text{J}/\text{cm}^2$, $p_0 = 1$ bar), (b) Au concentration depth profiles derived by RUMP.

could be fitted with a narrow Gaussian profile. After the laser treatment, it turned into a nearly constant distribution down to the visible depth of about 400 nm. Even a single laser pulse had produced a complete intermixing of the Au with iron. According to Schaaf's simulation [1], a pure diffusion of Au would cause a broaden of the Au layer width from 9(1) nm to 62 nm for a single laser shot, an additional convection flow must be taken into account to explain the complete intermixing of Au and iron. Since the convection flow is difficult to analyze, in most of the following experiments a homogeneous beam is used to suppress the convection flow.

2.2.2 Resonant nuclear reaction analysis

Resonant Nuclear Reaction Analysis (RNRA) is a general category of ion beam analysis techniques involving a nuclear reaction between a target nucleus and an incident particle. When the energy of the incident particle exceeds the Coulomb barrier, i.e., the potential barrier caused by charge repulsion, the nuclear reaction can occur. The reaction generally results in the emission of reaction products, such as an α particle or a γ ray. The theory of the RNRA are well discussed by Maurel [58, 59] and Vickridge [60].

The common reactions employed for microanalysis are (d, α), (d, p), (p, α) for particle detection and (p, $\alpha \gamma$) for γ ray detection. RNRA with γ ray detection are particularly useful for light elements such as ^{13}C , ^{15}N , ^{18}O , ^{19}F , ^{22}Ne , ^{23}Na , ^{24}Mg , ^{27}Al , ^{29}Si and ^{30}Si [55, 56, 57] depth profiling.

Osipowicz, Lieb and Brüssermann's experimental work [61] indicated that the resonance energy of $^{15}\text{N}(p, \alpha\gamma)^{12}\text{C}$ is $E_R = 429.57(9)$ keV with a resonance width of $\Gamma = 124(17)$ eV. The narrow resonance width and high cross section ($\sigma = 300$ mb) make $^{15}\text{N}(p, \alpha\gamma)^{12}\text{C}$ an ideal reaction for nitrogen profiling [63, 64, 65].

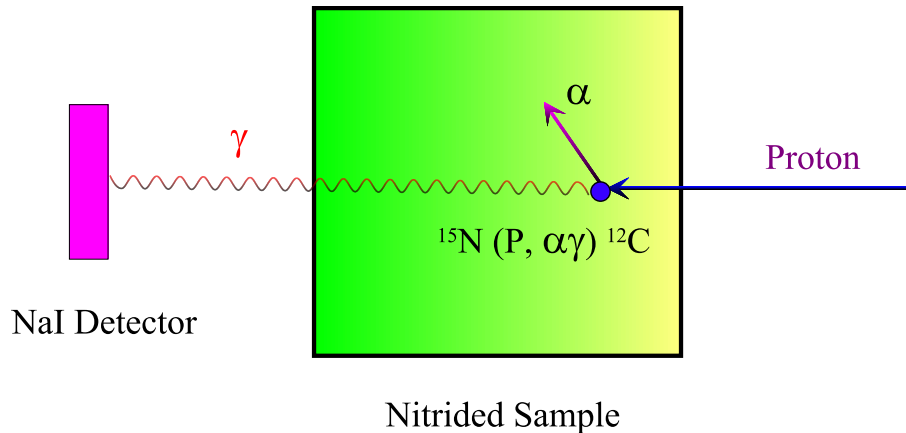


Figure 2-6: Schematic drawing of the resonant nuclear reaction analysis.

The principal of the RNRA with $^{15}\text{N}(p, \alpha\gamma)^{12}\text{C}$ reaction is illustrated in Figure 2-6. The 4.43 MeV γ -ray ($2^+ \rightarrow 0^+$) in ^{12}C is emitted only after the resonant reaction,

when the incident proton energy is higher than the threshold energy of 430 keV, its signal is proportional to the nitrogen atoms concentration. Quantitatively, the yield of the γ ray is given by:

$$Y(E_b) = \epsilon_{det}\Omega N_p \int_0^\infty \int_0^\infty \int_0^\infty C_N(x)g(E_b, E)f(E, E', x)\sigma(E')dE'dEdx \quad (2.6)$$

where ϵ_{det} is the detector efficiency, Ω is the detector solid angle and N_p is the number of incident protons, $C_N(x)$ is the concentration profile of the nitrogen atoms. $g(E_b, E)$ describes the energy distribution of the incident protons. In equation 2.6, $\sigma(E')$ and $f(E, E', x)$ are the two most important factors: $\sigma(E')$ is the resonance cross section at the proton energy E' . $f(E, E', x)$ corresponds to the possibility of finding a proton with the initial energy of E , after penetrating a depth of x , still maintains the energy of E' .

From equation 2.6, the γ yield is determined by the nitrogen depth profile $C_N(x)$ and proton incidence energy. Through an deconvolution inverse procedure, the nitrogen concentration profile could be derived. The simplified approach to determine the nitrogen content C_N in the compound of A_mB_n is described by equation 2.7.

$$C_N = \frac{C_{st}Y\epsilon_B}{Y_{st}\epsilon_{st} + C_{st}Y(\epsilon_B - \epsilon_A)} \quad (2.7)$$

where ϵ_A and ϵ_B describe the stopping power of pure A and B material respectively, ϵ_{st} is the stopping power of standard or calibration sample with known nitrogen concentration of C_{st} . Y and Y_{st} correspond to the γ yield of compound A_mB_n and calibration sample. The stopping power of compound is approximated with the Bragg rule [62].

The analyzing depth of the nitrogen profile is determined by

$$x(E_i) = x(E_{i-1}) + \frac{2(E_i - E_{i-1})}{\epsilon(E_i) + \epsilon(E_{i-1})} \quad (2.8)$$

with the assumption of constant stopping power within the small depth step. The depth can be converted from at/cm^2 to nm if the density is known.

Actually, the energy straggling of the incident protons, the initial beam energy spread of the accelerator and the Doppler broadening have to be taken into account. All these effects are included in a computer programme WinRNRA which automatically fits the nitrogen depth profile to the experimental γ yield [66], the minimization of the $\chi^2 = \Sigma(Y_{sim}(E_i) - Y_{meas}(E_i))^2$ is done by Levenberg-Marquardt least square methods [67], where Y_{sim} and Y_{meas} correspond to the simulated and experimental γ yield respectively.

In details, RNRA is conducted with the well defined proton beam of IONAS [41], the available maximum proton energy limits the analysis depth to below 500 nm. During the measurement the sample was cooled by liquid nitrogen to avoid sample changes due to diffusion or anneal effect induced by the analyzing proton beam of 0.5 μ A. The diameter of the proton beam is between 1 and 3 mm. The γ spectra were collected with a 12 cm long NaI detector having a diameter of 16 cm, its efficiency ϵ_{det} for determination of the absolute nitrogen concentration was calibrated by stoichiometric TiN standard samples prepared by RF magnetron sputtering [68]. The homogeneous nitrogen concentration of calibration sample is determined by RBS.

2.2.3 Mössbauer spectroscopy

Conversion Electron Mössbauer Spectroscopy (CEMS) [69, 70] is based on the discovery of Mössbauer effect [71, 72, 73], or in other words, the phenomenon of recoil free resonant emission and absorption of nuclear γ -radiation.

When emits or absorbs a γ ray, a free atom will recoil with an energy determined by the conservation of energy and momentum between the nucleus and γ ray.

$$E_R = \frac{E_\gamma^2}{2Mc^2} = 1.95 \cdot 10^{-3} eV \quad (2.9)$$

comparing to the Heisenberg natural line width:

$$\Gamma^H = \frac{h}{\tau} = 4.66 \cdot 10^{-6} eV \quad (2.10)$$

It is evident that the transition lines of emission and absorption are separated by $2E_R \approx 10^6 \Gamma$, thus out of resonance.

The most important point of Mössbauer effect is that: when an atom is bounded in a lattice, the whole lattice will take the recoil energy, thus the mass of the single nucleus in equation 2.9 is replaced by the mass of the crystal, which is typically about 10^{20} times larger than single atom. By this way, the transitional recoil energy of the crystal only amounts to a negligible fraction of the natural line width Γ^H , now the nucleus γ ray system can be in resonance.

From quantum mechanics, the probability of the recoil free emission or absorption is determined by temperature T and Debye temperature Θ_D :

$$f(T) = \exp \left\{ -\frac{3E_R}{2k_B\Theta_D} \left[1 + 4\left(\frac{T}{\Theta_D}\right)^2 \int_0^{\frac{\Theta_D}{T}} \frac{x}{e^x - 1} dx \right] \right\} \quad (2.11)$$

Recoil free absorption and emission enable Mössbauer spectroscopy to be an excellent hyperfine analysis method with extremely high energy resolution. Due to the interaction between probe nuclei (^{57}Fe atoms in our case) and the hyperfine fields, such as an electric field gradient or a magnetic field, the energy level of probe nuclei shift by a typical value of around 10^{-5} eV, which is invisible to normal γ ray analysis methods except for Mössbauer spectroscopy with natural linewidth energy resolution.

The energy shift E_D was scanned by placing emitter and absorber in different solids and moving them relative to each other, as described by:

$$E_D = E_\gamma \left(1 + \frac{v}{c}\right) \quad (2.12)$$

which corresponds to the Doppler shift of the photon frequency, v is the relative velocity of emitter and absorber.

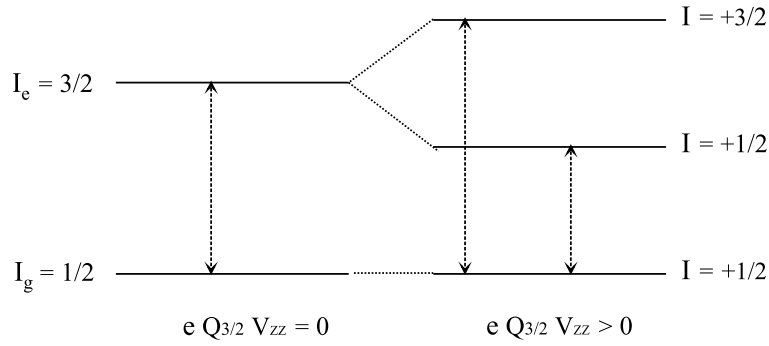


Figure 2-7: Energy splitting due to hyperfine electronic field gradient.

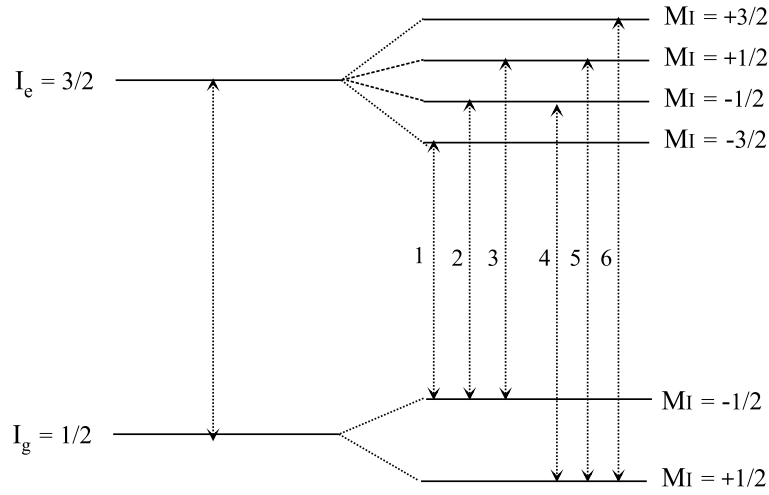


Figure 2-8: Energy splitting due to hyperfine magnet field.

CEMS is extremely sensitive to the local hyperfine field. The energy shift between the nuclear energy level of source and absorber ΔE could be divided into three components.

$$\Delta E = \delta + E_q + E_m \quad (2.13)$$

where δ is the electrical monopole interaction between the nuclear charge Z_e and the electron density at the nucleus, which is determined by

$$\delta = \frac{2}{5} \pi Z e^2 [|\Psi_A(0)|^2 - |\Psi_S(0)|^2] [R_e^2 - R_g^2] \quad (2.14)$$

In equation 2.14, $e|\Psi_S(0)|^2$ and $e|\Psi_A(0)|^2$ give the electron density at the nucleus of source (S) and absorber(A). R_e and R_g are the radius of the electron cloud around the nucleus, where the subscripts e and g refer to excited and ground state.

The last two terms in equation 2.13 are due to the interaction of the nucleus with local electronic field gradient(EFG) and magnet field B.

As illustrated in Figure 2-7 and Figure 2-8, the energy splitting E_q and E_m induced by the electric and magnetic hyperfine fields are determined by

$$E_q = \frac{eQV_{zz}}{4I(2I-1)}[3M_I^2 - I(I+1)]\sqrt{1 + \frac{1}{3}\eta^2} \quad (2.15)$$

and

$$E_m = -g_N\mu_N BM_I \quad (2.16)$$

where I is the spin of the nucleus, m_I is the magnetic quantum number. The EFG asymmetry parameter η is given in term of the EFG tensor (V = electrical potential)

$$\eta = \frac{V_{xx} - V_{yy}}{V_{zz}} \quad (2.17)$$

In a CEMS spectrum of a ^{57}Fe containing sample, ΔE determines the position of the resonance absorption peak, which is unique for a certain hyperfine field environment or a specific iron nitride phase in the case of laser nitriding of iron. The ability of the Mössbauer spectroscopy to distinguish different iron nitride phases is outstanding, since the iron nitrides differ very much in their hyperfine parameters.

To collect the resonant absorption signal, one possible experimental setup is to measure the absorption spectrum of the emitted γ - ray. However, for a thick sample, this method doesn't work due to the limited penetration depth. There are several alternative experimental setup based on the products of internal conversion process, such as conversion electrons, Auger electrons or conversion X-rays. If the conversion electrons emitted from the excited nuclei are detected, this kind of spectroscopy is

called Conversion Electron Mössbauer spectroscopy (CEMS). One brilliant advantage of CEMS is the short penetration depth of conversion electron ($\approx 150 \text{ nm}$), which favors CEMS for surface layer analysis. Similarly, due to the deeper penetration depth of conversion x-rays ($\approx 10 - 30 \mu\text{m}$ in iron), conversion x-ray Mössbauer spectroscopy (CXMS) provides a good supplement to CEMS.

The Mössbauer spectra in our investigations were taken at room temperature, using a simultaneous trip-radiation Mössbauer spectrometer [74] with a $^{57}\text{Co}/\text{Rh}$ source ($\approx 400\text{MBq}$) and a constant acceleration drive. The conversion and Auger electrons were detected in a He/CH_4 gas-flow proportional counter, the information depth being around 150 nm. The spectra were stored in a multichannel scaler with 1024 channels [75]. After measurement, the spectra were fitted with a least-squares routine by superimposing Lorentzian lines [76]. Velocity calibration was performed at room temperature with a $25 \mu\text{m}$ α - Fe foil, to which all isomer shift are related.

2.2.4 X-ray diffraction

Only after the discovery of X-rays by Wilhelm Röntgen in 1895, the analysis of the crystalline structure and phase composition of bulk materials become possible [77, 78, 79]. In this work, most of the X-Ray Diffraction(XRD) experiments were conducted with the geometry of the Grazing angle Incidence (GIXRD). The main reasons are two-folded: Firstly, the typical pulsed laser modified region is within the depth of $1 \mu\text{m}$, where GIXRD reveals more information than other diffraction geometries. Secondly, because of the rapid cooling rate involved in the pulsed laser nitriding, polycrystalline is almost always the predominant structure for laser produced metal nitrides. With GIXRD, all diffraction peaks of crystallized phase are guaranteed to be resolved in a single spectrum. GIXRD is also the best way to trace the phase ratio evolution as a function of temperature, pressure or other variables.

With 5° grazing incidence angle, the penetration depth is around 750 nm for pure iron, which enable GIXRD an ideal methods to investigate the surface properties,

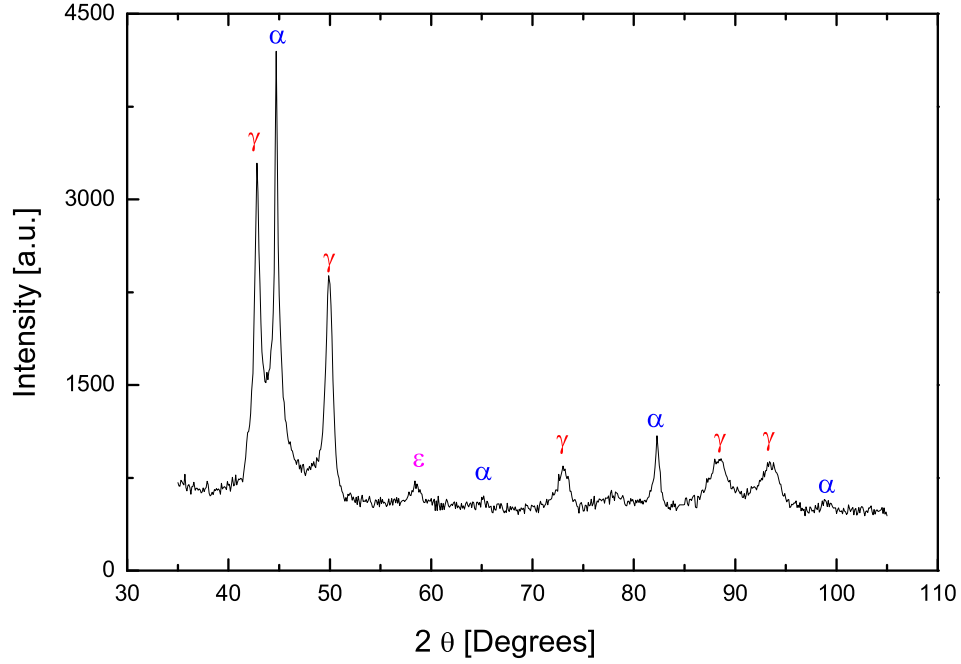


Figure 2-9: 5° GIXRD spectrum of excimer laser nitrided iron ($p_0 = 2$ bar).

such as surface phase composition, mean crystallite size and lattice strain. Figure 2-9 shows the GIXRD spectrum of an excimer laser nitrided iron sample at 2 bar. The dominant iron nitride phases such as γ - Fe(N) and ϵ - Fe_{2+x}N can be clearly distinguished from the virgin α -Fe substrate.

The lattice spacing parameter is determined by the Bragg law

$$n\lambda = 2d\sin\theta \quad (2.18)$$

For cubic structure such as α -Fe or TiN,

$$d = \frac{d_0}{\sqrt{h^2 + k^2 + l^2}} \quad (2.19)$$

where h, k, l are the Miller indexes.

From each diffraction peak a lattice spacing parameter d_0 could be calculated.

The accuracy of d_0 is determined by the accuracy of θ and λ . Although there are different sources of systematic errors, the predominant source of error come from the displacement of specimen from the diffractometer axis, which produces an error to the lattice spacing defined by:

$$\frac{\delta d_0}{d_0} = -\frac{D}{R_d} \cos\theta \tan\theta \quad (2.20)$$

where D is the horizontal displacement of the specimen from the diffractometer axis and R_d is the distance from specimen to the detector. The systematic error of d_0 is 0 as θ is 90° , where the true lattice spacing parameter could be deduced. The real approach is plot the d_0 as the linear function of $\cos\theta \tan\theta$ (Nelson - Riley Plot), linear extrapolation to $\cos\theta \tan\theta = 0$ gives a lattice spacing which takes the systematic errors in consideration.

From GIXRD spectrum, the crystallite grain size and lattice stain could also be determined from the x-ray diffraction peak broadening. Scherrer has derived an expression relating the x-ray diffraction peaks width to crystallite size:

$$B_{crystallite} = \frac{k_x \lambda}{L \cos\theta} \quad (2.21)$$

where λ is the wavelength of incidence x-ray, θ is the Bragg angle, L is the average crystallite size in a direction of the scattering vector, k_x is a constant varying between 0.89 and 1.309 for cubic materials, the assumption that $k_x = 1.0$ is generally justifiable since the precision of crystallite size analysis by this methods is, at best, about 10%.

A broadening of the diffraction peaks can also be induced by lattice strain, according to the following relationship

$$B_{strain} = \eta \tan\theta \quad (2.22)$$

where η is the strain in the material.

The width B_r , the peak width after subtracting the instrument broadening, can

now be considered as the sum of widths due to small crystallite size and lattice strain

$$B_r = B_{crystallite} + B_{strain} = \frac{k_x \lambda}{L \cos \theta} + \eta \tan \theta \quad (2.23)$$

$$B_r \cos \theta = \frac{k_x \lambda}{L} + \eta \sin \theta \quad (2.24)$$

If $B_r \cos \theta$ is plotted against $\sin \theta$, we get a straight line (Williamson-Hall plot) [80], after linear regression, the crystallite size L and lattice strain η would be determined.

In this thesis, all XRD spectra were taken with a Bruker AXS D8 advance diffractometer employing Cu K_α radiation ($\lambda = 1.54095 \text{ \AA}$).

2.2.5 Characterization of surface properties

A primary motivation for laser nitriding is to improve the surface hardness by iron nitrides or other ceramics. After the laser treatment, the surface hardness is investigated by nanoindentation hardness measurements [90], A diamond indenter (Vickers diamond, a square based pyramid with opening angle of 136°) indents into the surface according to the applying force F . The force is gradually increased from 0 to F , then return to 0 continuously. The universal hardness HU (N/mm^2) or GPa) is defined as the ratio of the force F and the area A , where the Vickers diamond is in contact with the material surface:

$$HU = \frac{F}{A(h)} \quad (2.25)$$

The surface profile of laser nitrided samples was measured by a DEKTAK³ST profilometer, which uses a $2.5 \mu\text{m}$ diameter diamond tip and a load of 10 mg. The resolution of the surface roughness could reach 1 nm.

Chapter 3

Influence of ambient nitrogen pressure on laser nitriding

3.1 Laser-metal interactions

From a microscopic point of view, absorption of the incident laser at a metal surface can be described as the response of the free electron of the metal to an oscillating electromagnetic wave [101]. If the field oscillates at a frequency ω , the free electrons will oscillate at the same frequency, the phase and amplitude of the oscillation is determined by the damping force on the electron as described by the following equation:

$$m \frac{d^2 z}{dt^2} + m\gamma \frac{dz}{dt} = -eE_0 e^{-i\omega t} \quad (3.1)$$

where m and e denote the mass and charge of the free electron at the position z , E_0 is the amplitude of the electric field and the damping coefficient is denoted as γ . The solution of equation 3.1 is in the oscillating form as:

$$z(t) = \frac{e}{m} \frac{1}{\omega^2 + i\gamma\omega} E_0 e^{-i\omega t} \quad (3.2)$$

For a sample with N free electrons, the motion of the electron resulting in an oscillating polarization:

$$P(t) = -\frac{Ne^2}{m} \frac{1}{\omega^2 + i\gamma\omega} E_0 e^{-i\omega t} = \epsilon_0 \chi_e E(t) \quad (3.3)$$

Then the free electron contribution to the dielectric constant ϵ can be deduced:

$$\epsilon(\omega) = 1 - \frac{Ne^2}{m\epsilon_0} \frac{1}{\omega^2 + i\gamma\omega} = \epsilon'(\omega) + i\epsilon''(\omega) \quad (3.4)$$

If the damping force of the free electrons is negligible: $\gamma \ll \omega$, the imaginary part of the free electron contribution can be neglected and the real part becomes

$$\epsilon'(\omega) = 1 - \frac{Ne^2}{m\epsilon_0} \frac{1}{\omega^2} = 1 - \frac{\omega_P^2}{\omega^2} \quad (3.5)$$

where ω_P is called the plasma frequency. For $\omega \ll \omega_P$, the dielectric constant $\epsilon'(\omega)$ becomes negative and the index of refraction is purely imaginary resulting in a strong attenuation of the electromagnetic wave. The free electrons act like a high pass filter: above the plasma frequency the metal is transparent, below the plasma frequency total reflection occurs.

From a macroscopic point of view, the bulk response of materials to laser light is described by a heat conduction equation [103]. Because the laser spot size (\approx mm) is much larger than the thermal diffusion length ($\approx \mu\text{m}$ for excimer laser), a one dimensional heat conduction model is adopted to determine the temperature profile. The temperature at depth x is given by [103]

$$\rho_i(T)C_i(T)\frac{\partial T_i(x,t)}{\partial t} = \frac{\partial}{\partial x} \left(K_i(T)\frac{\partial T_i(x,t)}{\partial x} \right) + I_p(t) [1 - R(T)] \exp[-\alpha(T)x] \quad (3.6)$$

where T denotes the temperature at the time of t which starts from the initial laser irradiation on the surface. The subscript i describes either the solid (s) or liquid (l)

phase. The thermal properties of the bulk material are described by a temperature dependent density ρ , a thermal heat capacity C and thermal conductivity K . The last item in equation 3.6 corresponds to the energy source from the laser irradiation. $I_p(t)$ is the time dependent laser intensity after passing the laser-produced plasma or plume. The temperature dependent parameter R describes the surface reflectivity and α is the absorption coefficient in the solid or liquid phase of the bulk material.

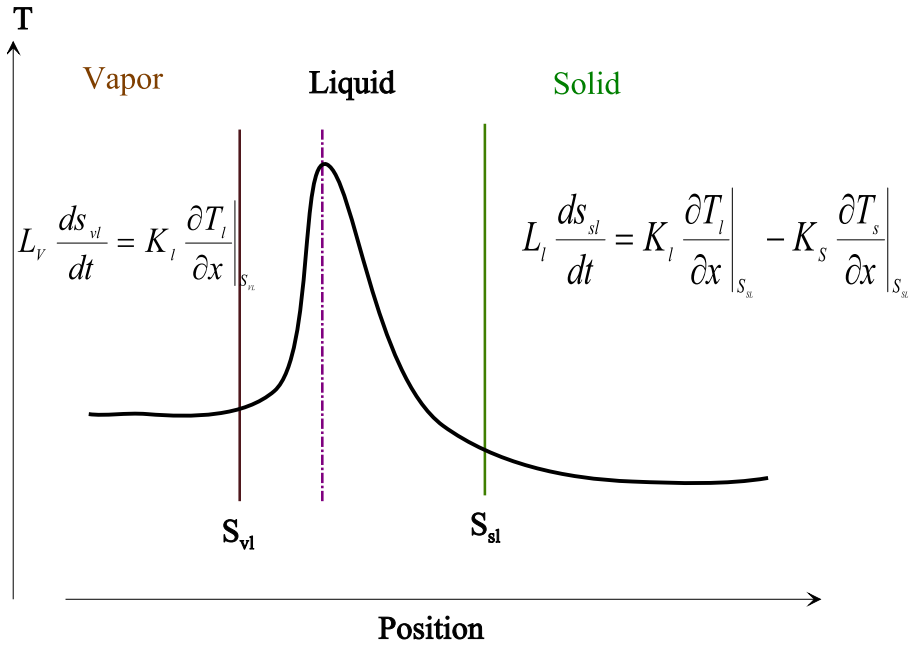


Figure 3-1: Schematic diagram of the solid/liquid and vapor/liquid interfaces and the temperature profile in the near surface region during laser irradiation.

The propagations of the vapor/liquid and solid/liquid phase fronts are determined by the thermal gradients in the vapor/liquid and solid/liquid interface. The position of the solid-liquid interface (S_{sl}) is defined by:

$$-K_s \frac{\partial T_s}{\partial x} \Big|_{x=S_{sl}} + K_l \frac{\partial T_l}{\partial x} \Big|_{x=S_{sl}} = L_l \frac{dS_{sl}}{dt} \quad (3.7)$$

where K_s and K_l are the thermal conductivity of the solid and liquid phase, L_l/L_v is the latent heat per unit volume of the liquid/vapor.

Similarly, the vapor/liquid front at the position S_{vl} is given by:

$$-K_l \frac{\partial T_l}{\partial x} \Big|_{x=S_{vl}} = L_v \frac{dS_{vl}}{dt} \quad (3.8)$$

A schematic drawing of the temperature profile in the near surface region is illustrated in Figure 3-1. As described in equation 3.7 and 3.8, both the vaporization and bulk diffusion process are temperature gradient driven, but in opposite directions. They compete with each other for the energy budget of the absorbed laser pulse. The side with steeper gradient will prefer to dominate the energy extraction process.

During the laser nitriding process, incorporating nitrogen into the molten surface layer is described by a one dimensional nitrogen diffusion equation:

$$\frac{\partial C_N(x, t)}{\partial t} = D(T) \frac{\partial^2 C_N(x, t)}{\partial x^2} \quad (3.9)$$

where $C_N(t)$ is the nitrogen concentration, $D(T)$ is the temperature dependent nitrogen diffusion constant. If the diffusion constant D is assumed be a constant, the simplest solution of equation 3.9 is either a complementary error function:

$$C_N(x, t) = C_0 \operatorname{erfc} \left[\frac{x}{\sqrt{4Dt}} \right], \quad C_N(0, t) = C_0, t > 0 \quad (3.10)$$

according to the boundary condition of constant nitrogen concentration C_0 at the surface [104], or a Gaussian function:

$$C_N(x, t) = \frac{M}{\sqrt{\pi Dt}} \exp \left[\frac{-x^2}{4Dt} \right], \quad M = \int_0^\infty C_N(x, t) dx = \text{const.} \quad (3.11)$$

which maintains a constant total nitrogen amount M in the nitrogen diffusion process [104].

3.2 Experimental findings

In order to evaluate the nitrogen pressure dependence of pulsed laser nitriding, a series of experiments were conducted, from single pulse irradiation, isotopic multipulse irradiation, to meandering surface treatment. The simplest single pulse experiments reveal directly the ambient pressure dependence of laser nitriding, from which some of the fundamental parameters characterizing the laser nitriding efficiency can be extracted. Multipulse isotopic experiments are an excellent technique to trace the evolution of the nitrogen content during subsequent laser irradiation. Furthermore, through multipulse irradiation, the saturation of nitrogen take up is reached. Some samples are nitrided by a meandering treatment which provides the possibility of large surface nitriding with good surface morphology.

In the following sections, the nitrogen concentration depth profile, surface morphology, and the surface phase composition at different ambient nitrogen pressures are presented. The samples under investigation are iron and stainless steels, which have been irradiated by XeCl excimer laser pulses (55 ns FWHM) with an energy density of 4 J/cm^2 and a repetition rate below 10 Hz.

3.2.1 Nitrogen concentration depth profile

At first, single pulse excimer laser nitriding of iron at different nitrogen pressures was investigated. The incident laser beam was homogenized after the microlens array, which minimized the hydrodynamics convection induced by the temperature inhomogeneity in the molten surface layer [1, 35]. Before each laser pulse in a nitrogen environment, the sample surface was pre-irradiated in inert gas such as argon to remove surface oxide layer. In order to increase the statistics in the subsequent RNRA analysis, the nitriding treatment was done in enriched ^{15}N gas from 0.05 bar to 2 bar. Due to the limited ^{15}N resource, the single pulse nitriding experiments above 2 bar were conducted in natural nitrogen environment until 10 bar.

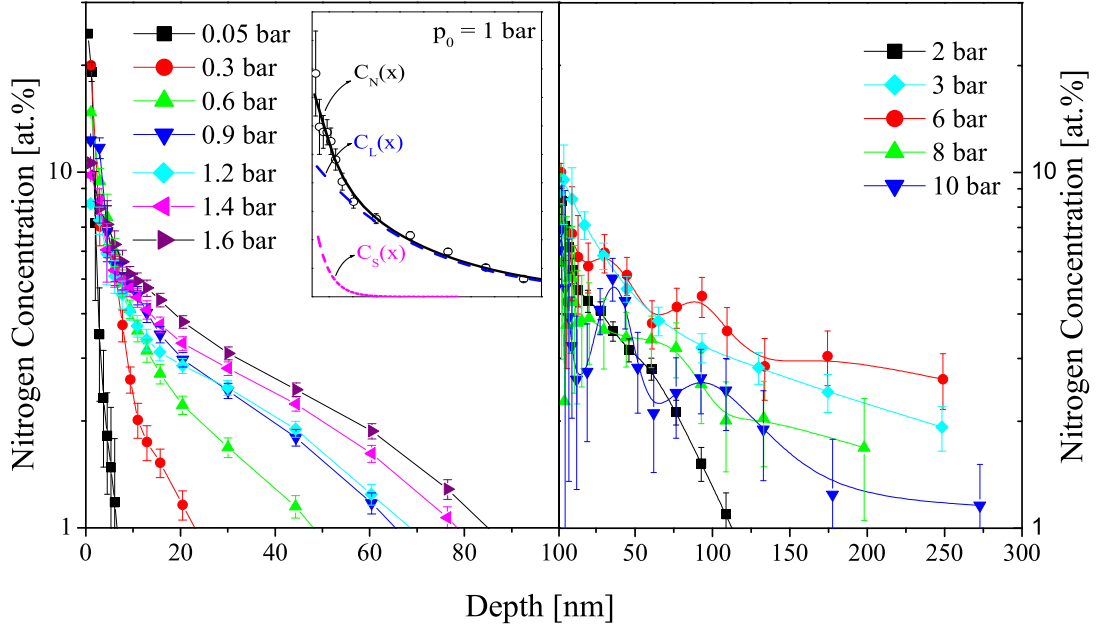


Figure 3-2: Nitrogen depth profiles of excimer laser nitrided iron after single pulse irradiation, the nitrogen pressures range from 0.05 bar to 10 bar. The insert shows the fitting of the nitrogen depth profile with the superposition of two exponential functions ($p_0 = 1$ bar).

The efficiency of the laser nitriding of iron is mainly reflected by the nitrogen depth profiles deduced from RNRA. These profiles in single pulse laser irradiated iron at the nitrogen pressures from 0.05 bar to 10 bar, are shown in Figure 3-2. The left part of Figure 3-2 presents the data in the low pressure region below 2 bar. The common feature shared by the nitrogen profiles in this regime is that they are similar to exponential functions with a maximum nitrogen content exceeding 10 at.% at the surface. The most distinct difference is the increase of the nitrogen distribution depth, from less than 10 nm at 0.05 bar, to more than 85 nm at 1.6 bar.

The right part of Figure 3-2 shows the nitrogen depth profiles in the high pressure region from 2 bar to 10 bar. The nitrogen distribution continually increases up to 6 bar, but then drops. When the nitrogen pressure exceeds 3 bar, the profiles become

more complicated, there is a new local maximum around 100 nm. Another fact worth mentioning is the saturation of the nitriding efficiency with nitrogen pressure. Pressure of 3 bar already reaches the optimal nitriding result, higher pressures such as 8 bar or 10 bar neither improve the nitrogen concentration, nor the nitriding depth. In fact, the nitrogen pressure of 10 bar leads to lower nitriding efficiency than 3 bar.

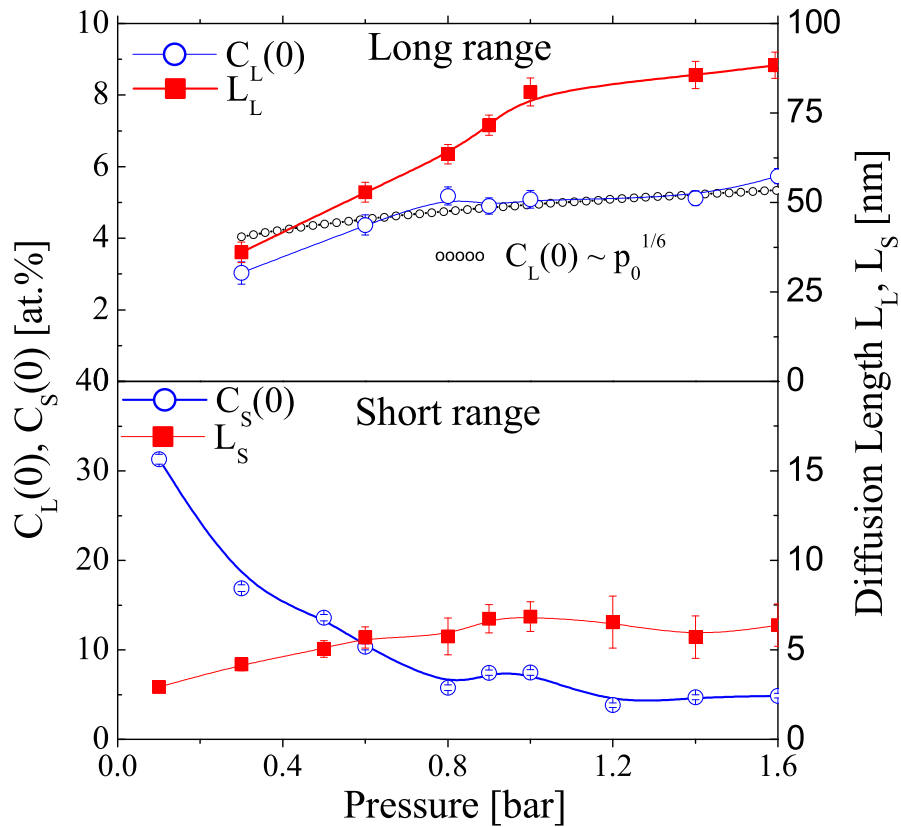


Figure 3-3: Characteristic parameters of the nitrogen depth profiles after single pulse laser irradiation as the functions of the nitrogen pressure.

Before the further analysis, the first question is how to retrieve valuable parameters from the nitrogen depth profiles. They should be able to characterize the nitriding efficiency and reflect the fundamental mechanism of laser nitriding. The first simplification is to assume that the nitrogen is incorporated into the molten iron by a one

dimensional diffusion process. Secondly, a infinite reservoir of nitrogen is supposed to be at the vapor/liquid interface during the laser nitriding process. Furthermore, the diffusion constant D is simplified to be independent of the temperature. Under these conditions, the solution of the one dimensional diffusion equation is an error function: $Cerfc\left[x/\sqrt{4Dt}\right]$, which can be well approximated by an exponential function: $Cexp(-\sqrt{\pi}x/L)$, the deviation between the two functions being below 8 % if $L = \sqrt{4Dt}$ [88, 89, 35, 37].

In the low nitrogen pressure region below 2 bar, the nitrogen concentration depth profiles $C_N(x)$ are fitted with the superposition of two exponential decay functions (as indicated in the insert of Figure 3-2):

$$C_N(x) = C_L(x) + C_S(x) = C_L(0)exp^{-\frac{\sqrt{\pi}x}{L_L}} + C_S(0)exp^{-\frac{\sqrt{\pi}x}{L_S}} \quad (3.12)$$

The main difference between the two exponential functions comes from the diffusion depth: The long range component $C_L(x)$ with a diffusion length of $L_L \approx 80$ nm ($p_0 = 1$ bar) corresponds to the nitrogen diffusion profile maintained by the laser plasma. The other exponential function $C_S(x)$ with a very short diffusion length of $L_S < 10$ nm cannot be ascribed to a real nitrogen diffusion process, but most likely corresponds to the fall out of laser plasma. Since nitrogen diffusion is the more fundamental process determining laser nitriding efficiency, more attention is focused on $C_L(x)$ rather than $C_S(x)$. It is supposed that the coefficient $C_L(0)$ is proportional to the solubility of nitrogen in molten iron and $C_S(0)$ reflects the amount of plasma fall out. The nitrogen pressure dependences of $C_L(0)$, $C_S(0)$, L_L and L_S in the low pressure region from 0.1 bar to 1.6 bar, are demonstrated in Figure 3-3.

At 0.1 bar, only the short range exponential function $C_S(x)$ contributes to the nitrogen concentration profile. From 0.6 bar to 1.6 bar, the long range component $C_L(x)$ becomes predominant. As shown in the upper part of Figure 3-3, both of $C_L(0)$ and L_L increase with ambient nitrogen pressure p_0 . Qualitatively, the pressure dependence of $C_L(0)$ is fitted as $C_L(0) \propto p_0^{1/6}$ at the pressure below 1.6 bar. Similarly,

L_L increases rapidly from 35 nm to 81 nm ($p_0 < 1\text{bar}$), then slowly to 88 nm ($p_0 = 1.6\text{ bar}$). As for the short range component of nitrogen depth profile, the lower part of Figure 3-3 indicates that L_S is always less than 7 nm, corresponding to the typical thickness of laser plume fall out. $C_S(0)$ drops drastically from 0.1 bar to 1 bar, due to the reduced laser ablation with increasing nitrogen pressures. From the comparison between nitrogen pressure dependence of $C_L(x)$ and $C_S(x)$, a transition from laser ablation dominated regime to nitrogen diffusion dominated regime is clearly demonstrated.

When the nitrogen pressure exceeds 2 bar, the nitrogen depth profiles can not be fitted with the combination of two exponential functions. The mean nitrogen concentration at 10 bar is even lower than that at 3 bar. This may be ascribed to the plasma break down in the high density plasma front, where most of incident photons are absorbed and the hot plasma region is decoupled from the iron surface. Therefore, nitrogen pressures more than 3 bar do not improve the energy coupling in the laser-plasma-metal system. The optimal iron nitriding pressure window lies between 2 bar and 3 bar.

In order to achieve large nitriding depth, multipulse laser irradiation was utilized. Although subsequent laser pulses increase the nitrogen take up and nitriding depth, they also induce nitrogen depletion. Since the chemical potential of nitrogen molecule is lower than the iron nitride compound, nitrogen atoms in nitrified iron prefer to recombine as nitrogen molecules and escape from the surface [136], known as the degassing effect. The degassing rate increases exponentially with surface temperature. Furthermore, due to the high laser intensity, the surface temperature of iron under laser irradiation is much higher than the evaporation temperature, a thin surface layer with maximum nitrogen concentration would be evaporated or ablated.

In order to trace the evolution of the nitrogen content during subsequent laser pulses, a delicate multipulse isotopic experiment was designed to distinguish the competing processes between nitrogen take up and depletion. Since RNRA only detects

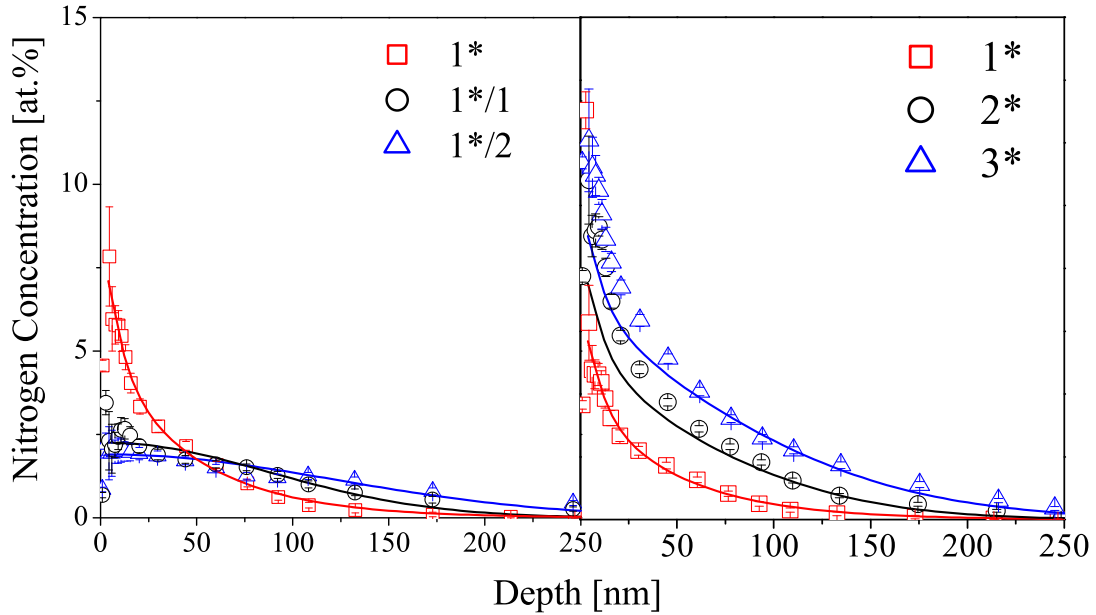


Figure 3-4: Nitrogen depth profile evolution in the ^{15}N isotopic multipulse experiments ($p_0 = 1$ bar).

the resonance signal of ^{15}N , the isotopic experiments were conducted in two directions: (1) Always in ^{15}N enriched environment (16.89 % ^{15}N), iron samples were irradiated with an increasing number of laser pulses. (2) The iron sample were first irradiated in ^{15}N enriched environment, followed by the laser irradiation in natural nitrogen gas (0.37 % ^{15}N). After the analysis of the corresponding nitrogen depth profiles, (1) demonstrated the net nitrogen take up and (2) revealed the evolution of the nitrogen content and how much nitrogen was released after the subsequent pulse irradiation.

Figure 3-4 shows two typical isotopic experimental results, at the nitrogen pressure of 1 bar. After the first shot in ^{15}N (denoted as 1*), the nitrogen depth profile is fitted according to equation 3.12. The diffusion length of the long range component $L_L = \sqrt{4Dt_1}$ is 81 nm (where the diffusion constant D is determined by $D = D_0 \exp(-Q/RT)$, with $D_0 = 2.86 \times 10^{-3} \text{ cm}^2/\text{s}$ and $Q = 61090 \text{ J/mol}$ for

liquid iron [91]). Under the irradiation of 4 J/cm^2 excimer laser pulse, a mean temperature of 2445 K and a melting time of $t_m = 293 \text{ ns}$ are estimated based on the one dimensional thermal simulation by Illgner and Schaaf [84], a constant diffusion constant D of $1.42 \times 10^{-4} \text{ cm}^2/\text{s}$ is assumed during the laser nitriding. If both D and L_L are know, the nitrogen diffusion time t_1 for the single pulse irradiation (1^*), or from another aspect, the plasma-metal effective coupling time t_c , is derived to be 112 ns.

After the first shot in ^{15}N enriched N_2 comes the second pulse in natural nitrogen (denoted as $1^*/1$). The nitrogen depth profile looks very different from the exponential function. The surface nitrogen concentration is merely about 2 at.% while the nitrogen depth exceeds 250 nm. Nevertheless the nitrogen profile of $1^*/1$ could be fitted quite well by a Gaussian function: $M/\sqrt{\pi Dt} \exp[-x^2/4Dt_2]$, as shown in the right part of Figure 3-4. The physical meaning of the Gaussian function is same as the complementary error function, also a solution of the diffusion equation 3.9 with the boundary condition of constant nitrogen content M . From the Gaussian fitting, a nitrogen diffusion time $t_2 = 239 \text{ ns}$ is derived for $1^*/1$. When a third pulse in natural nitrogen adds on (denoted as $1^*/2$), another Gaussian function with the diffusion time $t_3 = 480 \text{ ns}$ still fits the nitrogen profile. If the surface ablation and nitrogen degassing are neglected, the difference between t_2 and t_3 is equal to the melting time of surface iron t_m [89]. Thus from the Gaussian fitting of $1^*/1$ and $1^*/2$, t_m is determined to be around 241 ns (also comparable to the simulated melting time of 293 ns), about 129 ns longer than t_c . This suggests that the nitriding process does not start simultaneously as the surface melting, but after a certain time delay of $t_m - t_c$, the nitrogen gas has the chance to contact the surface molten layer.

In principal, if the nitrogen depth profile evolutions during the initial several pulses are well characterized, the nitrogen depth profile generated after an arbitrary number of pulses can be predicted. For example, two pulse irradiation in ^{15}N enriched environment 2^* is equivalent to the superposition of 1^* and $1^*/1$. Three pulse

irradiation in ^{15}N enriched environment 3^* is equivalent to $1^* + 1^*/1 + 1^*/2$. The predicted nitrogen depth profiles are plotted at the right side of Figure 3-4. There are some mismatches particularly in the surface layer within 100 nm, perhaps due to the improved surface absorption of the incident laser. The rough surface or the fall out produced by previous laser irradiation would produce more absorption centers for the incident laser light.

In summary, with isotopic nitriding experiments, some fundamental parameters characterizing the nitriding process are extracted. If a one dimensional thermal diffusion model with simplified boundary conditions is supposed, the physical correspondences of these parameters, such as the effective laser-metal coupling time t_c and the surface melting time t_m can be derived.

Technological applications usually need multipulse irradiation to achieve a deeper nitriding depth and higher nitrogen content. The nitrogen depth profiles in iron and stainless steel after 64 excimer laser pulse irradiation are illustrated in Figure 3-5. Compared to single pulse laser irradiation, the nitrogen profiles are smoother, especially in the high pressure region. This is probably due to the annealing effect introduced by the subsequent pulses. The overall nitrogen take up and nitriding depth increase rapidly in the low pressure region below 2 bar. When the nitrogen pressure exceeds 3 bar, there are no considerable improvements of the nitriding efficiency, demonstrating the similar pressure dependence as the single pulse experiments. Since nitrogen has a higher diffusion coefficient in b.c.c. iron than in f.c.c. iron austenite, laser nitriding of iron sample (Fe) maintains much higher nitrogen content compared to stainless steel (SS) under the same nitriding conditions.

3.2.2 Phase analysis

The previous sections focus on the nitrogen depth profile at different nitrogen pressures, however, after the ultra fast cooling and heating process, the phase compositions of laser nitrided iron and stainless steel are more important for real applications.

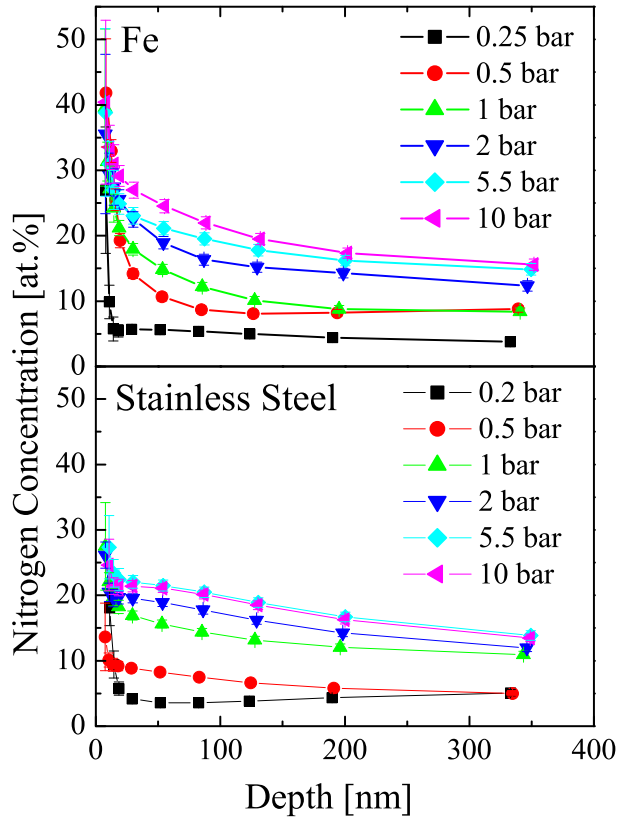


Figure 3-5: Nitrogen depth profiles of laser nitrided iron and stainless steel at different nitrogen pressures from 0.2 bar to 10 bar.

In this section, the near surface phases are analyzed by a combination of GIXRD and CEMS.

Stainless steel is an alloy composed of Cr, Ni and Mo, since CEMS is not sensitive to other metal nitride phases, such as CrN_x , NiN_x . GIXRD at a fixed incidence angle of 5° is utilized to detect all of the possible crystalline metal nitride phases.

The GIXRD spectra of laser nitrided stainless steel in Figure 3-6a reveal that in addition to the original austenite phase γ - $\text{Fe}(\text{CrNiMo})$ of stainless steel, the only new diffraction peaks correspond to γ - $\text{Fe}(\text{N})$. The amounts of other metal nitride phases are too small to be detected.

The diffraction spectrum of laser nitrided stainless steel is decomposed into two

subspectra [31], as illustrated in Figure 3-6b. The predominant contribution comes from the iron nitride austenite with larger lattice constant, the other one corresponds to the virgin stainless steel. For example, the $\langle 220 \rangle$ diffraction peak is fitted with the superposition of two Gaussian functions, corresponding to γ -Fe(N) and γ -Fe(CrNiMo), respectively. Their phase ratios are approximated by the area ratios of the Gaussian functions. In laser nitrided stainless steel, γ -Fe(N) has a similar fcc structure as virgin stainless steel except for the different lattice constant, which is stretched by the interstitial nitrogen atoms. The relationship between the nitrogen concentration C_N and the lattice constant a is described by [82]:

$$a = 3.595\text{\AA} + 0.78\text{\AA} \cdot C_N \quad (3.13)$$

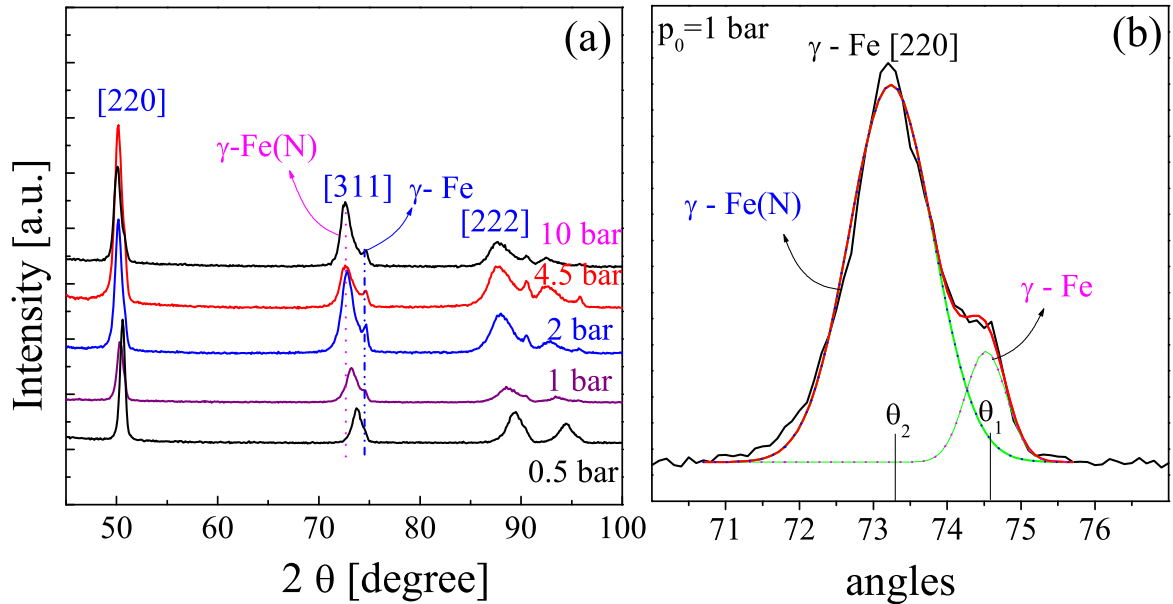


Figure 3-6: (a) GIXRD spectra of laser nitrided stainless steel at different nitrogen pressures. (b) Diffraction spectrum as the superposition of two subspectra with different lattice constants.

The Bragg diffraction rule for a fcc lattice is:

$$\sin\theta = \frac{\lambda}{2a} \sqrt{n^2 + l^2 + k^2} \quad (3.14)$$

where n , l , k are the Miller indices and λ the wavelength of the Cu K_α radiation utilized in our GIXRD measurement. The lattice constant of laser produced iron nitrides is derived from the positions of the diffraction peaks and the nitrogen concentration was determined from equation 3.13.

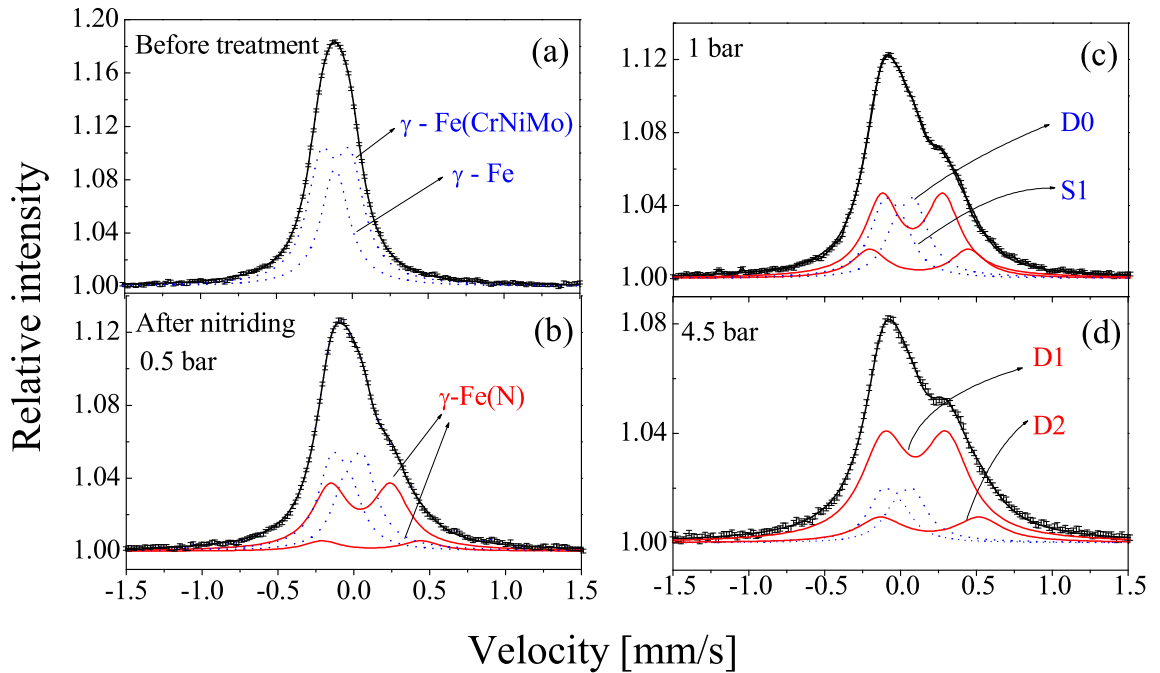


Figure 3-7: CEMS spectra of (a) virgin stainless steel, (b) stainless steel nitrided at 0.5 bar, (c) at 1 bar and (d) at 4.5 bar.

The CEMS spectra of stainless steel nitrided by the excimer laser ($H = 4\text{J}/\text{cm}^2$) are presented in Figure 3-7. The whole sample surface is irradiated with 8×8 meandering

scan. The CEMS spectrum of virgin stainless steel is shown in Figure 3-7a. As there is no local magnetic hyperfine field at the ^{57}Fe probe site, one expects a γ - Fe single line (S1). However, it is impossible to fit the CEMS spectra of stainless steel simply with S1, an additional γ - Fe(CrNiMo) doublet (D0) with small quadrupole splitting (QS) of 0.19(3) mm/s with the same isomer shift as S1 is adopted [32, 33]. D0 is ascribed to substitutional atoms such as Cr, Ni or Mo occupying the Fe site, which violate the electric field symmetry [100]. A more detailed discussion of the Mössbauer analysis of iron nitride can be found in some recent publications [96, 97, 98, 99]. After the laser nitriding, the stainless steel spectrum in Figure 3-7 is fitted by the superposition of one single line and three doublets. S1 and D0 with smallest QS (dotted line) correspond to virgin stainless steel. The two additional doublets (D1 and D2, plotted with solid line) are ascribed to the laser produced γ - Fe(N). The hyperfine parameters agree well with the previous study of Schaaf [25, 83], where the hyperfine parameters are calculated with a point charge model. The QS of D1 and D2 are 0.40(1) mm/s and 0.65(1) mm/s, respectively, corresponding to two different atomic configurations: with one (D1) or two (D2) nearest neighboring nitrogen atoms near the ^{57}Fe atom site.

As the nitrogen pressure increases, the area fractions of D1 and D2 increase systematically, while the contribution from virgin stainless steel is reduced. It seems that the area fraction of iron nitride austenite is correlated to the abundance of interstitial nitrogen atoms. For each ^{57}Fe probe atom, there are six possible nearest neighboring sites for the interstitial nitrogen atoms. If the nitrogen atoms are assumed to be randomly distributed in the FeN_χ austenite, the occupation probability of the nitrogen atoms around ^{57}Fe is determined by a binominal distribution [25]:

$$P_6^n = \binom{6}{n} \chi^n (1 - \chi)^{6-n} \quad (3.15)$$

where n is the number of nearest neighboring nitrogen atoms around ^{57}Fe atom.

P_6^n is the corresponding occupation probability.

Since both virgin stainless steel and laser produced iron austenite contribute to S1 and D0, CEMS can not distinguish them. However, due to the different lattice constant, GIXRD is able to determine their phase ratios from the area fractions of the corresponding subspectra. From the area fraction of D1, after subtracting the contribution of virgin stainless steel to S1 and D0, we get P_6^1 , and then according to equation 3.15, the nitrogen concentration.

The comparison between the mean nitrogen concentration deduced from RNRA and CEMS at different nitrogen pressures is plotted in Figure 3-8. The nitrogen concentration derived from CEMS nicely agrees to the RNRA measurements (mean nitrogen concentration in the CEMS sensing depth of 150 nm) and is also correlated to the GIXRD results except for the high pressure region. Since the affinity to nitrogen is much higher for Cr than for Fe, the high nitriding pressure maybe leads to the formation of chromium nitrides (CrN , Cr_2N), which are invisible in ^{57}Fe CEMS. For GIXRD, it should be mentioned that the sampling range of GIXRD with 5° incidence angle is about 750 nm, much deeper than RNRA sampling depth, so the mean nitrogen concentration derived from GIXRD is less than the results from the RNRA or CEMS measurement.

Similar to stainless steel, phase analysis of laser nitrided iron is conducted by CEMS and GIXRD. GIXRD spectra of laser nitrided iron at 5° incidence angle are plotted in Figure 3-9. The samples were irradiated by 8*8 meandering treatment, with a energy density of $4\text{J}/\text{cm}^2$. Virgin iron is in the pure α - Fe phase. After the laser treatment, the predominant iron nitride phases is γ - Fe(N) with the mean nitrogen concentration around 10 at.%. As the nitrogen pressure increases, the diffraction peaks from γ - Fe(N) phase become more prominent. When the pressure exceeds 2 bar, there is new diffraction signal from ϵ - Fe_{2+x}N corresponding to a nitrogen concentration of more than 10 at.%. The linewidths of the diffraction peaks of ϵ - Fe_{2+x}N and γ - Fe(N) phase are much broader than those of the α - Fe phase. It

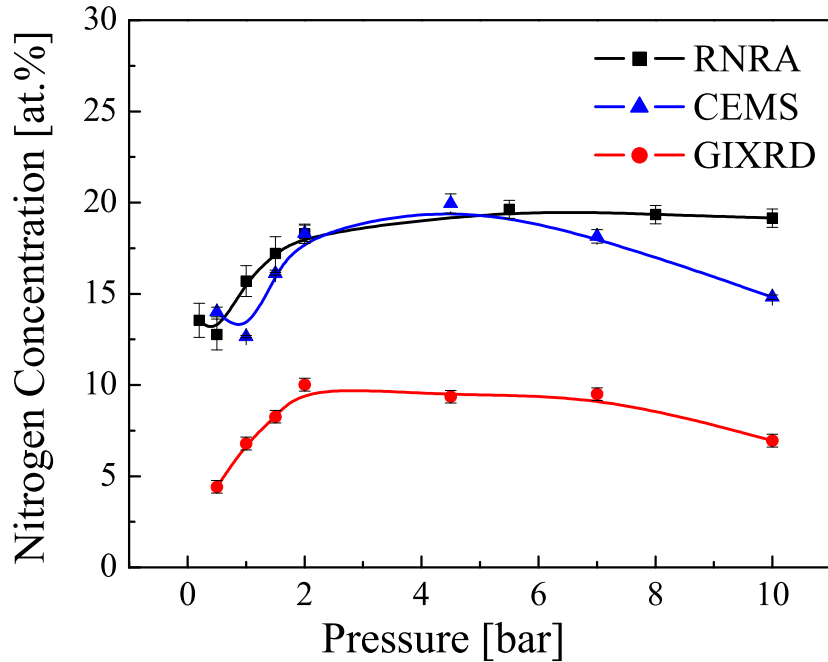


Figure 3-8: Comparison of the mean nitrogen concentrations in stainless steel deduced from CEMS, GIXRD and RNRA measurements, respectively.

means that the main grain size of ϵ - Fe_{2+x}N or γ - $\text{Fe}(\text{N})$ is smaller than the virgin iron due to the fast cooling induced by the high power laser.

CEMS spectra of laser nitrided iron are presented in Figure 3-10a. The hyperfine parameters of the iron nitride phases are adopted from the work of Schaaf and Kopcewicz [25, 93, 94]. Phase ratios of the iron nitrides and virgin α - Fe are plotted in Figure 3-10b as the function of nitrogen pressure. At low nitrogen pressure, the predominant phase is γ - $\text{Fe}(\text{N})$. As the pressure exceeds 2 bar, a significant change emerges due to the formation of ϵ - Fe_{2+x}N , the main nitride phases consist of ϵ , α and α' . At high pressure, the phase ratio of ϵ - Fe_{2+x}N reaches nearly 40%, much higher than the GIXRD results. This significant difference suggests that ϵ - Fe_{2+x}N phase is mainly distributed in the surface within the CEMS sensing depth of 150 nm. Most important, as demonstrated in the phased ratio variations at different nitrogen

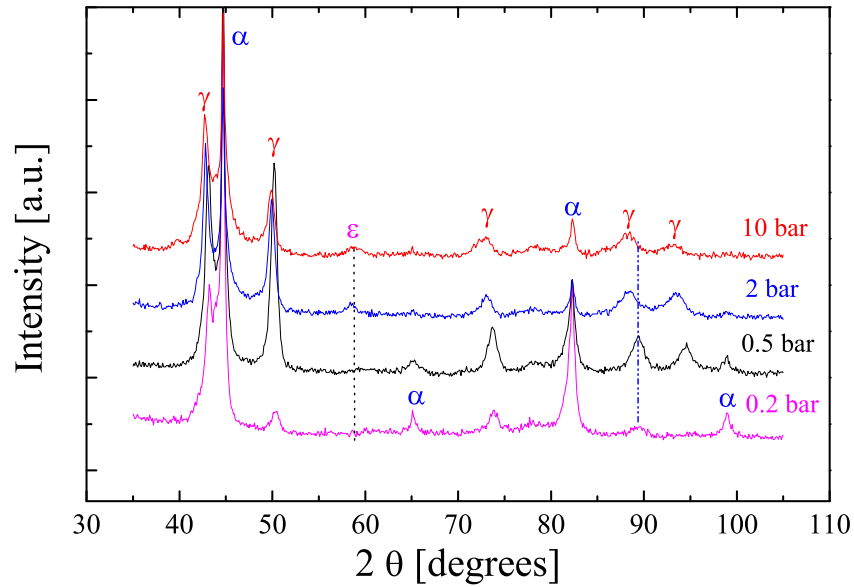


Figure 3-9: GIXRD spectra of laser nitrided iron at different nitrogen pressures.

pressures, the nitriding efficiency shows a rapid increment below 2 bar and a flat plateaus at high pressure region.

3.2.3 Surface morphology

After the laser treatment, there are remarkable change of the surface morphology, as shown in Figure 3-11. It is interesting to investigate the surface profile after the laser irradiation, since the surface material redistribution is determined mainly by the surface plasma pressure and the plasma-metal coupling time. It provides another possibility to probe the laser nitriding process.

Because the stainless steel samples are prepared with less surface roughness, the investigation of the surface morphology is focused on stainless steel. Surface profiles of stainless steel nitrided at different nitrogen pressure are illustrated in Figure 3-11. It is found that during laser nitriding, the molten surface materials are redistributed, some are evaporated or ablated, some are pushed to the laser border by the gradient

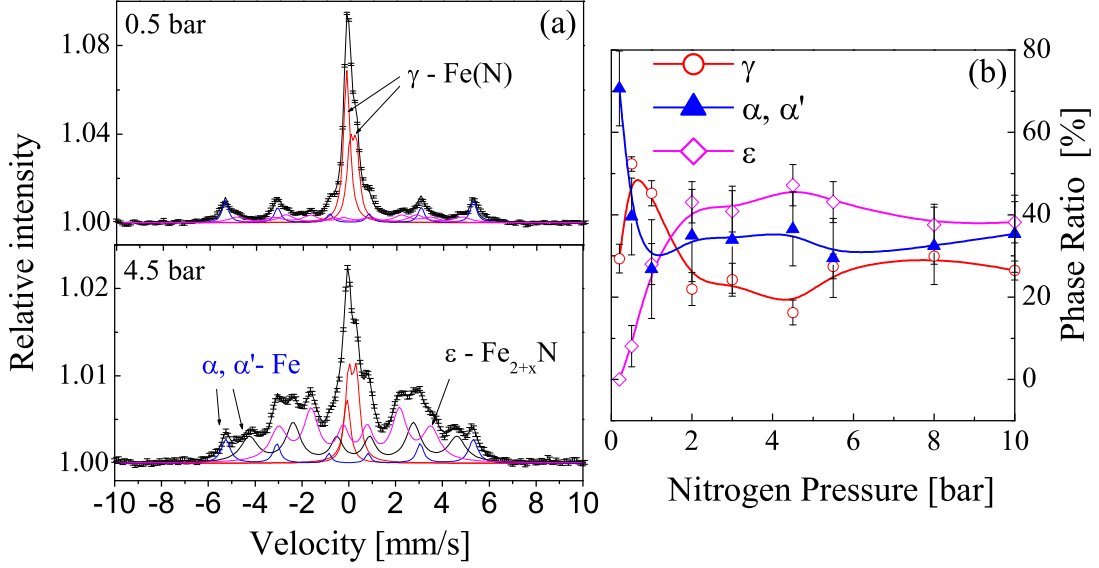


Figure 3-10: (a) CEMS spectra of laser nitrided iron at the nitrogen pressure of 4.5 bar and 0.5 bar, respectively. (b) Phase composition deduced from CEMS spectra.

of plasma pressure and recoil pressure of surface evaporation, thus a crater is formed, known as piston effect. A schematic drawing of the piston effect is illustrated in Figure 3-12. After integration of the depth of laser crater with the lateral length, two characteristic quantities V_+/V_- are extracted corresponding to the integral ranges outside/inside the laser spot border, as illustrated in Figure 3-11. Physically, V_+ is ascribed only to piston effect (also denoted as V_{pist}). The removed surface material inside the laser spot V_- is due to both surface evaporation and piston effect. Subtraction of V_+ from V_- leads to V_v , corresponding to the net amount of evaporated materials if the fall out from the laser plume is neglected.

The velocity of piston movement u_{pist} is determined by p_{plasma} and p_r :

$$u_{pist} = \sqrt{\frac{2(a+b)K_l \ln(T_b/T_m)}{a \cdot b}} \left(\frac{2(p_{plasma} + p_r)}{\rho_l} \right)^{\frac{1}{4}} \quad (3.16)$$

where T_b/T_m is the boiling/melting temperature of iron, ρ_l is the molten metal

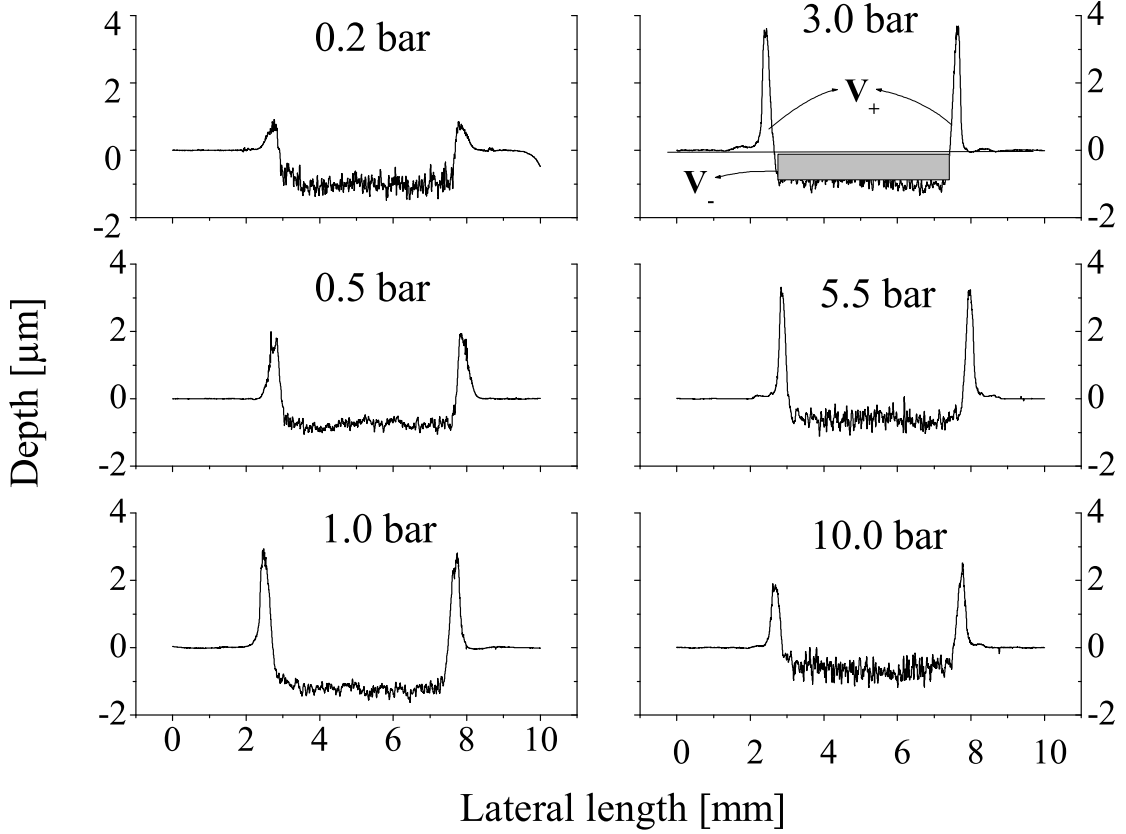


Figure 3-11: Surface profiles of stainless steel after excimer laser irradiation (64 pulses) at different nitrogen pressures.

density, K_l is the thermal conductivity of molten iron and a, b describe the dimensions of the laser pulse. With typical $H = 4 \text{ J/cm}^2$ excimer laser irradiation, p_{plasma} and p_r are estimated to be 480 bar and 290 bar, respectively [1].

The amount of removed molten material due to piston effect corresponds to the integration of piston movement velocity u_{pist} with the plasma-metal coupling time t_c

$$V_{pist} \propto \int_0^{t_c} u_{pist} dt \quad (3.17)$$

During the nitriding process, the evaporation rate of metal ($\partial x_{ev}/\partial t$) is determined

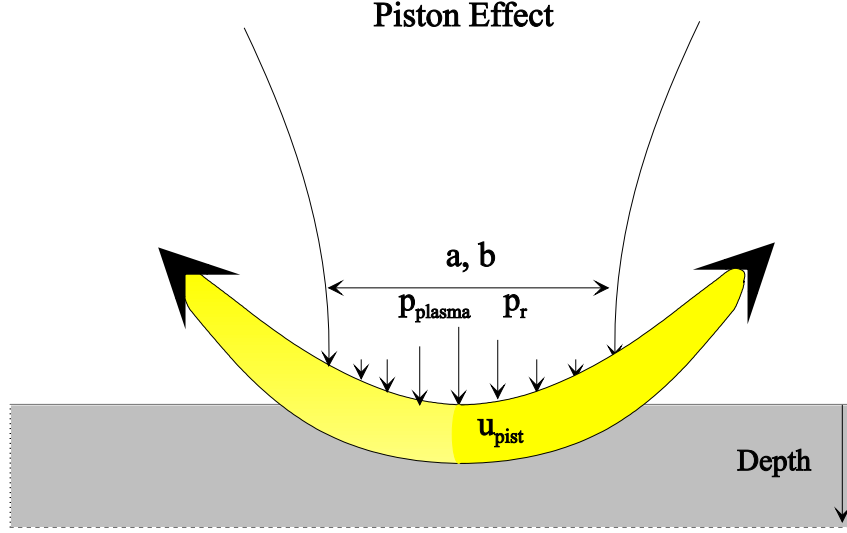


Figure 3-12: Schematic illustration of the piston effect induced by the plasma pressure p_{plasma} and the recoil pressure of surface evaporation p_r [102].

by the molten metal temperature T_l [102]:

$$\frac{\partial x_{ev}(t)}{\partial t} = \frac{p_v(T_l)}{\rho_l \sqrt{2\pi \frac{k_B}{m_a} T_l}} \quad (3.18)$$

where x_{ev} is the evaporation depth, p_v is the vapor pressure. m_a denotes the atomic mass. Similar to V_{pist} , V_v is proportional to the integration of the evaporation rate with time duration of evaporation (t_v):

$$V_v \propto \int_0^{t_v} \frac{\partial x_{ev}(t)}{\partial t} dt \quad (3.19)$$

The nitrogen gas pressure dependence of V_{pist} and V_v is illustrated in Figure 3-13. V_v reaches maximum at 0.2 bar, where V_v is 6 times larger than V_{pist} . In low pressure region below 2 bar, as pressure increases, the rapid drop of V_v is ascribed to the increased absorption of incident laser at the plasma front, which reduces the surface temperature of metal and evaporation rate. The pressure dependence of V_v is more complicated when the pressure is above 2 bar. Although the evaporation rate is reduced, part of the energy absorbed by the plasma would be returned to the metal

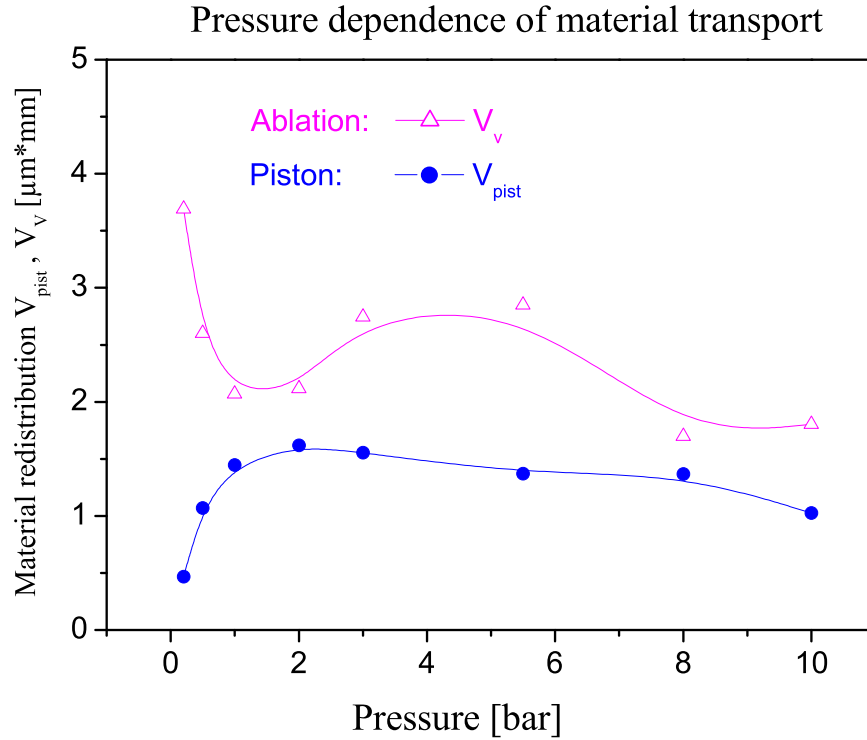


Figure 3-13: Material redistribution deduced from the surface profiles after laser treatment. The curves are plotted to guide the eye.

surface via re-emitted irradiation from the plasma, which could eventually increase the time duration of evaporation.

As shown in Figure 3-13, the pressure dependence of V_{pist} looks more straightforward: V_{pist} increases rapidly below 2 bar, remains nearly constant between 3 and 8 bar, and even drops a little around 10 bar. Clearly there is a strong correlation between V_{pist} and laser nitriding efficiency. Since surface profile measurement is much faster compared to RNRA or CEMS, it may be used for on-line monitoring of the nitriding efficiency.

In summary, from the comparison between V_{pist} and V_v , the investigation of surface profiles of stainless steel clearly indicates the reduced laser ablation with increasing

nitrogen pressure, which is related to the transition from low nitriding efficiency to high nitriding efficiency. It suggests that the energy distribution between evaporation (denoted as E_V) and melting (denoted as E_M) is critical for the optimal laser nitriding, if E_V is too high, as at low ambient pressures below 0.6 bar, more energy is dissipated by the surface ablation or evaporation. As nitrogen pressure increases, E_M is increased due to the absorption and re-emitted irradiation of the laser plume, which effectively enhances the laser-metal energy coupling and improves the laser nitriding efficiency.

3.3 Discussion of laser plume dynamics

With RNRA, CEMS and GIXRD, the nitrogen concentration profiles and the surface phase compositions were derived. In the following section, the laser nitriding mechanisms and the laser plasma dynamics in the laser-plasma-metal system will be discussed and compared with the experimental results. Due to the complexity of the laser nitriding process, most attentions are focused on a qualitative approach instead of an exact quantitative calculations.

During the high power pulsed laser irradiation, once the laser plume is ignited, since it absorbs the incident photons, the laser-metal system now becomes a laser-plume-metal three body system. The plume dynamics plays a central role in this system because it not only determines the energy transfer to the irradiated metals but also provides the source for the nitrogen take up. There are several models describing the dynamics of laser plumes, which are briefly discussed as follows.

In 1990, Singh and Narayan developed an ideal gas approximation [111] to simulate the laser plume propagation. The dynamics of a laser generated plasma is classified into two stages: (1) isothermal expansion during the laser pulse duration τ . (2) adiabatic expansion into the vacuum after the laser irradiation. In the first stage, the

pressure p at any position (x,y,z) in the plasma is determined by:

$$p(x, y, z, t) = \frac{N_T t k_B T_0}{\sqrt{2\pi^{\frac{3}{2}} \tau V(t)}} \times \exp \left[-\frac{x^2}{2X(t)^2} - \frac{y^2}{2Y(t)^2} - \frac{z^2}{2Z(t)^2} \right], \quad t < \tau \quad (3.20)$$

where T_0 is the isothermal temperature of the plasma and N_T is the total number of evaporated particles at the end of laser pulse ($t= \tau$). $X(t)$, $Y(t)$, $Z(t)$ describe the dimensions of the expanding plasma whose volume is defined by $V(t)=X(t)Y(t)Z(t)$. The ideal gas equation ($p=nk_B T_0$) is supposed to be satisfied.

After the laser irradiation, the relationship between the volume and the temperature of the plasma is described by the adiabatic expansion

$$TV(t)^{\gamma-1} = \text{const.} \quad (3.21)$$

where γ is the ratio of the specific heat capacities of the laser plume.

The pressure inside the plume is given by

$$p(x, y, z, t) = \frac{N_T k_B T_0}{\sqrt{2\pi^{\frac{3}{2}} V(t)}} \times \exp \left[-\frac{x^2}{2X(t)^2} - \frac{y^2}{2Y(t)^2} - \frac{z^2}{2Z(t)^2} \right], \quad t > \tau \quad (3.22)$$

Singh's model well describes the plasma dynamics of low pressure pulsed laser ablation or PLD, however, in high pressure ambient gas environment, this model becomes invalid since now the laser plasma is too far away from ideal gas approximation.

Based on the most general rules of mass, energy and momentum conservation in the laser-plasma-metal system, Arnold developed a fully analytical approach to describe the laser plume propagation [112] with shock wave (SW) developed at the laser plume/ambient gas interface. Although his model can be applied for both low and high ambient gas pressure, it describes only the plume expansion after the extinction of the laser pulse, without including the period of the laser irradiation.

Raizer and Pirri [105, 106, 107, 108, 109, 110] proposed a laser supported absorption wave to model the laser-plasma-metal interactions during the pulsed laser

irradiation. The laser absorption wave is classified into two regimes: Laser Supported Combustion (LSC) wave and Laser Supported Detonation (LSD) wave, depending on the incident laser intensity I_0 . To illustrate the difference between these regimes, three threshold laser intensities are defined, namely: I_V (evaporation threshold), I_C (LSC wave threshold) and I_D (LSD wave threshold). When $I_V < I_0 < I_C$, the incident laser induces surface evaporation and a laser plume, but the laser plasma is of low density and high transparency. If $I_C < I_0 < I_D$, the plume starts to be ionized and part of the laser energy is absorbed and converted into the internal energy of the plasma. Due to the presence of the target surface, the laser absorption wave propagates subsonically towards the direction of laser beam and is preceded by a shock wave. After partial absorption, the laser beam can still penetrate the plasma to reach the material surface. When $I_D < I_0$, essentially all of the incident laser energy is absorbed in the high density plasma front, strong heating of the plasma yields a supersonic expansion of the laser absorption wave, named LSD wave. It actually decouples the incident laser beam from the metal surface, which is unattractive for the efficient laser-metal thermal coupling.

For the XeCl excimer laser, $I_C \approx 10^7 \text{ W/cm}^2$, and $I_D \approx 10^8 \text{ W/cm}^2$ [116]. The laser intensity of our 4J/cm^2 XeCl excimer is high enough to produce the LSC wave, but still below the threshold of LSD wave. Therefore, in the following discussion, the LSC wave model is adopted to describe the dynamics of the laser plume during the laser irradiation.

The spatial geometry of the LSC wave during the excimer laser nitriding process is illustrated schematically in Figure 3-14, where the LSC wave is treated as a discontinuity and a homogeneous plasma is assumed. p , ρ and h describe the pressure, density and enthalpy of shocked nitrogen or plasma depending on the subscript *shock* or *plasma*. ρ_0 denotes the density of the ambient nitrogen gas, which is proportional to the nitrogen pressure p_0 . The propagation velocities of LSC and shock wave are denoted as V_W and u_{shock} , respectively.

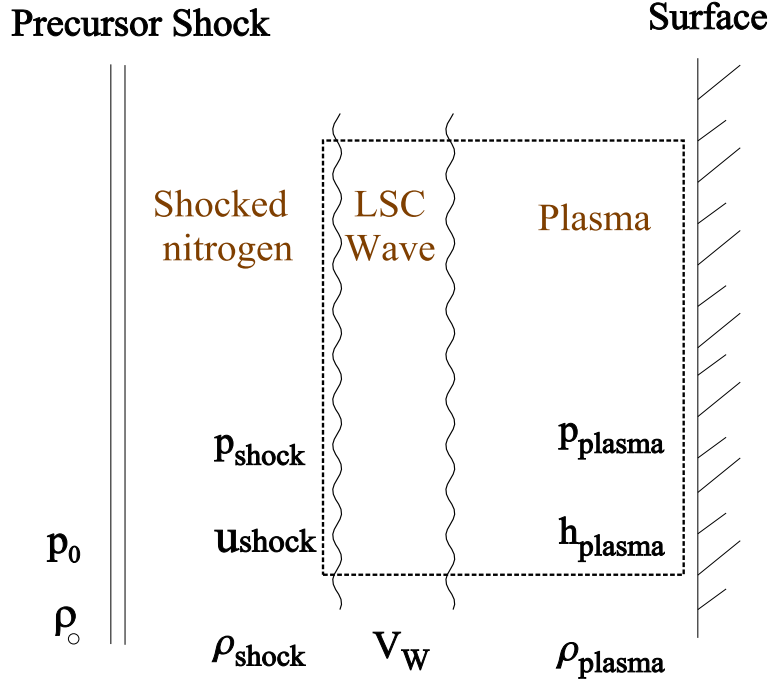


Figure 3-14: Schematic diagram of laser supported combustion wave.

In the coordinate system attached to the LSC wave, the conservation of energy in the volume between the LSC wave and metal surface requires:

$$\rho_{plasma} V_W \left(h_{plasma} + \frac{V_W^2}{2} \right) = \rho_{shock} (V_W - u_{shock}) \left(h_{shock} + \frac{(V_W - u_{shock})^2}{2} \right) + I_a \quad (3.23)$$

where I_a is the absorbed laser intensity by LSC wave.

Conservation of mass and momentum across the LSC wave leads to:

$$\rho_{plasma} V_W = \rho_{shock} (V_W - u_{shock}) \quad (3.24)$$

and

$$p_{plasma} + \rho_{plasma} V_W^2 = p_{shock} + \rho_{shock} (V_W - u_{shock})^2 \quad (3.25)$$

In the laser plasma the relationship among pressure, density and enthalpy is described by

$$p_{plasma} = \frac{\gamma - 1}{\gamma} \rho_{plasma} h_{plasma} \quad (3.26)$$

In the high ambient pressure nitrogen gas, across the shock wave, strong shock wave relations yield

$$p_{shock} = \frac{\gamma_s + 1}{2} \rho_\infty u_{shock}^2 \quad (3.27)$$

and

$$\rho_{shock} = \frac{\gamma_s + 1}{\gamma_s - 1} \rho_0 \quad (3.28)$$

where γ_s and γ are the adiabatic exponents for the shocked nitrogen and laser plasma respectively.

From the upper equations, the pressure of plasma p_{plasma} and velocity of the LSC wave V_W in terms of the absorbed laser intensity are derived:

$$p_{plasma} = \left[1 - \frac{2W}{\gamma_s - 1} \right] \left[\frac{\gamma_s + 1}{2} \right]^{\frac{1}{3}} \left[\frac{(\gamma - 1)(\gamma_s - 1)}{(\gamma + W)(\gamma_s - 1 - 2W)} \right]^{\frac{2}{3}} \rho_0^{\frac{1}{3}} I_a^{\frac{2}{3}} \quad (3.29)$$

and

$$V_W = (W + 1) \left[\frac{(\gamma - 1)(\gamma_s - 1)}{(\gamma_s + 1)(\gamma + W)(\gamma_s - 1 - 2W)} \cdot \frac{I_a}{\rho_0} \right]^{\frac{2}{3}} \quad (3.30)$$

where W is a nondimensionalized particle velocity that can be approximated by $W = 0.009 \cdot I_a^{2/3}$ for I_a in MW/cm².

After a brief introduction to the theoretical models of the laser plume dynamics, here the previous experimental findings will be interpreted qualitatively. The first focus is the plasma pressure p_{plasma} , since it strongly influences the solubility of nitrogen S_N in molten iron, which is the most important factor influencing the nitrogen

take up. Though the laser plasma consists of both diatomic nitrogen molecules and monoatomic neutral or ionized nitrogen, it is supposed that the relationship between p_{plasma} and S_N still follows the Sieverts law [91, 118]

$$S_N \propto \sqrt{p_{plasma}} \quad (3.31)$$

During the laser irradiation, the laser plume dynamics is described by the LSC wave model, simplification of equation 3.29 leads to $p_{plasma} \propto \rho_0^{\frac{1}{3}}$, when $t < \tau$.

After extinction of the pulsed laser irradiation, since the lateral dimension of the laser produced plasma is much bigger than the vertical dimension (the direction of the incident laser), a one dimensional approximation of the laser plume propagation is adopted. The conservation of the laser plume momentum leads to [112]

$$p_{plasma} - p_{shock} \propto \frac{d}{dt} \left(\rho_0 R \frac{dR}{dt} \right) \quad (3.32)$$

where R describes the vertical dimension of the laser plasma, the pressure of the shocked nitrogen gas at the shock wave front is given by [114, 113]

$$p_{shock} = \frac{\gamma_s + 1}{2} \rho_0 u_{shock}^2 \propto \rho_0 \left(\frac{dR}{dt} \right)^2 \quad (3.33)$$

thus equation 3.32 can be rewritten as

$$p_{plasma} \propto k \rho_0 \left(\frac{dR}{dt} \right)^2 + \rho_0 R \frac{d^2 R}{dt^2} \quad (3.34)$$

where k is a constant. According to a planar shock wave model [120, 121] the time dependent $R(t)$ is approximated by:

$$R(t) \propto \left(\frac{E_a}{\rho_0} \right)^{\frac{1}{3}} t^{\frac{2}{3}} \quad (3.35)$$

where E_a is the absorbed laser energy by the laser plasma.

from the upper equations, it can be deduced that

$$p_{plasma} \propto k\rho_0 \left(\frac{dR}{dt} \right)^2 + \rho_0 R \frac{d^2 R}{dt^2} \propto \rho_0^{1/3} t^{-2/3}, \quad t > \tau \quad (3.36)$$

It is nice to find that during and after the pulsed laser irradiation, the nitrogen pressure dependence of p_{plasma} shares the same law: $p_{plasma} \propto \rho_0^{1/3}$. Combined with equation 3.31, the nitrogen solubility S_N is estimated to be $S_N \propto \rho_0^{1/6} \propto p_0^{1/6}$. If we assume that the long range coefficient $C_L(0)$ in the nitrogen depth profiles is proportional to S_N , the nitrogen pressure dependence of $C_L(0)$ in Figure 3-3 is qualitatively well interpreted based on the LSC wave model.

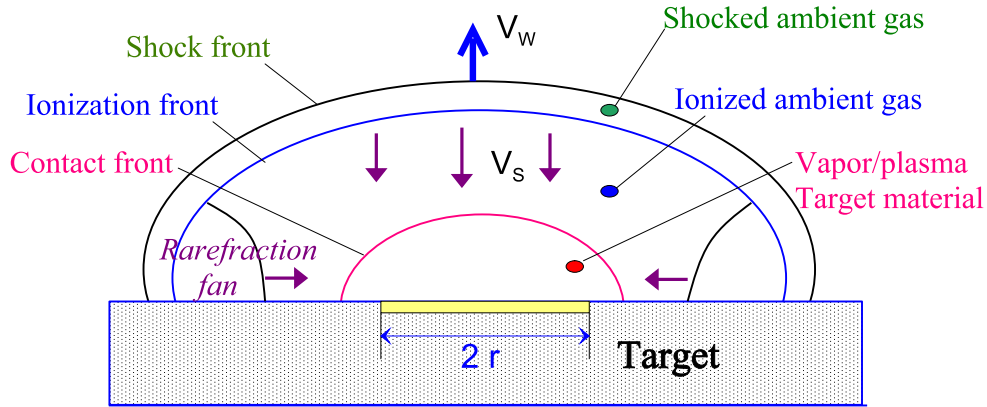


Figure 3-15: Schematic drawing of the spatial structure of laser plume.

From the previous analysis of nitrogen profile evolution in the isotopic multipulse experiments, a discrepancy between the plasma-metal coupling time t_c and the melting time of iron t_m is found. The next aim is to give a reasonable explanation based on the laser plume dynamics.

The spatial and temporal structures [115, 116] of the laser produced plume are schematically illustrated in Figure 3-15 and Figure 3-16, respectively.

As illustrated in Figure 3-15, at a laser intensity greater than the LSC wave threshold, a LSC wave in the metal vapor is ignited. Because of the presence of

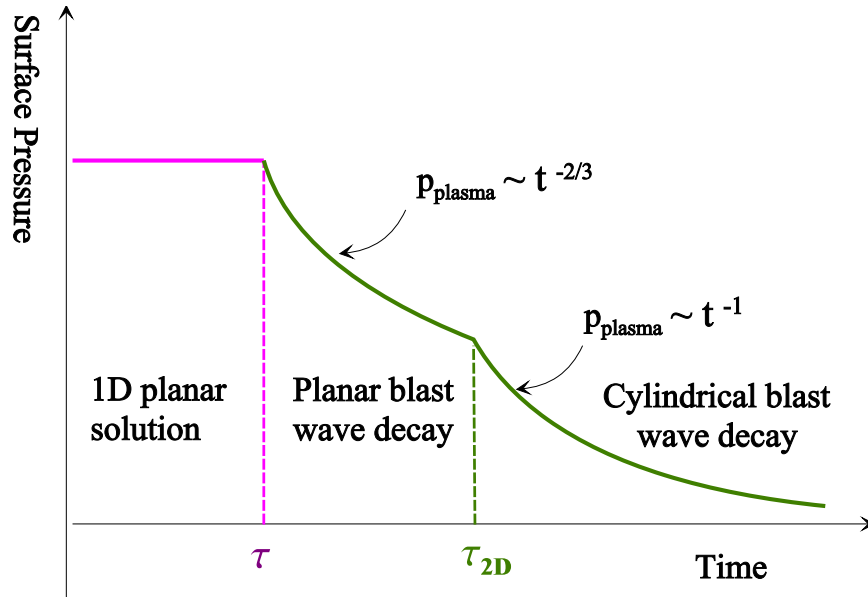


Figure 3-16: Schematic drawing of the plasma pressure as a function of time.

the target surface, a precursor shock wave precedes the LSC wave. The nitrogen atoms in front of the metal vapor are partially ionized due to the electron heating (inverse bremsstrahlung absorption) and the shock wave heating, a significant fraction of the incident photons are absorbed in the ionization front of the laser plume, which supports the propagation of the LSC wave into the nitrogen gas along the laser beam path. The pressure gradient behind the LSC wave induces a reversed gas flow or a rarefaction fan moves toward the target from the vertical and lateral direction (as indicated by the arrows in Figure 3-15). The gas flow is critical for the laser nitriding process, since before the rarefaction fan reaches the target surface, the ambient nitrogen atoms are actually screened from the metal surface due to the metal vapor expansion. Therefore, laser nitriding does not start simultaneously with the ignition of the laser plume, only after a certain time delay, when the rarefaction fan touches the metal surface, the ionized or neutral nitrogen atoms starts diffusing into the molten iron.

The time evolution of the laser plume is characterized by two relaxation times: τ_{2D} and τ_z . At the radial relaxation time τ_{2D} , the leading edge of the rarefaction fan

from the spot border reaches the laser spot center. τ_{2D} is given by

$$\tau_{2D} = r/V_S \quad (3.37)$$

where r is the laser spot radius and V_S is the sound speed in the laser plume, which is determined by:

$$V_S = \sqrt{\frac{p_{plasma}}{\rho_{plasma}}} = \left(\frac{\gamma p_{plasma}}{\rho_0} \right) \left[\frac{W+1}{W} \frac{\gamma_s - 1}{\gamma_s + 1} \right]^{\frac{1}{2}} \propto \rho_0^{-\frac{1}{3}} \quad (3.38)$$

Similarly, τ_Z is the time interval at which the rarefaction fan reaches the target surface in the vertical direction, it is determined by the sound speed V_S and the LSC wave propagation speed V_W in the laser plasma:

$$\tau_Z = \tau + \tau * \frac{V_W}{V_S} \quad (3.39)$$

where τ is the pulse duration of the laser. Combining equation 3.30 with equation 3.38, the ambient nitrogen pressure dependence of τ_{2D} is derived to be: $\tau_{2D} \propto \rho_0^{\frac{1}{3}}$. τ_Z is independent of ρ_0 .

Under the typical laser nitriding conditions ($4\text{J}/\text{cm}^2$, $p_0 = 1$ bar, $\gamma = 1.2$ and $\gamma_s = 1.4$), τ_{2D} and τ_Z are estimated to be 265 ns and 113 ns [1], respectively. The difference between t_c and t_m deduced from the previous fitting of the nitrogen profile is 129 ns, quite close to τ_Z . Furthermore, the sum of t_c (112 ns) and τ_Z (113 ns) is still less than τ_{2D} (265 ns), which means that the nitriding process is limited before the two dimensional effect dominates. So it is reasonable to model the laser plume dynamics with the one dimensional planar wave approximation. As illustrated in Figure 3-16, it is believed that the nitriding process is limited to the first two stages of laser plume propagation.

3.4 Summary

Based on the investigation of the nitrogen pressure series, the following conclusions can be drawn at this stage:

1: From the analysis of the nitrogen depth profiles and surface phase composition of excimer laser nitrided iron and stainless steel, the influence of the nitrogen pressure on nitriding efficiency was classified into two regimes: In the low pressure region below 2 bar, total nitrogen take up and nitrogen distribution depth increases rapidly. In the high pressure regime between 3 bar and 10 bar, the nitriding efficiency remains nearly constant and even drops around 10 bar. The optimal nitriding window is between 2 bar and 3 bar. The nitrogen and the surface profile variations at different nitrogen pressures clearly demonstrated the transition from laser ablation to nitrogen diffusion dominated regime. It is believed that the energy distribution between evaporation and surface melting is crucial to achieve a good nitriding efficiency.

2: The nitrogen depth profile $C_N(x)$ after single pulse irradiation was fitted with the superposition of two exponential functions $C_L(x)$, $C_S(x)$, corresponding to the contributions from the nitrogen diffusion and the plasma fall out. Their coefficients $C_L(0)$, $C_S(0)$ and the diffusion length L_L , L_S were extracted from the fitting. Physically, these characteristic parameters reflect the solubility of nitrogen in liquid iron and the plasma-metal effective coupling time t_c . With the aid of ^{15}N isotopic multi-pulse experiments, the evolution of the nitrogen content during the subsequent laser pulses was successfully traced. By exponential or Gaussian function fitting of the corresponding nitrogen profile, t_c and the melting time of the surface iron t_m were deduced.

3: Based on the LSC model and the conservation of momentum, a qualitative approach to the laser plume dynamics was conducted. The relationship between the ambient nitrogen pressure and the plasma pressure was estimated, which agreed quite well with the experimental findings in the low nitrogen pressure region below 2 bar. Furthermore, the discrepancy between iron melting time and plasma metal effective

coupling time was explained by the spatial and temporal structure of the laser plume. It has been found that only after a certain time delay of about 129 ns, when the plasma rarefaction fan contacted the iron surface, started the nitriding process.

Chapter 4

Influence of laser pulse duration on laser nitriding

4.1 Physics on different time scales

There are three most important processes involved in the early stage of laser nitriding of metals: absorption of the incident laser, production of the plasma and melting of the metal. These processes do not happen at the same time, but in a time sequence [126, 127, 128, 129]. Laser irradiation and the free carrier absorption start nearly simultaneously, on a time scale of 10^{-14} second, the energy equilibrium among excited free electrons is reached via electron-electron collisions. Then, through electron-phonon interaction, the excited free electrons dissipate their thermal energy to the lattice on a time scale of 10^{-12} second. This energy dissipation process is schematically illustrated in Figure 4-1. After a time interval of hundreds of picoseconds, the thermal energy transferred from the excited electrons to the lattice leads to surface melting and evaporation and the formation of a laser plume. When the laser pulse duration decreases from ns to ps, or fs, a remarkable change of the time sequence of laser-metal-plasma interactions will be expected, which forms the main motivation to investigate the influence of laser pulse duration on laser nitriding.

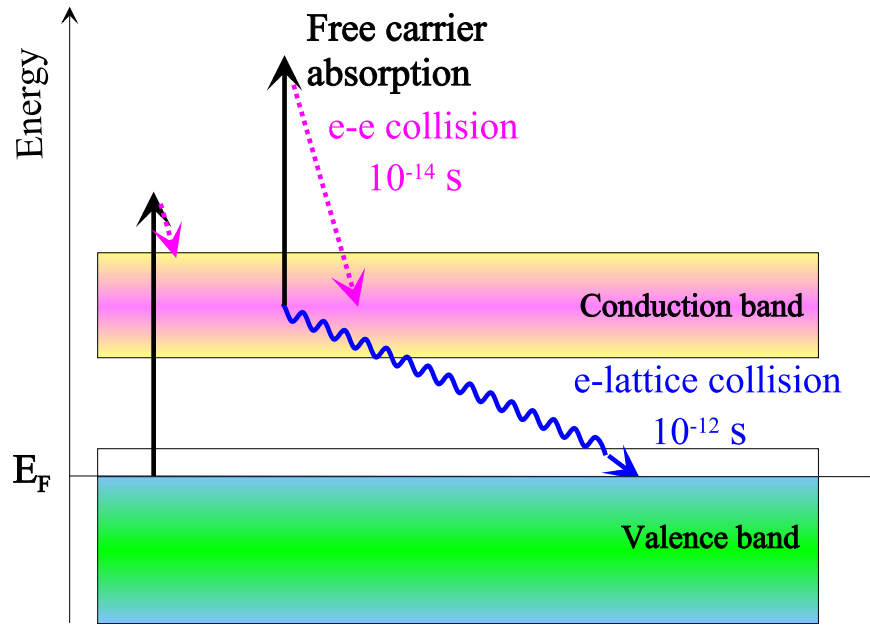


Figure 4-1: Schematic drawing of the photon energy dissipation mechanisms on different time scales [102].

The laser-plasma-metal interactions are schematically illustrated in Figure 4-2. For XeCl excimer laser, its 55 ns pulse duration is relatively long compared to the time scale of surface melting or laser plasma formation. A considerable amount of the laser energy is absorbed by the plasma, which reduces the direct laser irradiation at the metal surface. However, after the incident laser pulse has terminated, laser plasma will transfer part of its energy to metal by blackbody-like irradiation, which may eventually increase the thermal coupling between the laser and the nitrated metal. When the laser pulse duration drops to ps or fs, the most important difference compared to ns laser is that the laser-metal interaction is separated in time from the evaporation of metals. The laser plasma is produced after the laser pulse, once the laser plasma is formed, there will be no power supply from the incident laser, the laser enhanced thermal coupling doesn't work now. Particularly for fs Ti:sapphire laser, since the laser pulse length becomes shorter than the time needed to couple the excited electronic energy to the lattice, i.e., a few picoseconds, during the laser irradiation, thermal diffusion is insignificant, lattice atom desorption induced by electronic

transition or nonequilibrium electron heating becomes prominent [23, 129]. One interesting consequence is that the laser plume (after several ps) is produced even before the surface melting (after some hundred ps).

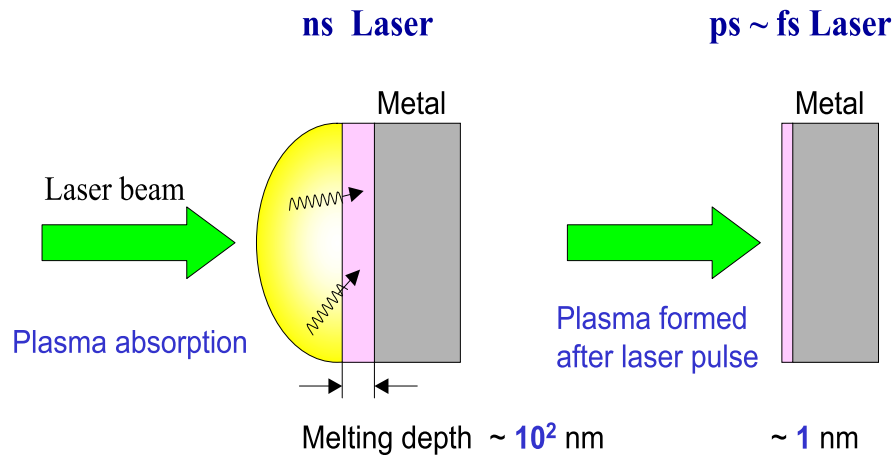


Figure 4-2: Schematic drawing of the laser-plasma-metal system under the irradiations of different pulsed lasers.

Due to the fundamental differences in the laser-plasma-metal system according to the pulse duration and laser intensity, it is expected that the pulsed laser series will lead to a better understanding of the laser nitriding mechanism and also the crucial role of laser plasma.

4.2 Description of pulsed laser types

In our investigations, a ns XeCl excimer and Nd-YAG laser, a ps free electron laser (FEL) and a fs ultra fast Ti:sapphire laser were utilized. A brief introduction to these pulsed lasers is presented as follows.

a) In the development of laser technology, excimer lasers operating in the ultra-violet may be considered as the third generation of industrial lasers. The short wavelength or high photon energy of excimer lasers led to a wide range of new applications. The lasing mechanism of the excimer laser is illustrated in Figure 4-3.

Noble Gas Halide Laser

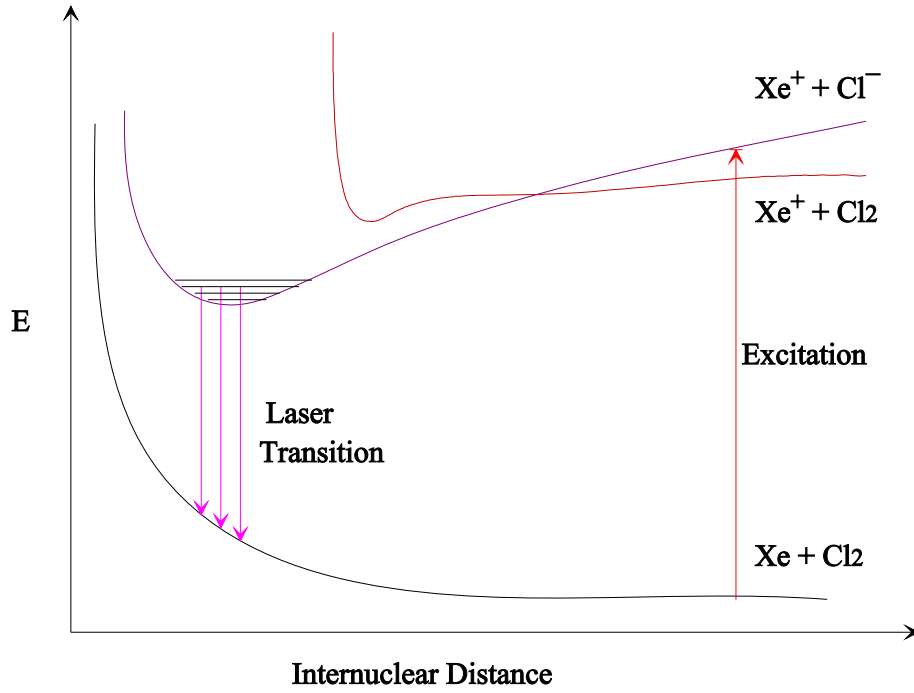


Figure 4-3: Energy levels and lasing mechanism of a XeCl excimer laser.

Excimer stands for excited dimer, a diatomic molecule consisting of an inert gas atom and a halide atom, which are bound in excited states only. These diatomic molecules have very short lifetimes and dissociate releasing the excitation energy through UV photons.

The various gas combinations, when electrically excited, produce a pseudo molecule (called a "dimer") with an energy level configuration that causes the generation of a specific UV laser wavelength emission as given in Table IV-1.

Table IV-1. List of different types of excimer lasers

Laser Media	Wavelength
Argon Fluoride	193 nm
Krypton Chloride	222 nm
Krypton Fluoride	248 nm
Xenon Chloride	308 nm
Xenon Fluoride	351 nm

Systems operating at average powers of 50-100 W are commercially available. A typical excimer operates in a pulsed mode of 30-40 ns pulses at a repetition rate up to 50 Hz with pulse energies of 1-2 J/pulse.

Until fairly recently, excimer lasers were more commonly found in the research laboratory where they are used either as a specific UV source or, in many cases, to serve as a "pumping" or exciting source to generate visible laser emissions. In the latter case, the excimer's UV output is directed into a tunable dye laser or Raman shifter module and converted into a modestly high power visible frequency emission.

Excimer lasers are now making the transition from the lab to the production area for a few unique uses in industry or in the operating room for exploratory surgical applications

The excimer laser in our experiment is Siemens XP2020 XeCl excimer laser, the wavelength λ is 308 nm with the pulse duration of 55 ns (FWHM) and a maximum pulse energy of 4 J. The size of the homogenized excimer laser is 5 mm \times 5 mm.

b) Solid state lasers have grown immensely in brightness since the operation of the first ruby laser and promise to do so again with the advent of diode lasers as a new pumping source. Diode lasers transfer the energy to the solid material much more efficiently than flashlamps allowing much higher average loading levels. Added advantages are the stability, reliability, and increased lifetime.

The gain medium in a solid-state laser is an impurity center in a crystal or glass.

Solid-state lasers made from semiconductors are described below. The first laser was a ruby crystal (Cr^{3+} in Al_2O_3) that lased at 694 nm when pumped by a flashlamp. The most commonly used solid-state laser is one with Nd^{3+} in a $\text{Y}_3\text{Al}_5\text{O}_8$ (YAG) or YLiF_4 (YLF) crystal or in a glass. These Nd^{3+} lasers operate either pulsed or cw and lase at approximately 1064 nm. The high energy of pulsed Nd^{3+} :YAG lasers allow efficient frequency doubling (532 nm), tripling (355 nm), or quadrupling (266 nm), and the 532 nm and 355 nm beams are commonly used to pump tunable dye lasers.

The Nd:YAG laser is optically pumped either by tungsten or krypton pump lamps and is capable of CW outputs approaching 1000 W at the 1.06 μm wavelength. The ends of the crystal, which is usually in the form of a rod, are lapped, polished, and may be coated to provide the cavity mirrors.

Although solid-state lasers offer some unique advantages over gas lasers, crystals are not ideal cavities or perfect laser media. Real crystals contain refractive index variations that distort the wavefront and mode structure of the laser. High power operation causes thermal expansion of the crystal that alters the effective cavity dimensions and thus changes the modes. The laser crystals are cooled by air or a liquid, particularly at high repetition rates.

In our investigations, the Nd-YAG laser was operated in BIAS Bremen, with the wavelength of 1.06 μm , pulse duration of 8 ns and the energy density of 2.34 J/cm², the pulse repetition rate was 10 Hz.

c) In its most common implementation, a Free-Electron Laser (FEL) feeds a beam of (high energy) electrons from a particle accelerator through a line of alternating magnets called an undulator or wiggler. The magnetic field causes the electrons to wiggle when they travel through the undulator and the electrons will emit radiation as their velocity changes [130]. Most particle accelerators deliver a train of electron pulses.

The interaction of the electrons with the combined magnetic and radiation field

results in a periodic force on the electrons. As a result a velocity spread is induced on the electrons in the electron beam. After the electrons have propagated a certain distance, this velocity modulation is translated into a density modulation on the electron beam, i.e., bunches are formed approximately a radiation wavelength apart. Therefore the electron beam is capable of amplifying a radiation field coherently. Mirrors are used to reflect the radiation back and forth through the undulator. The cavity length is chosen such that the optical pulse overlaps with a fresh electron pulse after one round trip at the entrance of the undulator. The efficiency of the FEL depends on the wavelength generated and can vary from tens of percent at mm wavelengths to a fraction of a percent in the UV. However since the energy stored in the electron beam increases as the wavelength decrease, high peak powers can be produced at all wavelengths. The efficiency of a FEL can be enhanced in two ways, first a non-uniform undulator can be used to increase the extraction efficiency. Second the energy stored in the electron beam after the interaction can be recovered, thereby increasing the overall efficiency of the system.

The wavelength and spectral width are determined by the number and spacing period of the magnets and the energy of the electrons. Therefore the FEL can be tuned in principle over a very large wavelength range from m to nm. However this range is limited in practice by the type of particle accelerator used (which fixes the energy range covered) and the fact that undulators have a fixed period and only the strength of the magnetic field can be varied within certain limits. Nevertheless the tuning range which can be obtained with FELs is in general much larger than those obtained with conventional lasers. Typical electron beam energies are tens of MeV and an undulator period of several centimeters. FELs have also been operated in the UV, visible and radar wavelength regime. In general the undulator period must be reduced and the electron beam energy increased to obtain shorter wavelengths. The wavelength tunability, high efficiency and reliability can make the FEL very attractive for industrial applications.

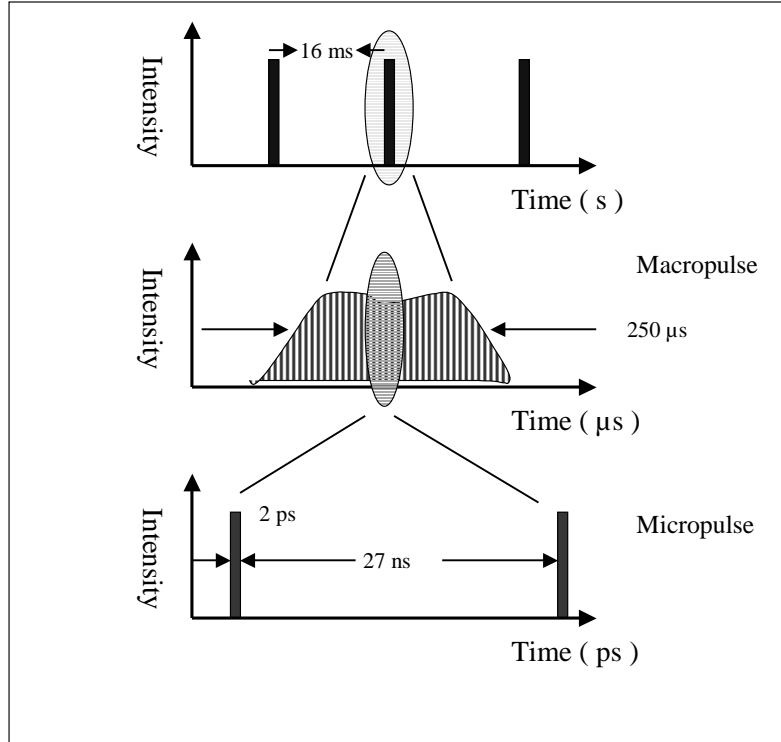


Figure 4-4: Time structure of FEL macro- and micropulses in Jefferson Lab.

Nitriding of iron with ultra short pulsed FEL was performed in the Jefferson Lab, Virginia. The IR Demo FEL driven by the superconducting RF linear accelerator with recycled electron beams provide the high intensity IR laser ($\lambda = 3.13 \mu\text{m}$) with maximum mean power of 1.7 kW. It was operated in pulsed mode with 250 μs macropulses consisting of 2 ps micropulses at the repetition rate of 37.4 MHz or 18.7 MHz and also CW mode. The energy of single micropulse of FEL is 17 μJ . The time structures of the FEL macro and micro pulses are illustrated in Figure 4-4.

d) The ultra short fs laser is discovered based on the mode-lock technique. Mode-locked lasers operate as a result of the resonant modes of the optical cavity which can affect the characteristics of the output beam. When the phases of different frequency modes are synchronized, i.e., "locked together," the different modes will interfere

with one another to generate a beat. The result is a laser output which is observed as regularly spaced pulsations. Lasers operating in this mode-locked fashion, usually produce a train of regularly spaced pulses, each having a duration of 10^{-15} to 10^{-12} sec. A mode-locked laser can deliver extremely high peak powers of 10^{12} W.

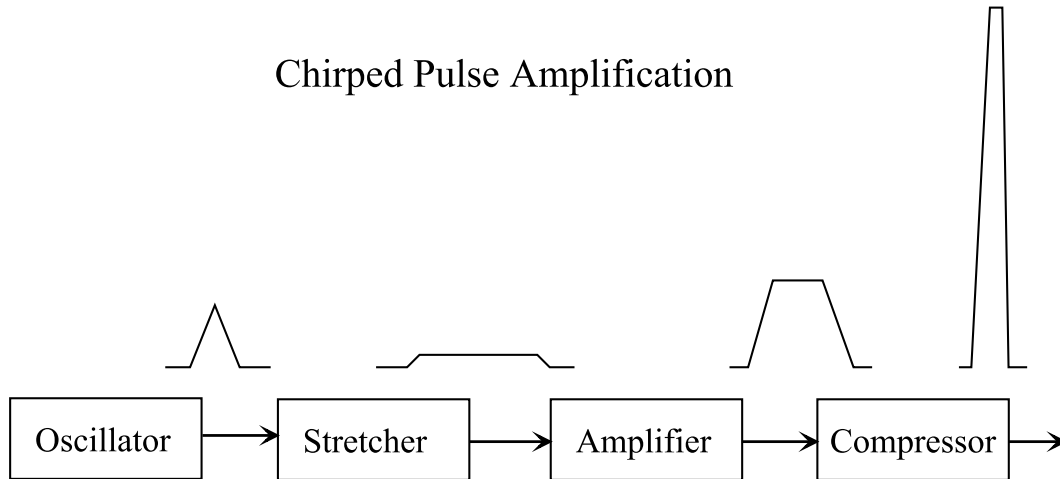


Figure 4-5: Chirped laser amplification technique for ultra short fs Ti:sapphire laser.

Ti:Sapphire fs laser we used is located in the Laser Zentrum Hannover (LZH). With chirped pulse amplifier, whose principal is illustrated in Figure 4-5, the output 150 fs pulse ($\lambda = 780$ nm) could reach the single pulse energy of 1 mJ with the repetition rate of 1 KHz.

In summary, the basic parameters of the short and ultra short pulsed laser utilized in our investigations are listed in table IV-2 as follows.

Table IV-2. Fundamental parameters of different types of pulsed lasers

Laser type	Ti:sapphire LZH	FEL Jefferson Lab.	Nd-YAG BIAS Bremen	XeCl Göttingen
Wavelength λ	780 - 850 nm	3.13 μm	1.06 μm	308 nm
Pulse duration τ	120 - 150 fs	2 ps	8 ns	55 ns
Pulse energy E	1 mJ	17 μJ	900 mJ	1 J
Laser intensity (W/cm^2)	1.2×10^{13}	$10^9 \sim 10^{10}$	2.9×10^8	8×10^7
Repetition rate f_p	1 kHz	37 MHz	10 Hz	1 Hz

4.3 Nitriding efficiency comparison

In the following sections, the nitriding efficiencies of different types of pulsed lasers are discussed base on the nitrogen content and the surface phase compositions. The nitrided metals under investigation are iron, stainless steel and titanium [30].

4.3.1 Nitrogen depth profile

Figure 4-6 shows the nitrogen concentration profiles of iron samples, which were treated by the four types of lasers introduced before. The excimer laser nitrided iron maintains a high nitrogen content: nearly 30 at.% at the surface and 10 at.% in the depth of 400 nm. In Nd-YAG laser nitrided iron (in N_2) the nitrogen content is slightly lower. It reaches a maximum of 20 at.% at the surface and nearly vanishes in the depth of 400 nm. In air the nitrogen concentration reaches maximum of 11 at.% at a depth of 200 nm, then remains nearly constant up to 400 nm. It is due to the formation of the surface oxide layer. Since oxygen is chemically more active to form iron oxides in the surface, but has no solubility in molten iron.

For FEL, there is very little nitriding effects, the maximum nitrogen concentration is less than 3 at.%. For fs Ti:sapphire laser, the nitriding efficiency is greatly

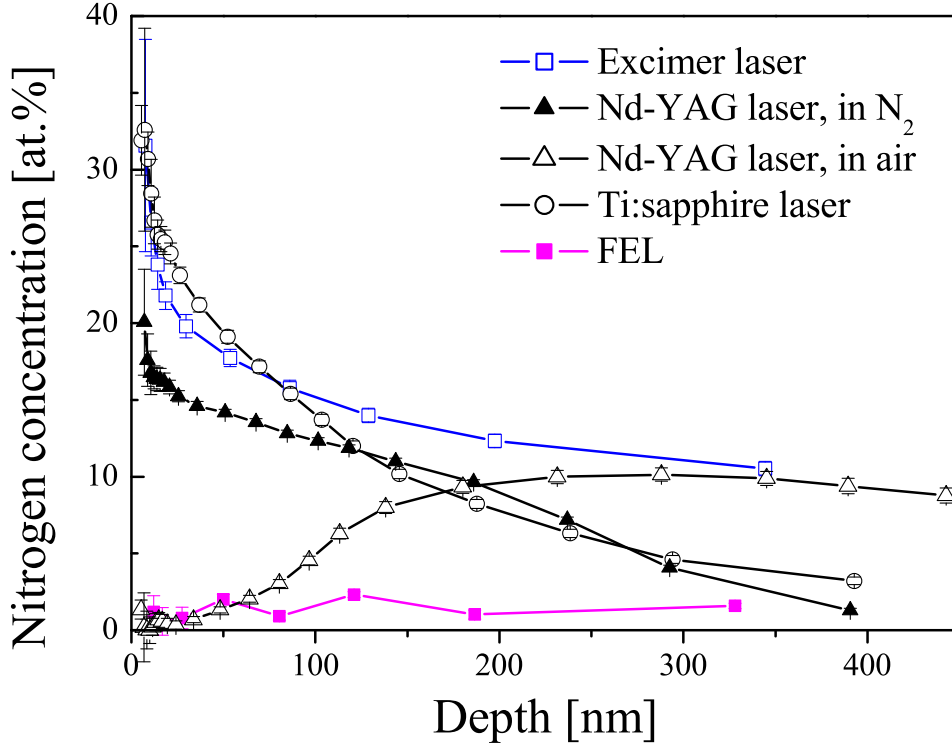


Figure 4-6: Nitrogen depth profiles of excimer laser, Nd-YAG laser, FEL and Ti:sapphire laser nitrided iron samples ($p_0 = 1$ bar). One sample is also treated by Nd-YAG laser in air.

improved and even comparable to that of Nd-YAG laser or XeCl laser. It is a surprising result since for fs laser, a much short melting time and molten depth of iron are to be expected compared to ns laser. If the nitrogen take up is simply determined by the nitrogen diffusion in molten iron, such a high nitriding efficiency is not understandable.

Since the nitrogen depth profiles in iron nitrided by different types of pulsed lasers, do not reveal what phases are produced due to ultra fast cooling and non-thermal effects. In the following section, phase analysis is conducted by the combination of GIXRD and CEMS measurements.

4.3.2 Surface phase composition

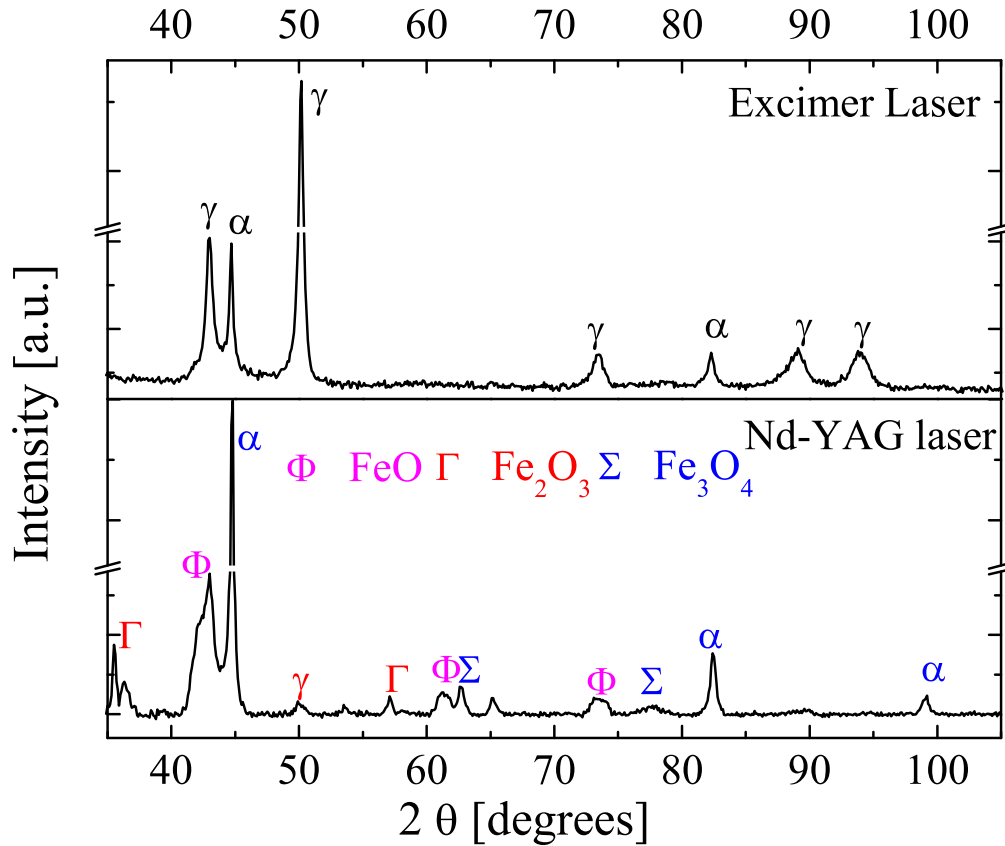


Figure 4-7: GIXRD spectra of excimer laser (in N_2) and Nd-YAG laser (in air) nitrided iron samples.

The GIXRD spectra of iron taken at 5° incidence after irradiations with the four types of lasers are plotted in Figure 4-7 and Figure 4-8. In excimer laser nitrided iron, the dominant nitride phase is γ - $\text{Fe}(\text{N})$. In the GIXRD spectrum of Nd-YAG laser nitrided iron in air, there are many diffraction peaks of iron oxides, such as FeO , Fe_2O_3 and Fe_3O_4 , the signal from iron nitrides is quite weak probably because most of them are buried below the surface iron oxides.

In Figure 4-8, it is interesting to find that for both FEL and Ti:sapphire laser

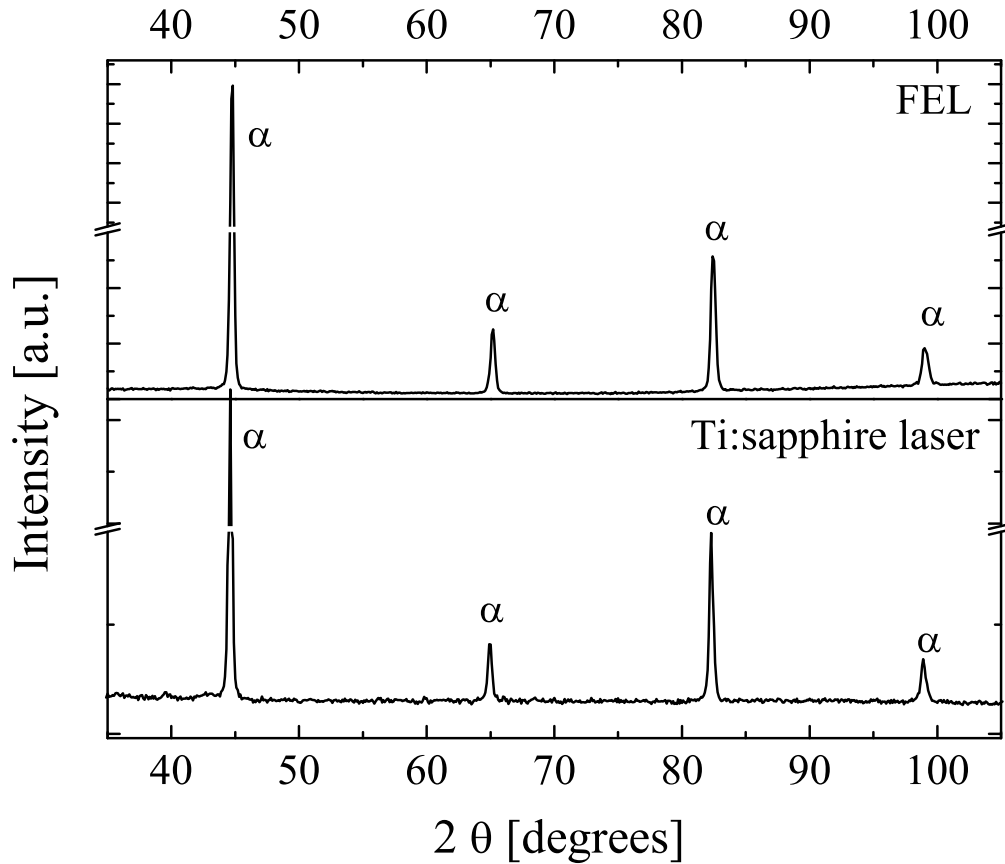


Figure 4-8: GIXRD spectra of FEL and Ti:sapphire laser nitrided iron samples.

nitrided iron, the diffraction patterns look exactly like the virgin α - Fe. For FEL nitrided iron, this is to be expected since RNRA has revealed a very low nitrogen contents (see Figure 4-6). However, for Ti:sapphire laser nitrided iron, this seems to be in conflict with the mean nitrogen concentration of nearly 17 at.% as deduced from RNRA. The missing nitrogen content suggests that the iron nitride produced by fs laser may not have the normal polycrystalline phases. ^{57}Fe CEMS was also utilized to characterize the iron nitride phases within the sensing depth of about 150 nm. One of its advantages is its sensitivity to amorphous phases which is invisible in the GIXRD measurement [136]. As shown in Figure 4-9, CEMS spectrum of excimer laser nitrided

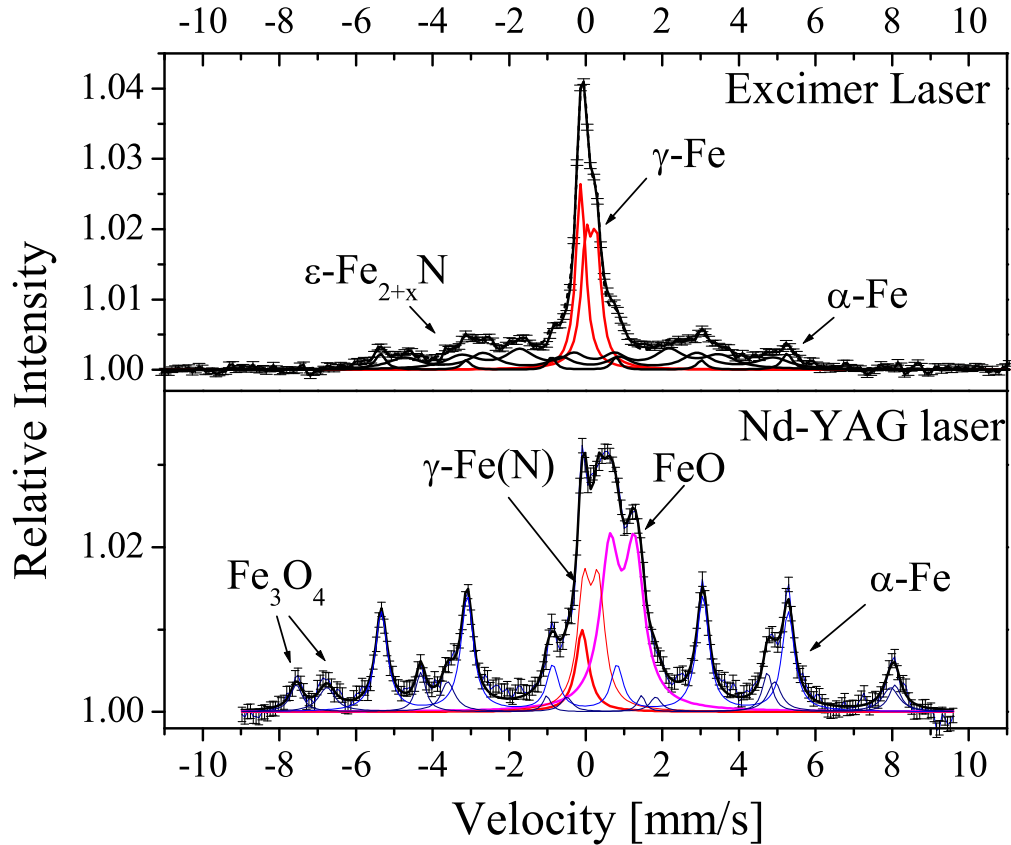


Figure 4-9: CEMS spectra of excimer laser (in N_2) and Nd-YAG laser (in air) nitrided iron samples.

iron agrees with the previous RNRA and GIXRD measurements. The main iron nitride phase are γ -Fe(N) phase, ϵ -Fe $_{2+x}$ N phase and α' -Fe(N) phase (martensite). However, the area ratio of ϵ phase in the CEMS spectrum is much higher than in the GIXRD spectrum. It means that the ϵ phase is distributed mainly in the very surface, rather than in deeper depths where the γ -Fe(N) dominates. For iron irradiated with Nd-YAG laser in air, the complicated CEMS spectrum is fitted with the superposition of α -Fe, γ -Fe(N), FeO and Fe $_3$ O $_4$ iron oxides phase. The area ratio of the iron oxides exceed 40%. The only nitride phase presenting in the CEMS sensing depth is γ -

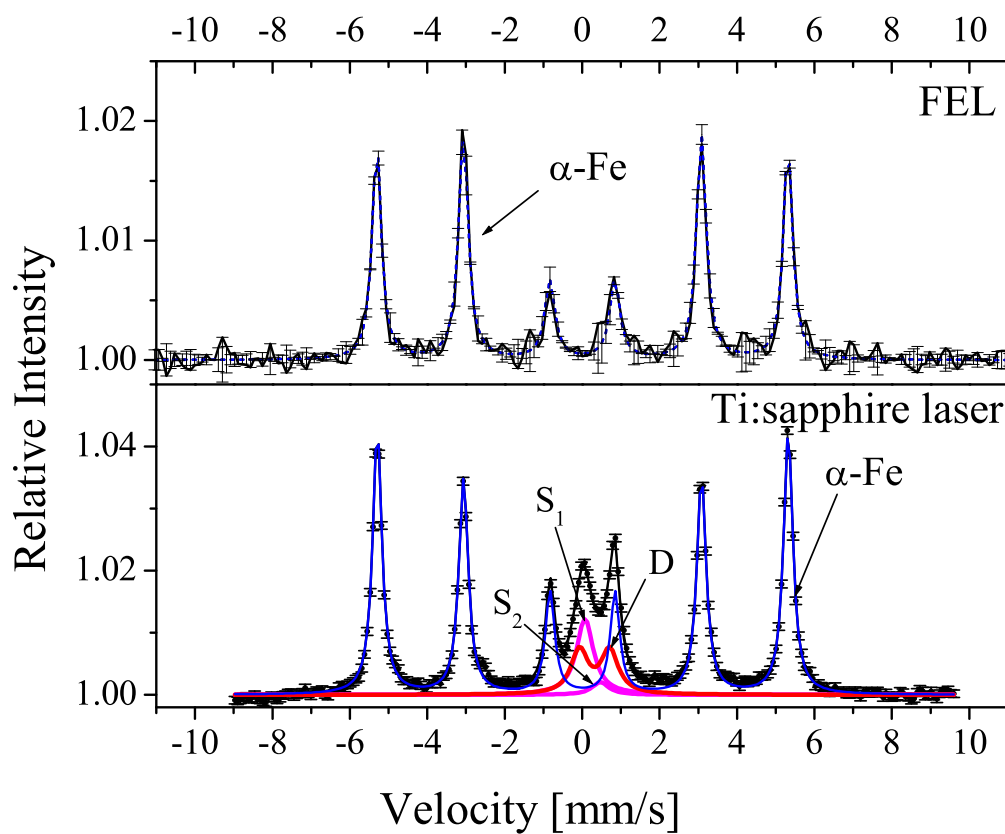


Figure 4-10: CEMS spectra of FEL and Ti:sapphire laser nitrided iron samples.

Fe(N).

Figure 4-10 shows the CEMS spectra of iron irradiated by ultra short FEL and Ti:sapphire laser. There are no new phases except for the original α - Fe in FEL nitrided iron, which agrees with the previous RNRA and GIXRD results. Though the laser intensity of the FEL is much higher than that of the Nd-YAG or excimer laser, both the high reflectivity of iron for $3.13 \mu\text{m}$ IR FEL and the ultra short pulse duration of 2 ps probably hinder an efficient nitriding. When the laser duration drops to fs, RNRA revealed a considerable nitrogen take up, but the iron nitride phase is completely invisible in GIXRD spectrum. Hopefully, CEMS could illuminate such a

paradox. The lower part of Figure 4-10 plots the CEMS spectrum of Ti:Sapphire laser nitrided iron. Two single lines (S_1 : IS=0.08(2) mm/s and S_2 : IS=0.48(3) mm/s) and a doublet (D: IS=0.34(2) mm/s, QS=0.78(4) mm/s) in addition to the virgin α iron sextet are adopted to fit the CEMS spectrum. The hyperfine parameters of the paramagnetic phase agree well with those of the γ'/γ'' - FeN phases prepared by reactive magnetron sputtering [131]. Since the area fraction of the paramagnetic phase counts only 21(3)%, in order to be consistent with the mean nitrogen concentration of about 16.5(7) at.% in the first 150 nm deduced from the RNRA measurement, this phase should contain 48(7) at.% nitrogen, corresponding to the stoichiometry of $FeN_{0.94(8)}$, very close to the supposed γ'/γ'' - FeN phase. The new FeN phase has an amorphous or nanocrystalline structure which most probably corresponds to the nitride fall out from the re-condensing plasma. Maybe, some FeN or FeN_2 molecules are directly formed in the plasma, then the subsequent fast cooling and clustering yields an amorphous or nanocrystalline iron nitride layer [132]. The amorphous or noncrystalline nature of the FeN phase explains why it is invisible in GIXRD, but remarkable both in CEMS and RNRA.

Finally, the surface hardness of laser nitrided iron or titanium was measured by the nanoindentation technique applying a force of 4 mN. As shown in Figure 4-11, large differences were found among metal samples nitrided by different lasers. Excimer laser nitrided iron achieves the maximum hardness of 5 GPa, Nd-YAG laser treated iron in air is softer due to the Fe_3O_4 and FeO iron oxides. The surface hardness of the fs laser irradiated iron is less than 0.7 GPa, even much lower than the virgin iron, corresponding to the amorphous or nanocrystalline structure produced by ultra fast Ti:sapphire laser.

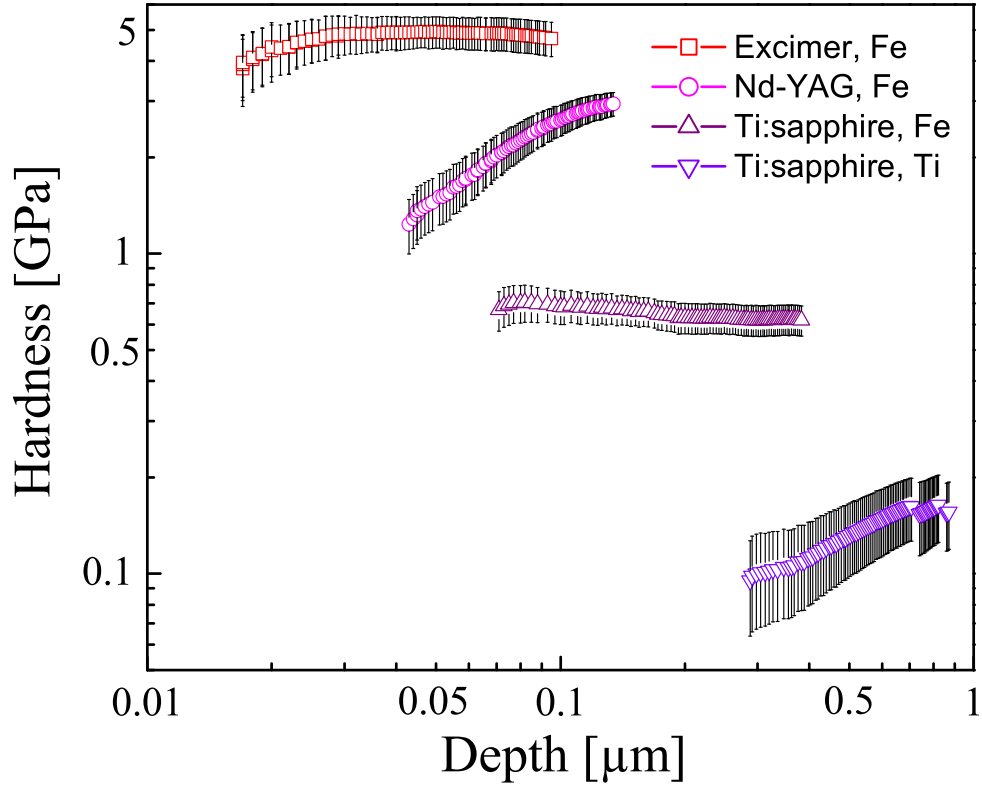


Figure 4-11: Surface hardness profiles of different types of pulsed laser nitrided iron and titanium.

4.4 Discussion of laser nitriding mechanisms

From the previous investigations, it has been found that ns excimer and Nd-YAG lasers lead to better nitriding efficiency compared to ps or fs ultra short pulsed laser. The following section will discuss the possible nitriding mechanisms for different types of pulsed lasers. Figure 4-12 presents the one dimensional thermal simulation of surface temperature and iron molten depth for 55 ns XeCl laser and 8 ns Nd-YAG laser [84, 34]. Since the energy equilibrium between electrons and phonons is reached after several ps, it is safe to adopt the thermal conduction equation to simulate the temperature profile during excimer or Nd-YAG laser irradiation but not for FEL and

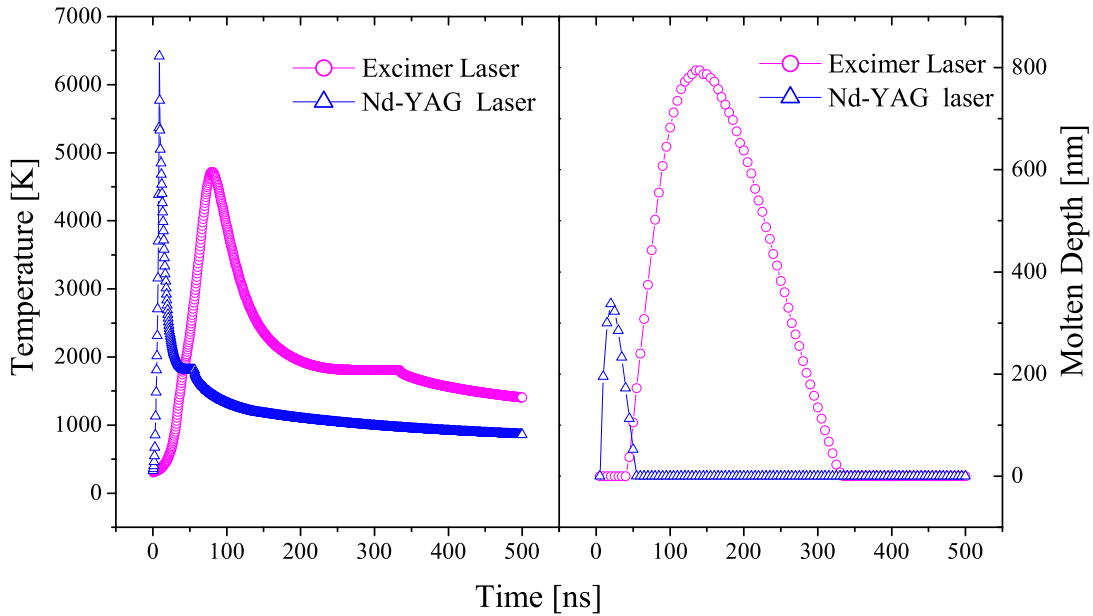


Figure 4-12: Simulation of the surface temperature and the molten depth of iron as the functions of time (Excimer laser: $H = 4 \text{ J/cm}^2$, Nd-YAG laser: $H = 2.34 \text{ J/cm}^2$).

Ti:sapphire laser, where the non-thermal effects become prominent during the ps or fs laser irradiation. The simulated temperature profiles are shown in Figure 4-12. Thickness of the molten iron layer is about 800 nm for excimer laser, 350 nm for Nd-YAG laser, and the melting time is 300 ns for excimer laser, 60 ns for Nd-YAG laser. It is clear that as the pulse duration decreases, both the melting time and the molten iron depth decreases rapidly. The thermal simulation clearly demonstrates that longer pulsed laser maintains longer melting time and deeper molten depth, which are the most crucial factors determining an efficient nitrogen diffusion. It is believed that the laser nitriding efficiency is primarily determined by a fully developed nitrogen diffusion process in the molten metals.

The most remarkable fact revealed by the Nd-YAG laser experiment is that IR laser nitriding of metal actually works. Due to the high reflectivity of IR laser for iron, normally it will not produce a considerable nitriding effect, as claimed by several

researchers [28]. However, in Figure 4-6, the nitrogen depth profile after IR Nd-YAG laser nitriding is comparable with UV XeCl laser, which has to be ascribed to the laser plasma formed after hundreds of picoseconds. Due to the much lower electron density in the plasma than that in metals, the plasma frequency of the laser plasma is at least two orders lower than in metals, thus the IR laser is highly reflective for metals but not for laser plasma. More fraction of the incident IR laser is absorbed instead of being reflected back, then the absorbed energy is partially returned back to the metal via blackbody-like irradiation from the laser plasma, leading to the enhanced laser-metal energy coupling and eventually improving the nitriding efficiency.

Compared to ns laser, FEL nitriding of iron exhibits extremely low nitriding efficiency. It is supposed that the ps FEL micropulses with 10^7 Hz repetition rate actually resemble a μ s or CW laser, but the surface iron must obtain a much higher peak temperature during the micropulse irradiation compared to normal CW laser owing to the time structure of the FEL laser pulse (see Figure 4-4), thus the degassing or the depletion of the nitrogen is greatly enhanced, resulting in the low nitriding efficiency of FEL. For fs laser, it is surprising to observe a 400 nm thick iron nitride layer, which can not be formed by the normal nitrogen diffusion process due to the ultra short thermal diffusion distance (less than 10 nm). However, with extremely high laser intensity ($I_0 \approx 10^{13}$ W/cm²) fs laser, the ablated iron ions obtain much higher kinetic energy than in the case of ns laser. Maybe some FeN or FeN₂ molecules or clusters are formed directly in the highly ionized laser plume, then the following re-condensing of the plasma and the ultra fast cooling leads to an amorphous or nanocrystalline iron nitride structure, as confirmed by the GIXRD and CEMS phase analysis. However, since normally the amorphous metal nitrides have poor mechanic properties and thermal stability, it is not favorable coating compared to crystalline phase.

4.5 Laser nitriding of titanium

In the past decades, ceramic thin film gained widespread applications and increasing importance. Tribological and electronic properties of these films are crucial for many applications such as cutting tools and functional layers for electronic and optical applications. Titanium nitrides are of special interest due to their extremely high hardness and high melting temperature like co-valent crystals, and excellent electronic and thermal conductivity of typical pure metals [133, 134]. They also possess high corrosion resistance to protect technical alloys and have diffusion barrier properties against copper diffusion in silicon integrated microelectronics technology. It is natural to extend the idea of pulsed laser nitriding to metals other than iron or steel. Titanium seems to be one of the promising candidates for pulsed laser nitriding, not only because of the attractive properties of titanium nitrides, but also of the fact that titanium is easier to transform to titanium nitrides. Another motivation for the titanium nitriding experiment is related to the laser nitriding mechanism, since the thermal parameters of titanium such as melting temperature and thermal conductivity are quite close to iron, the main difference between titanium and iron is the chemical activity with nitrogen. If the laser nitriding process is nitrogen diffusion dominated, no big differences would be expected.

To have an idea of the efficiency of pulsed laser nitriding of titanium, the first experiment was conducted using 64 pulses of homogeneous XeCl excimer laser, the energy density of each pulse was 4 J/cm^2 , and the ambient nitrogen pressure ranged from 0.5 bar to 2 bar. As shown in Figure 4-13, the most remarkable feature of the laser nitrided titanium is the extremely high nitrogen content at 1 bar and 2 bar. There are no significant nitriding effects at 0.3 bar when the laser ablation is dominated. At 2 bar, the stoichiometry of the laser nitrided titanium is quite close to TiN. Even at the depth of 350 nm, the nitrogen concentration still exceeds 30 at.%. Compared to the nitriding of iron under same conditions, laser nitriding of titanium achieves a much higher efficiency than nitriding of iron.

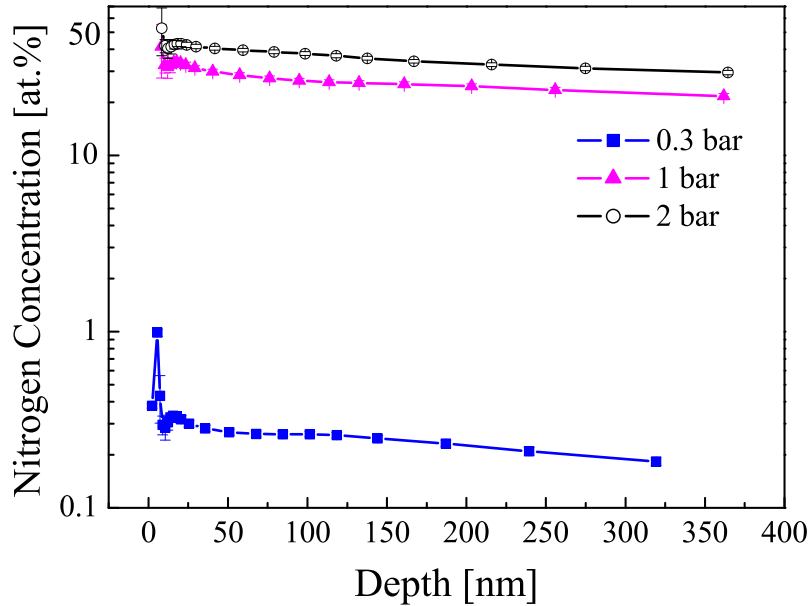


Figure 4-13: Nitrogen concentration profiles of excimer laser nitrided titanium at different nitrogen pressures.

In the previous discussion, it has been found that for decreasing pulse length, laser nitriding of iron becomes less efficient since the diffusion time of nitrogen is greatly reduced. Then how about the ultra short laser nitriding of titanium?

Figure 4-14 compares the normalized γ -ray yield of RNRA (proportional to the nitrogen concentration) among FEL nitrided titanium, iron and stainless steel. The normalized yield of FEL nitrided titanium is by a factor of 30 higher than iron or stainless steel. Since the laser parameters such as energy density, repetition rate and beam size are same, the big difference of nitrogen content suggests that nitrogen take up is not simply determined by nitrogen diffusion, the degassing effect during the laser irradiation is also critical. It seems that the nitrogen degassing effect is more prominent in iron or stainless steel than in titanium.

As shown in Figure 4-13, the mean nitrogen concentration in laser nitrided titanium sample is 25 - 50 at.%, so probably TiN is the dominant surface phase. GIXRD

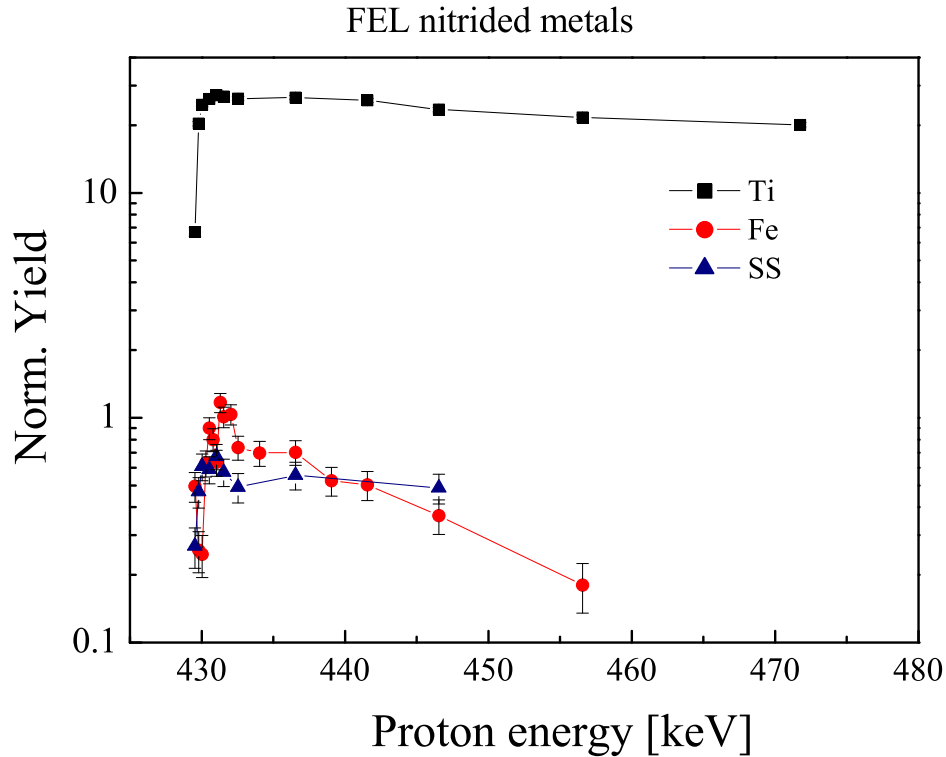


Figure 4-14: Comparison of normalized yield of γ -ray in RNRA among FEL nitrated titanium, iron and stainless steel.

spectra of excimer laser and FEL nitrated titanium samples are shown in Figure 4-15, the diffraction peaks of f.c.c. TiN are clearly distinguished from the hexagonal Ti substrate, but the peaks from other titanium nitride phases have not been found.

It is worth mentioning that the diffraction peaks of TiN in FEL nitrated titanium are even sharper than in the excimer laser nitrated titanium. According to the Scherrer equation, the mean grain size of titanium nitrides produced by FEL and excimer laser are estimated to be 150 nm and 75 nm, respectively. The comparison of the grain size contradicts to the general rule that a higher cooling rate leads to a smaller crystal grain size, the ps FEL nitrated titanium surface layer must remain molten for a longer time than ns excimer laser nitrated titanium. Although at first sight the result

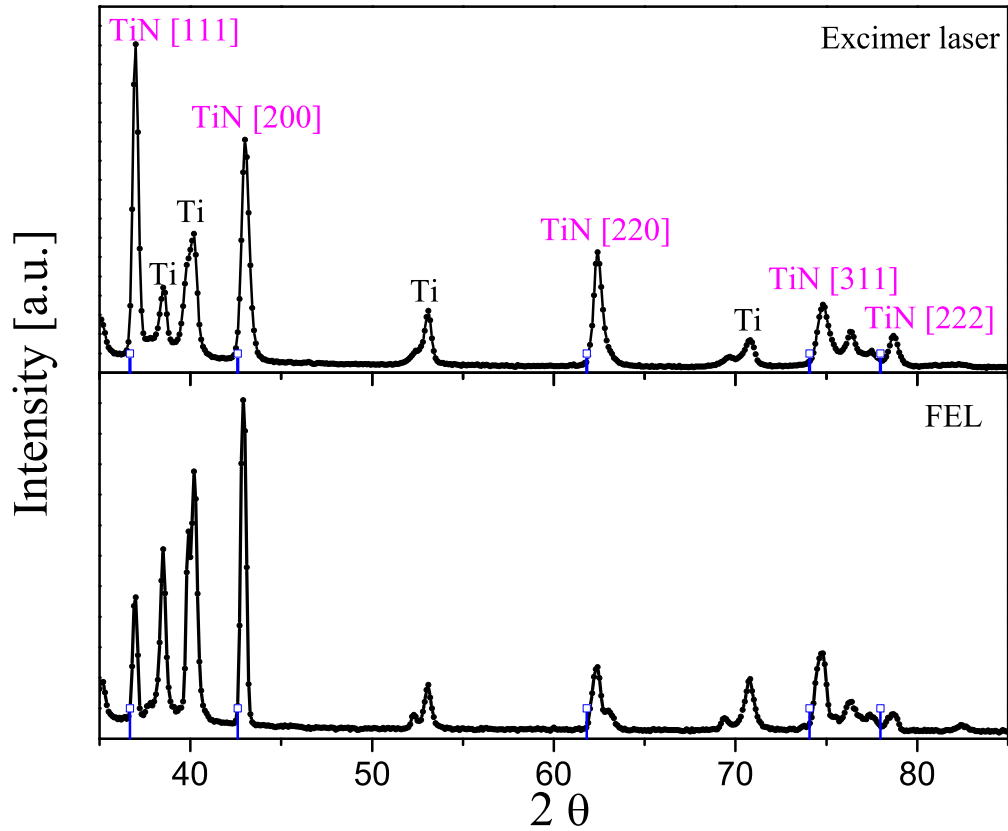


Figure 4-15: GIXRD spectra of excimer laser and FEL nitrided titanium.

looks little strange, the high 10^7 Hz repetition rate reduces the time interval among FEL micropulses to be merely tens of nanoseconds, probably even shorter than the melting duration produced by previous micropulse, thus in principal the FEL laser is equivalent to a μ s or CW laser with a mean intensity of $10^5 \sim 10^6$ W/cm², which ensures the bulk melting of the surface titanium layer. Due to the high intensity of FEL micropulse ($10^9 \sim 10^{10}$ W/cm²), the enhanced degassing rate in iron leads to an extremely low nitriding efficiency. Contrastively the high nitrogen content in titanium under the same nitriding conditions strongly favors the supposition of the reduced degassing rate in titanium, which will be confirmed by the annealing experiments in

the next chapter.

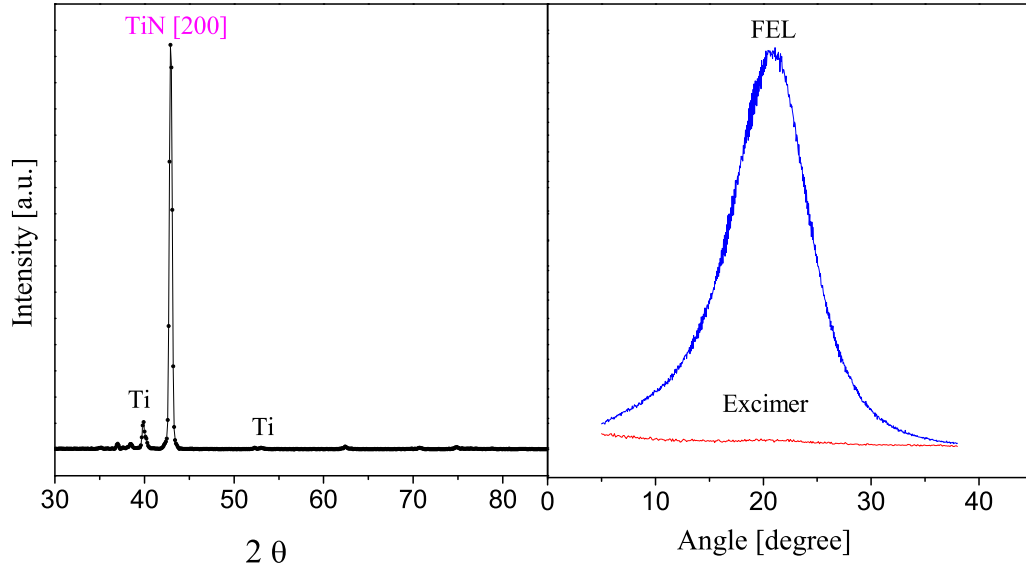


Figure 4-16: GIXRD spectrum of FEL nitrated titanium and rocking curve measurement of TiN $\langle 200 \rangle$ peak for excimer laser and FEL nitrated titanium.

In order to check the thickness of the nitrated layer and also the possible texture induced by the FEL treatment, a locked θ - 2θ scan of FEL nitrated titanium was conducted, the spectrum is shown in left part of Figure 4-16. The most remarkable fact is the high diffraction intensity of the TiN $\langle 200 \rangle$ peak, which suggests a $\langle 200 \rangle$ texture. The rocking curve measurement of the TiN $\langle 200 \rangle$ peak is plotted at the right part of Figure 4-16. The $\langle 200 \rangle$ texture in FEL nitrated titanium is clearly demonstrated while the excimer laser nitrated Ti does not exhibit a similar texture. It is known that $\langle 200 \rangle$ is the TiN surface with lowest surface energy [135], thermodynamically $\langle 200 \rangle$ texture is more favorable. On the other hand, the elastic constant in $\langle 111 \rangle$ direction is lower than in $\langle 200 \rangle$ direction, thus $\langle 111 \rangle$ is a plane with lower strain energy compared to $\langle 200 \rangle$ plane [135]. In this aspect, $\langle 111 \rangle$ texture is more favorable. Based on these considerations, it is supposed that the strain energy

in excimer laser nitride titanium is dominant while surface energy is more important in FEL nitrided titanium.

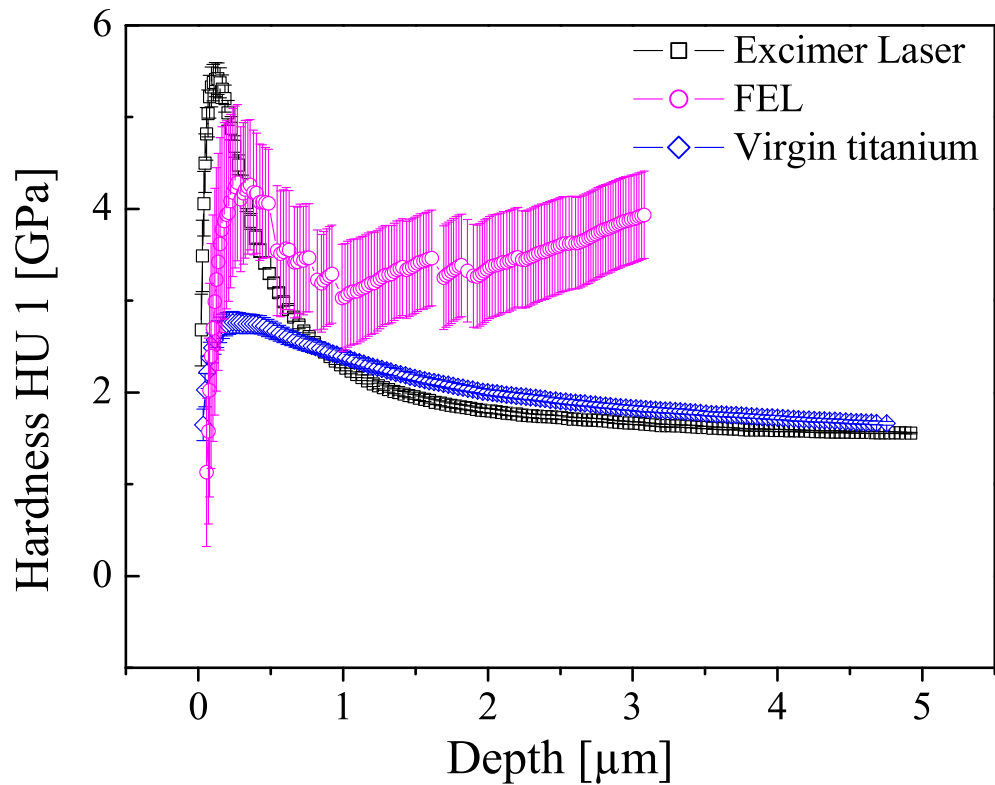


Figure 4-17: Surface hardness profile of excimer laser and FEL nitrided titanium compared to virgin titanium.

Because of the diamond like hardness of TiN, surface hardness profiles of excimer laser and FEL nitrided titanium were measured by nanoindentation, the results are plotted in Figure 4-17. Both nitriding treatments nearly doubled the surface hardness. The maximum hardness in the surface is about 5 GPa. FEL nitriding achieved a deeper nitriding depth compared to excimer laser, which is possibly related to the deeper molten layer produced by the FEL than the excimer laser. The hardness profile of FEL nitrided titanium is not smooth due to a rough surface.

From the investigation of the laser nitriding of titanium, particularly the FEL nitrided titanium, a crystalline titanium nitride layer with nearly 50 at.% nitrogen content and doubled surface hardness was confirmed. Bulk molten state is produced by the FEL. Since the thermal and optical parameters of iron and titanium are quite similar, degassing effects and phase formation are believed to be the main reasons resulting in the very different nitriding efficiencies of titanium and iron. Compared to ns excimer laser, FEL induces much higher surface temperature due to its high intensity, thus the degassing effect would be greatly enhanced. Nevertheless, since titanium nitride is more stable than iron nitride, the nitrogen degassing process in titanium will most probably be suppressed, FEL nitriding of Ti can still maintain a high nitriding efficiency.

4.6 Summary

In this chapter the nitrogen content, nitride phase formation and hardness of Fe and Ti for various types of lasers were discussed, differing in the laser wavelengths, pulse duration and time structures (see Table IV-2). The following arguments appear to be most important to explain the similarities and differences.

1: The experimental finding and thermal simulations indicated that longer pulse led to better nitriding efficiency, which supported the opinion that efficient laser nitriding of metal is primarily based on nitrogen diffusion process.

2: IR Nd-YAG laser nitriding of iron exhibited good nitriding efficiency even comparable to UV excimer laser, which was ascribed to the enhanced laser-metal thermal coupling maintained by the laser plasma. The laser nitriding efficient was found to be more or less independent of the laser wavelength.

3: Although a high nitrogen concentration was detected in Ti:sapphire laser nitrided iron by RNRA, the GIXRD measurement excluded the existence of a crystalline iron nitride. An amorphous or nanocrystalline iron nitride layer with the stoichiom-

etry close to FeN was revealed by CEMS, which should correspond to the fall out of the re-condensing plasma followed by a ultra fast cooling and clustering process.

4: Since the ps FEL micropulses with high repetition rate of 10^7 Hz actually resemble a μ s or CW laser, a crystalline titanium nitride layer and a bulk melting of Ti substrate were produced by FEL, as confirmed by the GIXRD measurements. The comparison between FEL nitrated Fe and Ti revealed that the laser nitriding efficiency is essentially determined by the competing between the nitrogen take up (nitrogen diffusion) and the nitrogen depletion (degassing process). It is supposed that the reduced nitrogen degassing rate in Ti is the main reason for the improved FEL nitriding efficiency of Ti.

Chapter 5

Thermal stability of laser produced iron/titanium nitrides

In chapter 3 and 4, detailed informations of nitrogen concentration profiles and surface layer phase compositions in pulsed laser nitrided iron, stainless steel and titanium were given. The influences of the ambient nitrogen pressure and the laser pulse duration on the nitriding efficiency were investigated and qualitatively discussed. However, up to now, there is still little knowledge about the thermal stability of the laser produced metal nitrides [29], which is critical for potential applications. In the following section, the thermal stability of the metal nitrides is investigated by annealing experiments, which are conducted both in vacuum and air. In detail, 2 hour isochronal annealings were carried out between room temperature (RT) and 973 K. The evolution of the phase and elemental composition and hardness of the surface layer were obtained from the well-suited selection of methods: RNRA, CEMS, GIXRD and nanoindentation. Since iron and stainless steel are the most popular metals, most of the discussion will be confined to them. Also a couple of titanium samples after FEL and Ti:sapphire laser nitriding were investigated to test some assumptions of previous chapters.

5.1 Iron/titanium nitrides phase evolution during annealing treatment

5.1.1 In vacuum environment

In the following section, quantitative results are presented. Since the maximum proton energy available at IONAS is 530 keV, only the top 400 nm layer can be investigated via RNRA, while the nitrated layer reaches to about 1 μm according to the simulations [84]. Figure 5-1 shows the nitrogen concentration profiles in iron and stainless steel, from 0 to 400 nm at various annealing temperatures. RNRA revealed that nitrogen in stainless steel is more stable than in iron. For stainless steel, even at 773 K, there is still no big change in the nitrogen concentration except for the very surface, while for iron, there is nearly no nitrogen left at 773 K. Another interesting feature is that for the annealing step at 423 K, the nitrogen concentration in certain depths becomes larger than in the original laser-nitrated samples, more prominent for iron than for stainless steel.

CEMS was used to get the information on the phase composition and evolution in the iron nitride layers. Laser treatment of iron and stainless steel introduces nitrogen atoms mainly as interstitial solid solution (γ - phase). Figure 5-2 shows two typical CEMS spectra of laser nitrated iron and stainless steel. The spectrum of iron in Figure 5-2a is the superposition of several magnetic phases with different magnet hyperfine fields, such as the α, α' , and ϵ phase, and also the paramagnetic γ phase. Figure 5-2b shows the CEMS spectrum of stainless steel, whose principal structure is fcc γ -Fe with additional interstitial nitrogen atoms. As discussed in the previous chapters, the CEMS spectrum of stainless steel is composed of two groups of subspectra. The dotted single line (IS=-0.11(2) mm/s) and the dotted doublet (IS=-0.11(2) mm/s, QS=0.19(3) mm/s) are ascribed to the virgin stainless steel [100]. The solid doublet (IS=0.07(2) mm/s, QS=0.40(1) mm/s) with larger isomer shift is related to the laser

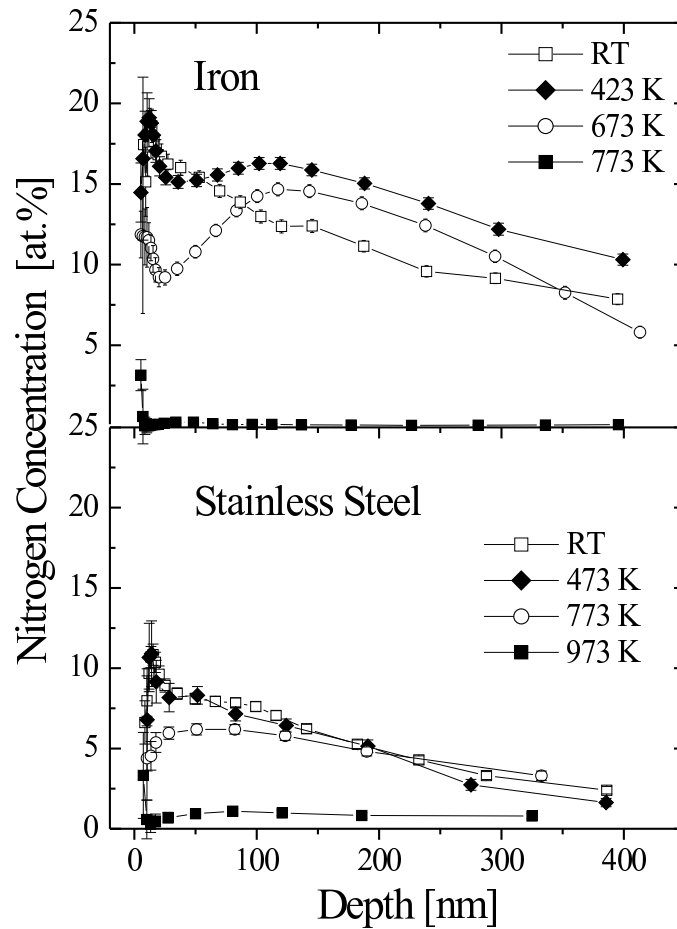


Figure 5-1: Nitrogen depth profiles for excimer laser nitrided iron and stainless steel annealed in vacuum (2 hours at each temperature).

produced fcc γ -Fe(N) austenite, corresponding to the microscopic geometry of one nearest nitrogen neighbor around the ^{57}Fe probe atom. All of the relevant hyperfine parameters agree well with the parameters of γ - Fe(N) austenite [25, 83].

The phase composition in iron and the subspectrum area fraction of stainless steel deduced from CEMS are plotted in Figure 5-3 as a functions of the annealing temperature. For iron, the main iron nitride phases after the laser treatment are the α' , α'' , ϵ and the γ iron nitride phase. When the annealing temperature reaches 473 K, the γ' phase appears, then gradually becomes the dominant phase around 523 K,

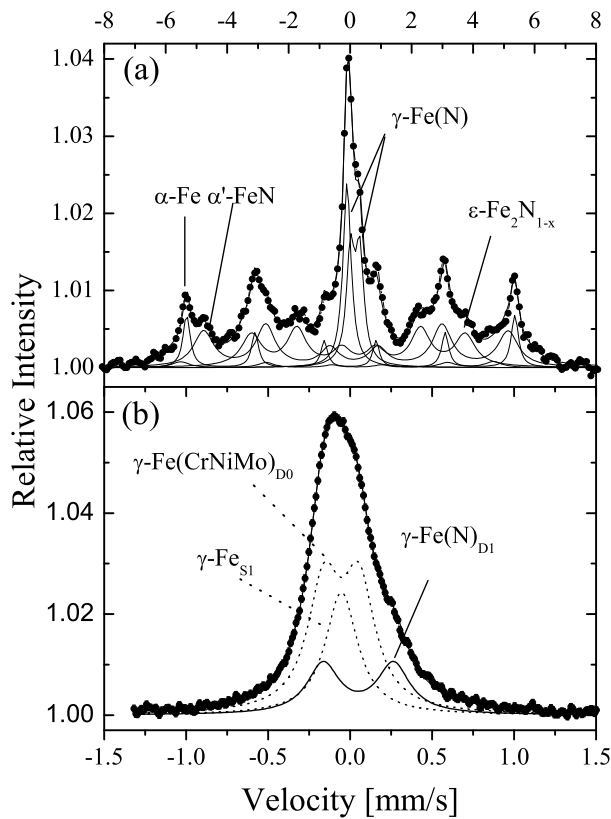


Figure 5-2: CEMS spectra of excimer laser irradiated iron and stainless steel with subspectra.

while the contribution from other phases is greatly reduced. When the temperature exceeds 773 K, there are no nitride phases presenting any more, the iron sample returns to the pure α phase. Stainless steel appears to be more stable than iron, and no new phases are created up to 973 K. The area fraction of the iron nitride doublet in stainless steel remains nearly constant up to 623 K.

One drawback of CEMS is that it is only sensitive to iron nitride phases. For stainless steel (CrNiMo1.4401) it is not sure whether other metal nitride phases such as CrN are produced after laser irradiation or during the annealing process. In the following section, GIXRD with a fixed incidence angle of 5° is utilized to extend the CEMS phase analysis. Figure 5-4 shows the XRD measurement results of iron and

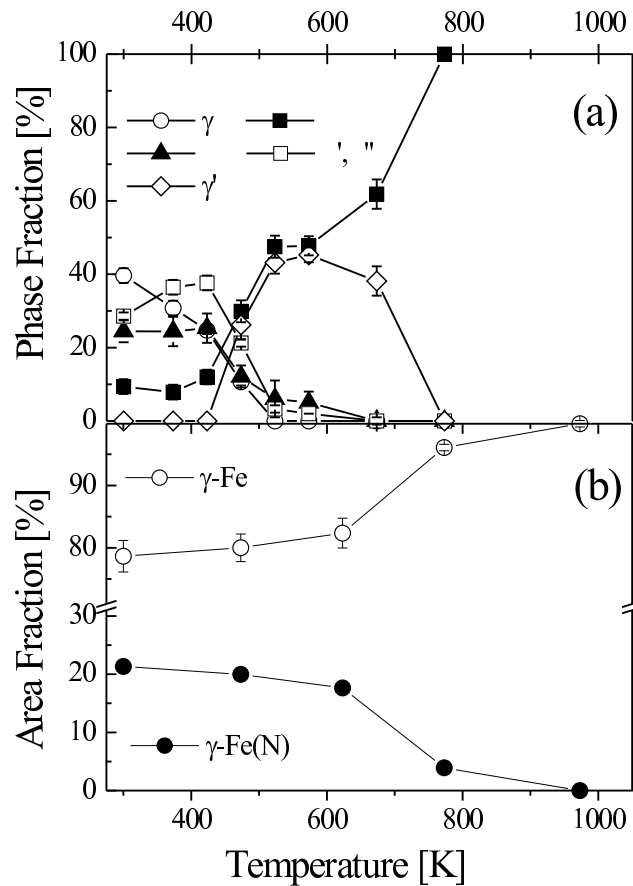


Figure 5-3: (a) Phase composition of excimer laser nitrided iron and (b) subspectral area fraction of excimer laser nitrided stainless steel revealed by CEMS as functions of annealing temperature.

stainless steel respectively.

The diffraction pattern of the iron sample in Figure 5-4a presents direct evidence for the critical temperatures of iron during the annealing process in vacuum. From 473 K, the γ' phase appears and then becomes the dominant iron nitride phase around 523 K. When the temperature exceeds 773 K, there are no diffraction peaks from iron nitride phases left. In the XRD spectra of the iron sample, the diffraction peaks of the ϵ iron nitride phase are hardly visible, while in the CEMS measurement results shown in Figure 5-3, the contribution of the ϵ phase can reach 20 %. The fact that XRD has a much deeper sampling range of about 750 nm can explain this discrepancy.

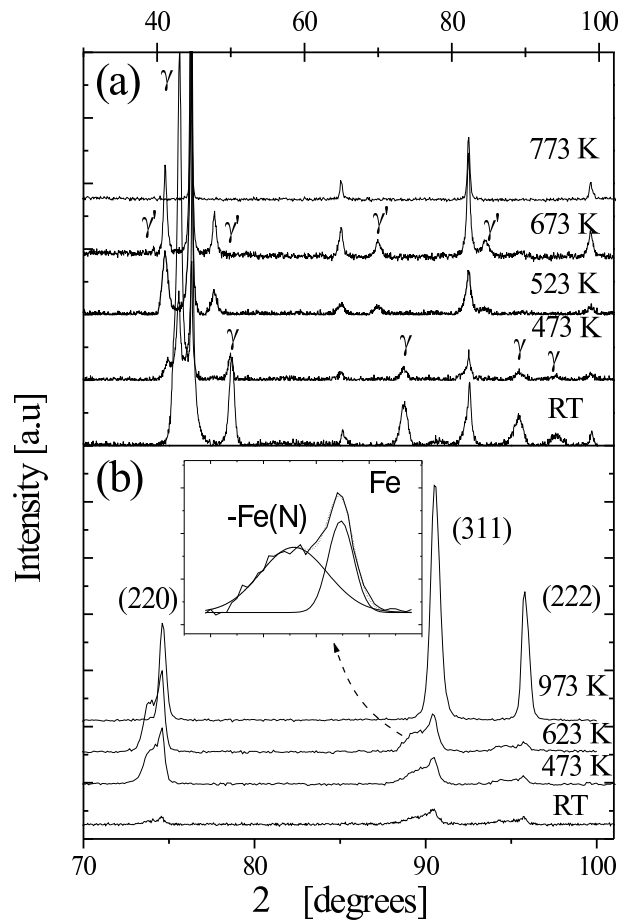


Figure 5-4: GIXRD spectra of excimer laser nitrided iron (a) and stainless steel (b) annealed in vacuum.

The comparison between CEMS and XRD reveals that the ϵ iron nitride is mainly distributed within the depth of 150 nm. Figure 5-4b shows the XRD spectra of stainless steel. There are no diffraction peaks from CrN or from other nitride phases which are invisible to CEMS. It seems that no other nitride phases are produced after laser irradiation. The diffraction spectra of stainless steel are composed of two groups of diffraction peaks: one of them corresponds to iron austenite, the other one with a shift to the lower angle corresponds to iron nitride austenite, as shown by the insert of Figure 5-4b. The diffraction peaks of iron nitride austenite shift to the lower angle compared to the virgin austenite, because the interstitial nitrogen atoms

stretch the fcc lattice. Consequently, the lattice constant of the iron nitride austenite is increased.

In conclusion, RNRA, CEMS and XRD measurements independently revealed the nitrogen concentration and iron nitride phase composition. Together they give an overall picture of the phase evolution during the annealing process in vacuum.

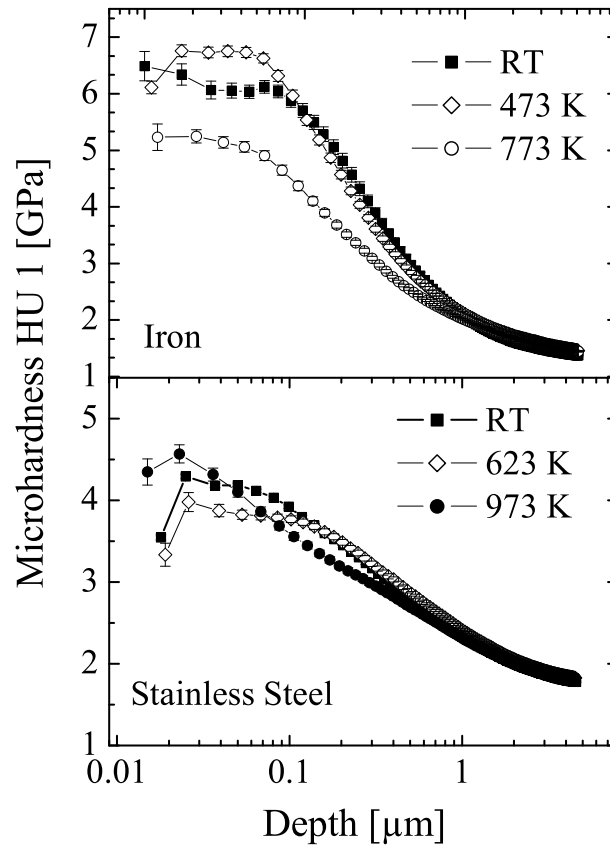


Figure 5-5: Microhardness measurement of excimer laser nitrided iron and stainless steel annealed in vacuum.

The nanoindentation technique is used to test the hardness of the surface layer during the annealing treatment. Figure 5-5 shows the surface microhardness profiles of iron and stainless steel up to 9 μm . For stainless steel, the hardness remains nearly constant. For the iron sample, the surface hardness is correlated to the nitrogen concentration and decreases with increasing annealing temperature. The phase

transition is the main mechanism contributing to this behavior. It is well known that the hardness of the hexagonal ϵ iron nitride (7.1 GPa) is much higher than that of the bcc ferrite (2.8 GPa) [82], depletion of ϵ iron nitride with increasing temperature results in reduced hardness.

5.1.2 In air atmosphere

In addition to the annealing experiment conducted in vacuum, we were also interested in annealing experiments in air, since this is the normal situation for most industrial applications. Figure 5-6 shows the nitrogen depth profiles in iron and stainless steel samples annealed in air. From these RNRA results, it is clear that the nitrogen content in stainless steel is more stable than in iron, similar to the annealing experiment results in vacuum.

The evolution of the nitrogen content is mainly determined by two mechanisms: the diffusion process and the degassing kinetics. It is well known that the diffusion coefficient of nitrogen in γ - Fe(N) is much smaller than in α - Fe. Since the principal structure of stainless steel is γ - Fe, nitrogen atoms in stainless steel are more difficult to transport than in α - Fe. This is the reason why up to 473 K, there is still hardly no change in the nitrogen concentration of stainless steel. For iron, the situation is different. Within the first 100 nm, the nitrogen content drops drastically around 573 K. However, in depths below 100 nm, the nitrogen concentration even increases slightly. It is impossible to explain this behavior only by the simple diffusion mechanism in homogeneous bulk material. Another fact has to be taken into account: typically the iron sample after laser irradiation has polycrystalline structure, the grain boundary diffusion becomes the dominant diffusion mechanism. CEMS revealed that most nitrogen enriched phases such as the ϵ and the γ' iron nitride phases are distributed in the first 150 nm. From RNRA and XRD, we assumed that the γ iron nitride phase is dominant with a mean nitrogen concentration of around 10 at.% between the substrate α -Fe and the surface. Taking a look at the CEMS spectrum in Figure 5-2, the

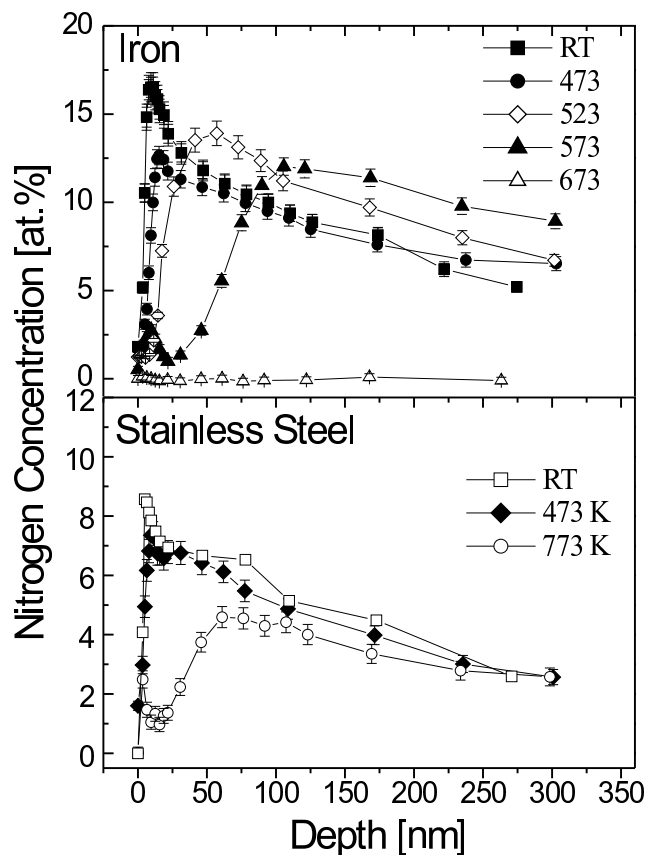


Figure 5-6: Nitrogen depth profiles for excimer laser nitrided iron and stainless steel annealed in air.

line width of the ϵ iron nitride phases is much broader than that of the γ phase. This means that the mean grain size of iron nitrides is smaller in the surface than in the depths of the nitrided layer. In other words, the grain boundaries are more densely distributed in the surface. Consequently, the nitrogen atoms with the maximum concentration in the surface are difficult to diffuse deeper and gradually accumulate in depths below 100 nm. If the annealing temperature exceeds 673 K, the degassing mechanism begins to play an important role in the nitrogen depletion process. Since at ambient pressure all iron nitrides are thermodynamically unstable compared to Fe and N_2 , the limitation for the decomposition reaction $Fe_xN \rightarrow xFe + \frac{1}{2}N_2$ is due to the kinetic barriers of the degassing process, i.e: the recombination of 2 N atoms to 1

N_2 molecule [136]. Only above 673 K, the degassing reaction rate becomes significant and increases very fast with increasing annealing temperature. It is believed that this is the main reason of the rapidly reduced nitrogen content within the depth of 100 nm. At the same time, the diffusion process of nitrogen is greatly enhanced at temperatures above 673 K. Due to the concentration gradient, the nitrogen in depths below 100 nm can easily diffuse both to the surface and to the substrate α -Fe, which results in the depletion of nitrogen in the whole nitrided layer. When the temperature reaches 973 K, no nitrogen left for both of iron and stainless steel. It also worth a mention that the nitrogen content in iron drops more quickly in air than in vacuum. This is possibly due to the iron oxide layer which developed from the surface. In order to confirm our assumption, the phase analysis are conducted by XRD and CEMS.

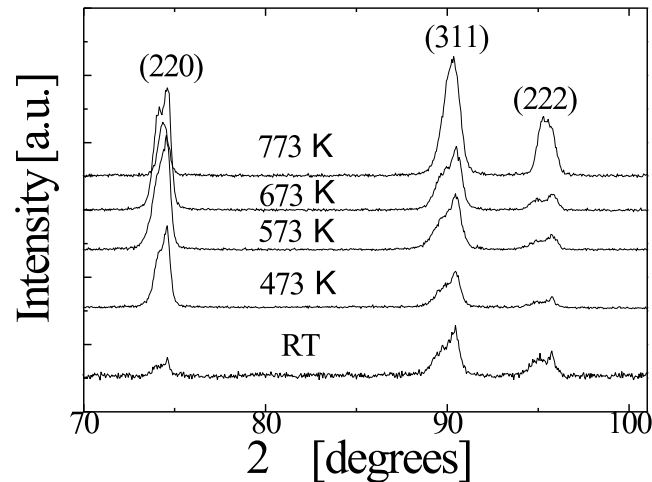


Figure 5-7: GIXRD spectra of excimer laser nitrided stainless steel annealed in air.

Figure 5-7 and Figure 5-8 give the grazing angle incidence X-ray diffraction spectra of stainless steel and iron, respectively. As shown in Figure 5-7 no additional new phases are produced in stainless steel during the whole annealing process in air. For the iron sample, when the annealing temperature reaches 673 K, the iron nitrides disappear completely. At the same time, there are strong diffraction peaks from iron oxides, such as hematite (α - Fe_2O_3) and magnetite (Fe_3O_4).

Figure 5-9a presents the phase composition of the iron sample during the annealing process in air. The phase fractions of iron nitrides and iron oxides are deduced from the CEMS measurements. Oxidation starts from the surface at around 500 K. Then the iron oxides become the dominant phases at 673 K instead of α -Fe. This is clearly demonstrated in the CEMS spectrum shown in Figure 5-9b. Except for the iron oxide formation, the critical temperature of the iron nitride phase evolution in air is the same as for annealing in vacuum. From 473 K, γ' appears, and the dominant iron nitride phase changes from the γ to the γ' phase at 523 K.

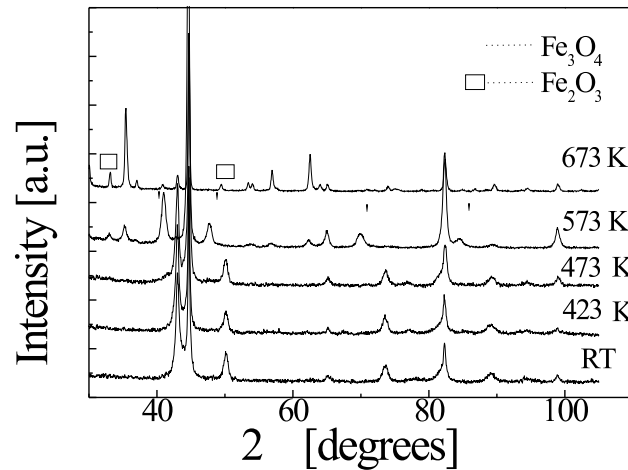


Figure 5-8: GIXRD spectra of excimer laser nitrided iron annealed in air.

Finally, the thermal stability of excimer laser nitrided titanium and Ti:sapphire laser nitrided iron were also investigated. In detail, 2 hours annealing treatment in air environment (at 873 K) was assigned to the excimer laser nitrided titanium to see whether the degassing effect is reduced compared to iron nitride. As for Ti:sapphire laser, the nitrided iron sample was simply stored in RT air atmosphere for two years, and the RNRA measurement is repeated to check the variation of the nitrogen content. If the titanium nitride produced by Ti:sapphire laser is amorphous, the nitrogen content could be quite unstable and a considerable difference would be expected after two years' storage. The nitrogen concentration depth profiles of both samples are

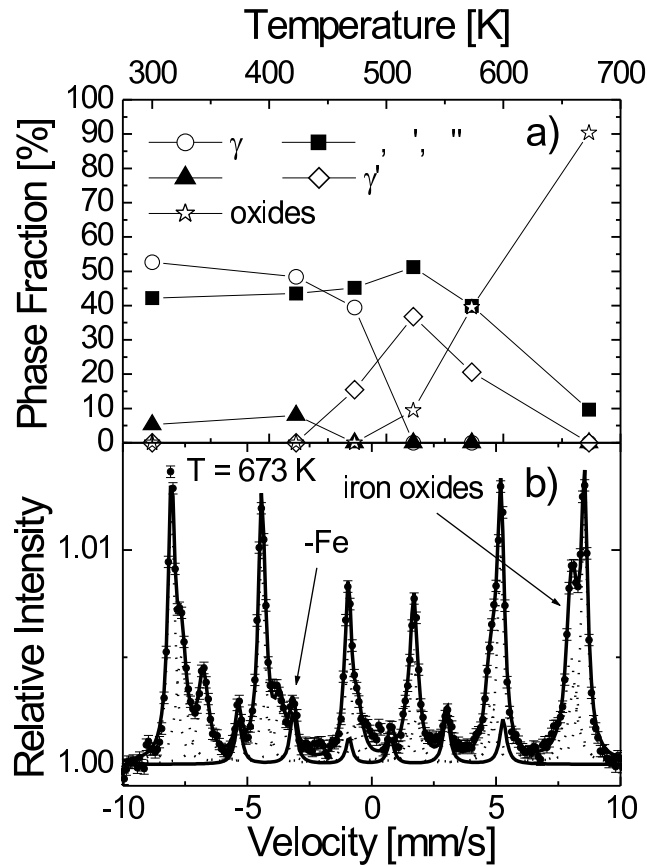


Figure 5-9: (a) Phase composition of excimer laser nitrided iron annealed in air as revealed by CEMS analysis; (b) CEMS spectrum of the excimer laser nitrided iron annealed in air at 673 K.

illustrated in Figure 5-10. The original nitrogen concentration profiles just after the laser preparation are also plotted as comparison.

After 2 hours annealing treatment at 873 K in air environment, the nitrogen content in the first 200 nm of excimer laser nitrided titanium drops considerably due to degassing effect. However, in depth of more than 200 nm, the titanium sample still maintains a high nitrogen concentration close to 30 at.%, nearly the same value as that before the annealing treatment. Compared to the laser nitrided titanium, excimer laser nitrided iron sample has already lost all of its nitrogen even at the temperature of 773 K. The big difference in nitrogen depletion behaviour offers strong evidence to the suppressed degassing effect in titanium nitride.

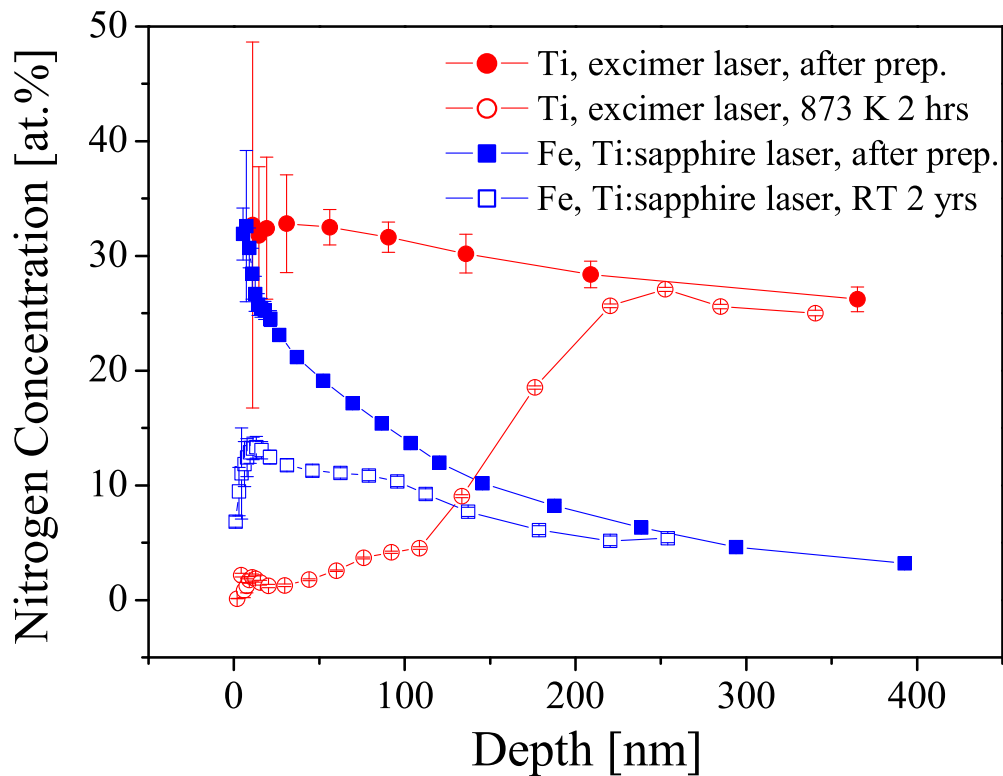


Figure 5-10: The evolution of the nitrogen depth profile of excimer laser nitrated titanium (annealed in air at 873 K for 2 hours) and Ti:sapphire laser nitrated iron (2 years in RT air atmosphere).

After two years in the RT atmosphere, the repeated RNRA measurement of fs Ti:sapphire laser nitrated iron revealed a significant change of the nitrogen content profile, the maximum concentration drops to merely half of the initial value. If the iron nitride is in normal crystalline state, 2 years' storage would not induce such a depletion of the nitrogen content. Only unstable amorphous or nanocrystalline iron nitrides could explain the remarkable missing of the nitrogen content in RT environment.

In summary, the thermal stability of laser produced iron and titanium nitrides by annealing treatment conducted both in vacuum and air was investigated. The de-

tailed information on the evolution of the nitrogen concentration, phase composition and abundance, surface hardness *vs* annealing temperature is derived by combining methods of ion beam analysis (nitrogen profile), Mössbauer spectroscopy, grazing angle X-ray diffraction (phase analysis) and nanoindentation measurement (surface hardness). Stainless steel proved to be more stable than the iron sample. No oxides or new iron nitride phases are produced up to 973 K. There are two critical temperatures for the iron samples during the annealing process. At 523 K, the dominant iron nitride phase changes from the γ to the γ' phase. When $T > 773$ K, there are no iron nitride phases left and the surface is oxidized when annealed in air. The different behavior of iron and stainless steel is due to the phase transition and diffusion mechanism. When $T > 973$ K, all iron nitride phases disappear from iron and stainless steel, which corresponds to the maximum temperature for possible future industrial applications of laser nitriding of iron. Annealing experiment of excimer laser nitrided Ti confirms the suppressed degassing effect in titanium nitrides, resulting in an improved FEL nitriding efficiency of Ti. In consistent with the previous phase analysis, the amorphous or nanocrystalline iron nitrides produced by fs Ti:sapphire laser are unstable even in RT atmosphere.

Chapter 6

Conclusions and outlook

6.1 Conclusions

From the investigations of the influences of the ambient nitrogen pressure and the laser pulse duration on the laser nitriding process, the most important conclusions are summarized as follows:

1: The role of laser plasma and the plasma dynamics

The laser plasma plays a critical role in laser nitriding, which effectively enhances the laser-metal thermal coupling. Although during the laser irradiation the plasma screens the incident laser beam from the metal surface, after extinction of the laser pulse, part of the absorbed energy is fed back to the nitrided metal by blackbody-like radiation and thermal conduction, which can eventually improve the laser-metal coupling time and the nitrogen diffusion time for efficient laser nitriding. The laser plasma dynamics is strongly influenced by the ambient pressure. In the nitrogen pressure series, the transition from laser ablation to nitrogen diffusion dominated regime with increasing nitrogen pressure is clearly demonstrated. The characteristic parameters of the nitrogen depth profile were extracted from the single pulse experiments, whose nitrogen pressure dependence was partially interpreted based on the LSC wave model. Two fundamental time parameters, namely, the iron melting time t_m and the

plasma iron effective coupling time t_c , were deduced from the ^{15}N isotopic experiments. The difference between them suggests that the laser nitriding process doesn't start simultaneously as the laser irradiation, which is also qualitatively explained by the spatial and temporal structure of the laser plume. More generally, as revealed in the pressure series, the nitriding efficiency increases rapidly as the nitrogen pressure increases up to 2 bar. From 2 bar to 10 bar, the nitrogen concentration remains more or less constant or decreases slowly. The optimal nitrogen pressure window for laser nitriding lies between 2 and 3 bar. In the high pressure region, gas breakdown probably hinders the further improvement of the nitriding efficiency.

2: Laser nitriding mechanisms.

Both the experimental results and the thermal simulation of the pulsed laser series confirmed a general rule: long pulsed laser achieves a better nitriding efficiency. It is believed that a well developed nitrogen diffusion process in molten metals is the primary mechanism of laser nitriding. Ns laser with 10^8 W/cm^2 intensity maintains a considerable long melting time and a deep molten depth as well as the effect of plasma enhanced laser-metal thermal coupling (the nitriding efficiency is nearly independent of the incident laser wavelength), make it superior for efficient nitriding treatment compared to ps or fs laser. The fs Ti:sapphire laser must have other nitriding mechanisms, since the 400 nm thick iron nitride layer with a mean nitrogen concentration of around 16 at.% cannot be attributed to the nitrogen diffusion due to the ultra short pulse duration and the thermal diffusion length. Most probably the ablated iron ions react directly with nitrogen to form FeN molecules or clusters in the laser plume, then the molecules or clusters are re-deposited on iron by plasma condensing to form an amorphous or nanocrystalline phase, which unfortunately has low hardness and poor thermal stability. Furthermore, the pulsed laser series revealed that the laser nitriding efficiency is essentially determined by the competing between nitrogen take up (nitrogen diffusion) and nitrogen depletion (degassing effect). The degassing rate increases exponentially with the surface temperature of molten metal. High inten-

sity FEL (which resembles a μs or CW laser due to the 10^7 repetition rate of FEL micropulses) greatly enhances the nitrogen degassing rate in iron, resulting in an extremely low nitriding efficiency. Another factor influencing the degassing rate is the chemical activity of metal with nitrogen. By the comparison between FEL nitrified iron and titanium and the annealing experiments, it is clear that the high chemical reactive metals such as titanium, are more favorable material for laser nitriding due to reduced degassing effect.

6.2 Outlook

First of all, all the investigations of the present work were limited to the analysis of the nitrified samples after the laser irradiation had been done. *In situ* or real time monitoring of the nitriding process is valuable to probe the plasma temperature, electron and ion density, plasma absorption and propagation, as well as surface temperature and molten depth of irradiated materials, which are critical to understand the physics of laser-plasma- material interactions [138, 139, 140, 141]. A schematic drawing of the experimental setup for the future *in situ* measurements is illustrated in Figure 6-1.

The *in situ* experiments will concentrate on the characterization of the laser plasma and metal surface state during the nitriding process. For ns excimer laser, a fast response ICCD camera triggered by the incident laser pulse directly images the plasma plume with high spatial resolution [126, 142]. A supersonic pinducer connected with a digital oscilloscope is employed to detect the photoacoustic signal and monitor the ablation depth of metal in real time [143]. As pulse duration approaches ps or fs, in order to achieve the corresponding high time resolution, pump probe technique is adopted to trace the ultra fast process. The principal is to apply a excitation pump pulse first, to induce the laser plasma, after a fine control of the time delay, a second pulse arrives to probe the plasma dynamics. The ultra fast time resolution is

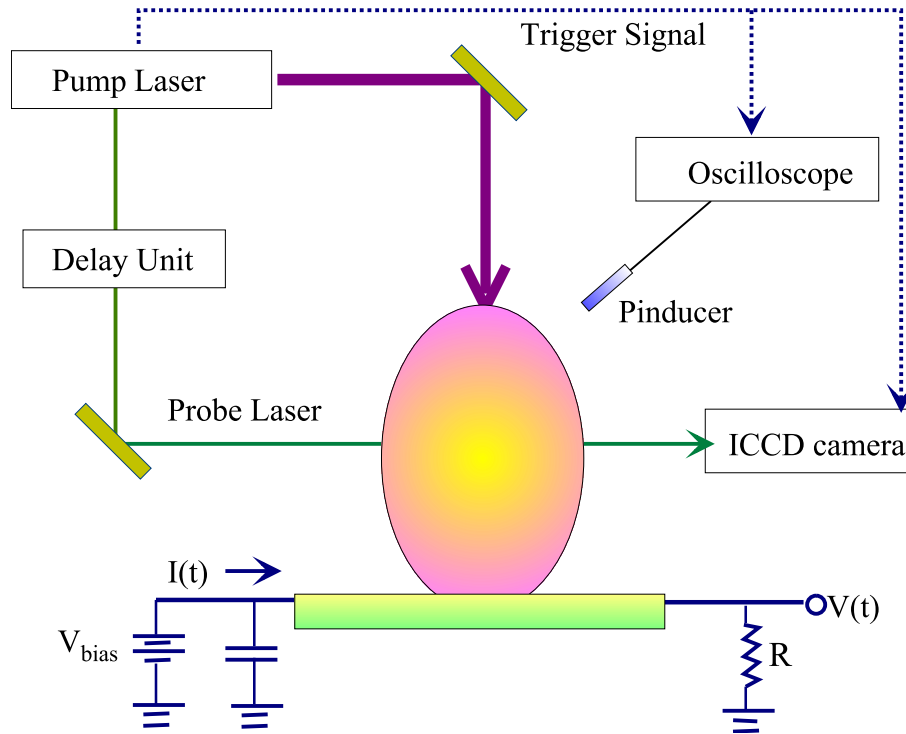


Figure 6-1: Schematic drawing of *in situ* experimental configurations with the aim of probing plasma properties and metal surface state during laser nitriding process.

achieved by simply adjust the optical path difference between the pump and probe pulse. For example, the 0.03 mm distance would produce a extremely short 100 fs delay.

The previous chapters revealed that the surface molten state is necessary for efficient laser nitriding. The thickness and the melting time of the surface molten layer are reflected by the resistance variation during the melting process. The experimental setup as shown in the lower part of Figure 6-1 was first proposed by Aziz [144, 145, 146], and proved to to successful in the ns region.

Secondly, I am thinking of the multibeam laser nitriding configurations [137] for optimal laser-metal energy couplings. The idea is to apply a short ps or ns pulsed laser with the intensity much higher than the surface evaporation threshold, to trigger the laser plasma. Then followed by a μs or CW laser with lower intensity but longer pulse duration, to maintain the necessary temperature and surface pressure of laser

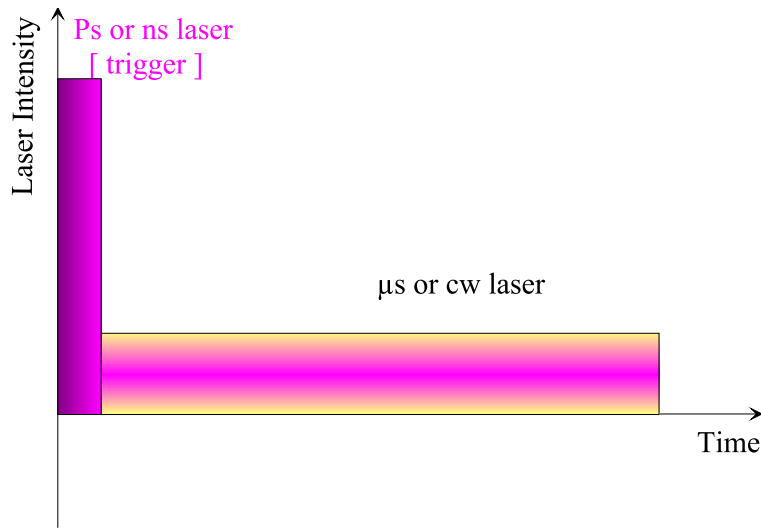


Figure 6-2: Schematic drawing of the idea of multi-beam pulsed laser nitriding for optimal laser-metal energy coupling.

produced plasma but does not induce plasma breakdown or overheating of the nitrided sample. The undesired depletion of nitrogen due to the extremely high surface temperature and the amorphous structure of surface layer induced by the ultra fast cooling can be avoided. The idea is more clearly presented in Figure 6-2.

Bibliography

- [1] P. Schaaf, Progress in Materials Science **47**, 1(2002).
- [2] *Metal Handbook*, ninth Edition, Vol.4, American Society for metals, Metals park, Ohio, 1978.
- [3] S. K. Chen, S. Jin, T.H. Tiefel, Y.F. Hsieh, E. M. Gyorgy and D.W.Johnson Jr., J. Appl. Phys. **70**, 6247(1991).
- [4] T. Weber, L. De Wit, F. W. Saris, A. Königer, B. Rauschenbach, G.K.Wolf and S. Krauss, Mater. Sci. Eng. **A 199**, 205(1995).
- [5] H. A. Wriedt, N. A. Gokcen, and R. H. Nafziger, Bulletin of Alloy Phase Diagrams **8**, 355(1987).
- [6] A. F. Guillemeret and H. Du. Z. Metallkunde **85**, 154(1994).
- [7] J. Kunze, *Nitrogen and carbon in iron and steel*, Akademie Verlag, Berlin, 1990.
- [8] G. Marest, def. Diff. Forum, **57/58**, 273(1998)
- [9] B. Rauschenbach and A. Kolitsch, Phys. Status Solidi **A 80**, 211(1983)
- [10] B. Rauschenbach, A. Kolitsch and K. Hohmuth, Phys. Status Solidi **A 80**, 471(1983)
- [11] F. Bodart, G. Terwagne and M. Piette, Mater. Sci. Eng., **90**, 111(1987)

- [12] G. Terwagne, M. Piette, F. Bodart and W. Möller, *Mater. Sci. Eng.*, **115**, 25(1989)
- [13] G. Terwagne, M. Piette, P. Bertrand and F. Bodart, *Mater. Sci. Eng.*, **B 2**, 195(1989)
- [14] J. Jagielski, N. Moncoffre, G. Marest, L. Thome, A. J. Barcz, G. Gawlik and W. Rosinski, *J. Appl. Phys.* **75**, 153(1994)
- [15] A. M. Vredenberg, C. M. Perez-Martin, J. S. Custer, D. O. Boerma, L. de Wit, F. W. Saris, N. M. van der Pers, T. H. de Keijser and E. J. Mittemeijer, *J. Mater. Res.*, **7**, 2689 (1992)
- [16] J. R. Conrad, J. L. Radtke, R. A. Dodd, F. J. Worzala and N. C. Tran, *J. Appl. Phys.* **62**, 4591(1987)
- [17] G. A. Collins, R. Hutchings, J. Tendys and M. Samandi, *Surf. Coat. Technol.*, **68/69**, 285(1994)
- [18] W. Ensinger, *Nucl. Inst. and Meth. B* **120**, 270(1996)
- [19] VDI, *VDI-Lexikon Werkstofftechnik* (VDI Verlag, Düsseldorf, 1990).
- [20] R. W. Cahn and P. Haasen, *Physical Metallurgy* (North-Holland Physics Publishing, Amsterdam - Oxford - New York - Tokyo, 1983).
- [21] N. Bloembergen, *Rev. Mod. Phys.* **71**, S283 (1999).
- [22] I. W. Boyd, *Laser Processing of Thin Films and Microstructures, Springer Series in Materials Science* Springer Verlag, Berlin, Heidelberg, 1987.
- [23] P. R. Willmott, J. R. Huber *Rev. Mod. Phys.* **72**, 315 (2000).
- [24] J. C. Miller, *Laser Ablation, Springer Series in Materials Science* Springer Verlag, Berlin, Heidelberg, 1994.

- [25] P. Schaaf, C. Illgner, M. Niederdrenk and K. P. Lieb, *Hyperfine Interactions* **95**, 199 (1995).
- [26] S. B. Ogale, P. P. Patil, D. M. Phase, Y. V. Bhandarkar, S. K. Kulkarni, S. Kulkarni, S. V. Ghaisas, S. M. Kanetkar, V. G. Bhide, and S. Guha, *Phys. Rev. B* **36**, 8237 (1987).
- [27] E. D'Anna, M. L. De Giorgi, G. Leggieri, A. Luches, M. Martino, A. Perrone, I. N. Mihailescu, P. Mengucci, and A. V. Drigo, *Thin Solid Films* **213**, 197 (1992).
- [28] J. Barnikel, K. Schutte, and H. W. Bergmann, *Härterei-Technische Mitteilungen* **52**, 91 (1997).
- [29] M. Han, E. Carpena, F. Landry, K.-P. Lieb, and P. Schaaf, *J. Appl. Phys.* **89**, 4619 (2001).
- [30] P. Schaaf, M. Han, K.-P. Lieb and E. Carpena, *Appl. Phys. Lett.* **80**, 1091 (2002).
- [31] M. Han, F. Landry, P. Schaaf, *Appl. Phys.* **A69**, S795 (1999).
- [32] P. Schaaf, F. Landry, M. Han, K.-P. Lieb, *Hyperfine Interactions* **126**, 211 (2000).
- [33] P. Schaaf, F. Landry, M. Han, E. Carpena, K.-P. Lieb, *Hyperfine Interactions*, in print (2001).
- [34] C. Illgner, Ph.D. thesis, University of Göttingen, 1996.
- [35] F. Landry, Ph.D. thesis, University of Göttingen, 2000.
- [36] L. Russian, Ph.D. thesis, University of Göttingen, 2000.
- [37] E. Carpena, Ph.D. thesis, University of Göttingen, 2002.
- [38] L. C. Feldmann, J. W. Mayer. *Fundamentals of Surface and Thin Film Analysis*, Elsevier, New York, 1986.

- [39] J. R. Tesmer and M. Nastasi, editors, *Handbook of Modern Ion Beam Materials Analysis*, MRS, Pittsburgh, Pennsylvania, 1995.
- [40] K. Bethge, F. Rauch, and P. Misaelidis, Nucl. Inst. and Methods B **50**, (1990).
- [41] M. Uhrmacher, K. Pampus, F. J. Bergmeister, D. Purshke, and K.-P. Lieb, Nucl. Inst. and Methods **B 9**, 234 (1985).
- [42] W. K. Chu, J. W. Mayer, and M. A. Nicolet. *Backscattering Spectrometry*, Academic Press, Orlando, Florida, 1978.
- [43] N. Bohr, Mat. Fys. Medd. Dan. Vid. Selsk., **18**, 8(1948).
- [44] J. F. Ziegler, J. P. Biersack, and U. Littmark. *The Stopping and Range of Ions in Solids* Pergamon Press, New York, 1985.
- [45] H. H. Andersen and J. F. Ziegler, *Hydrongen Stopping Powers and Ranges in all Elements* Pergamon Press, New York, 1985.
- [46] J. F. Ziegler, *Helium Stopping Power and Ranges in all Elements* Pergamon Press, New York, 1985.
- [47] J. F. Ziegler, *Stopping Cross-sections for Energetic Ions in all Elements* Pergamon Press, New York, 1985.
- [48] J. F. Ziegler and J. M. Manoyan. Nucl. Inst. and Methods **B 35**, 215 (1988).
- [49] L. R. Doolittle, Nucl. Inst. and Methods **B 9**, 344 (1985).
- [50] L. R. Doolittle, Nucl. Inst. and Methods **B 15**, 227 (1986).
- [51] J. Saarilahti, Nucl. Inst. and Methods **B 64**, 734 (1992).
- [52] J. P. Biersack, IBA, PC programm Package IBA, 1997
- [53] RBX, University of Budapest, PC programm Package RBX, 1992

- [54] M. Mayer. Technical Report MPI for Plasmaphysics, SIMNRA, IPP 9/113, 1997.
- [55] H. Damjantschitsch, M. Weiser, G. Heuser, S. Kalbitzer and H. Mannsperger. Nucl. Inst. and Methods **218**, 129 (1983).
- [56] B. Maurel and G. Amsel, Nucl. Inst. and Methods **218**, 159 (1983).
- [57] P. H. LaMarche, W. A. Lanford and K. Golub, Nucl. Inst. and Methods **189**, 533 (1981).
- [58] B. Maurel, PhD thesis, Universite de Paris VII, 1980.
- [59] B. Maurel, G. Amsel and J. P. Nadai, Nucl. Inst. and Methods **197**, 1 (1982).
- [60] I. Vickridge and G. Amsel, Nucl. Inst. and Methods **B 45**, 6 (1990).
- [61] T. Osipowicz, K. P. Lieb and S. Brüssermann, Nucl. Inst. and Methods **B 18**, 232 (1987).
- [62] W. H. Bragg and R. Kleeman, Philos. Mag., **10**, 318 (1905).
- [63] K. -P. Lieb, F. Bergmeister, T. Osipowicz, K. Pampus, and M. Uhrmacher. The Göttingen Ion Implanter IONAS, a versatile Tool for Nuclear Solid State Studies. In K. -P. Lieb and M. Uhrmacher, editors, *Solid State Reactions after Ion Implantation Detected by Nuclear Methods*, Göttingen, (1986) p. 191.
- [64] K. -P. Lieb, W. Bolse, T. Corts, A. Kehrel, M. Uhrmacher, and T. Weber. Depth profiling of Nitrided Surface Layer by Resonant Nuclear Reaction Analysis. In E. Brosszeit et al., editors, *Plasma Surface Engineering*, DGM informationsgesellschaft, Oberursel, (1989) p. 1055.
- [65] K. -P. Lieb, Characterization of solid state reactions in thin films by nuclear methods. In J. Stanek, editor, *Proceedings of the XXIV Zakapane School of Physics 1990*, World Scientific, Singapore, (1990) p. 108.

- [66] F. Landry and P. Schaaf, Nucl. Inst. and Methods **B 179**, 262 (2001).
- [67] W. H. Press, S. A. Teukosky, W. T. Vetterling and B. P. Flannery, *Numerical Recipes in C*, Cambridge University Press, New York, 1992.
- [68] T. Kacsich, M. Niederdrenk, P. Schaaf, K.-P. Lieb, U. Geyer, and O. Schulte, Surface and Coatings Technology **93**, 32 (1997).
- [69] G. K. Wertheim, *Mössbauer effect: Principles and Applications*, Academic Press, New York and London, 1964.
- [70] L. May, Editor, *An Introduction to Mössbauer Spectroscopy*, Plenum Press, New York-London, 1971.
- [71] R. L. Mössbauer, Z. Physik, **151**, 124 (1958).
- [72] R. L. Mössbauer, Naturwissenschaften **45**, 538 (1958).
- [73] R. L. Mössbauer, Science **137**, 731 (1962).
- [74] P. Schaaf, A. Krämer, L. Blaes, G. Wagner, F. Aubertin, and U. Gonser, Nucl. Instrum. and Methods **B 53**, 184 (1991).
- [75] P. Schaaf, T. Wenzel, K. Schemmerling, and K.-P. Lieb, Hyperfine Interactions **92**, 1189 (1994).
- [76] F. Landry and P. Schaaf (unpublished).
- [77] B. E. Warren, *X-ray Diffraction*, Dover Publications INC. New York, 1990
- [78] B. D. Cullity, *Elements of X-ray diffraction*, Addison-Wesley, Reading, Massachusetts, 1978.
- [79] E. F. Kaelble, *Handbook of X-rays*, McGraw-Hill, New York, 1967.
- [80] G. K. Williamson, W. H. Hall, Acta Metall. **1**, 22 (1953).

- [81] D. Bäuerle, *Laser Processing and Chemistry, Springer Series in Materials Science* (Springer Verlag, Berlin, Heidelberg, 1996).
- [82] P. Schaaf, F. Landry, M. Han, E. Carpenne, K.-P. Lieb, *Hyperfine Interactions* (2002), in print.
- [83] P. Schaaf, F. Landry, M. Neubauer, and K.-P. Lieb, *Hyperfine Interactions* **113**, 429 (1998).
- [84] C. Illgner, P. Schaaf, K.-P. Lieb, R. Queitsch, and J. Barnikel, *J. Appl. Phys.* **83**, 2907 (1998).
- [85] F. Landry, M. Neubauer, K.-P. Lieb, and P. Schaaf, in *Proc. European Conference of Laser Treatment of Materials, EKLAT 1998, September 1998, Hannover*, edited by B. L. Mordike (Werkstoff-Informationsgesellschaft, Frankfurt, 1998), pp. 81–86.
- [86] F. Landry, P. Schaaf, M. Neubauer, and K.-P. Lieb, *Appl. Surf. Sci.* **138-139**, 266 (1999).
- [87] F. Landry, K.-P. Lieb, and P. Schaaf, *J. Appl. Phys.* **86**, 168 (1999).
- [88] P. Schaaf, F. Landry, and K. -P. Lieb, *Appl. Phys. Lett* **74**, 153 (1999).
- [89] E. Carpenne, F. Landry, and P. Schaaf, *Appl. Phys. Lett* **77**, 2412 (2000).
- [90] W. C. Oliver and G. M. Pharr, *Journal of Materials Research* **7**, 1564 (1992).
- [91] E. Fromm, H. Jehn, W. Hehn, H. Speck, and G. Hörz. *Gases and Carbon in Metals (Thermodynamics, Kinetics, and Properties): Iron-Nitrogen*, Volume XV of *Physik Daten*, FIZ Energie, Physik, Mathematik, Karlsruhe, 1982.
- [92] S. J. Campbell, W. A. kaczmarek and M. Hofmann, *Hyperfine Interactions* **126**, 175 (2000).

- [93] M. Kopcewicz, J. Jagielski and A. Turos, J. Appl. Phys. **71**, 4217 (1992).
- [94] J. Jagielski and M. Kopcewicz, J. Appl. Phys. **88**, 673 (2000).
- [95] L. de Wit, T. Weber, J. S. Custer and F. W. Saris, Phys. Rev. Lett **72**, 3835 (1994).
- [96] A. L. Sozinov, A. G. Balanyuk and V. G. Gavriljuk, Acta Mater **47**, 927 (1999).
- [97] S. R. Chen, H. A. Daives and W. M. Rainforthj, Acta Mater **47**, 4555(1999).
- [98] A. G. Balanyuk, V. G. Gavriljuk, V. N. Shivanyuk, A. I. Tyshchenko and J. C. Rawers, Acta Mater **47**, 3813 (1999).
- [99] O. Öztük and D. L. Williamson, J. Appl. Phys. **77**, 3839 (1995).
- [100] V. M. Nadutov, Mater. Sci. Eng. **A 254**, 234 (1998).
- [101] E. Marzur, Spectroscopy and Dynamics of collective Excitations in Solids, B. Di Bartolo, editors, NATO ASI series, Plenum, 1996.
- [102] M. V. Allmen and A. Blatter, *Laser Beam Interactions with Materials, Springer Series in Materials Science*, Springer Verlag, Berlin, Heidelberg, 1995.
- [103] P. P. Pronko, S. K. Dutta, and D. Du, J. Appl. Phys. **78**, 6233(1995).
- [104] J. Crank, *The Mathematics of Diffusion*, Oxford University Press, London, 1956.
- [105] A. N. Pirri, R. G. Root, and P. K. S. Wu, AIAA Journal.**16**, 1296(1978).
- [106] A. N. Pirri, R. G. Root, and P. K. S. Wu. AIAA Journal, **5** 1597(1977)
- [107] A. N. Pirri, The Physics of Fluid **16**, 1435(1973).
- [108] Y. P. Raizer, JETP **31**, 1148(1970).

- [109] Y. P. Raizer, JETP **21**, 1009(1969).
- [110] Y. P. Raizer, *Gas Discharge Physics*, Springer Verlag, Berlin, Heidelberg, 1997.
- [111] R. K. Singh and J. Narayan, Phys. Rev. B **41**, 8843(1990).
- [112] N. Arnold, J. Gruber, J. Heitz, Appl. Phys. **A69**, 87(2000).
- [113] L. I. Sedov, *Similarity and Dimensional Methods in Mechanics*, Infosearch LTD, London, 1959.
- [114] L. D. Landau and E. M. Lifshitz, *Course of Theoretical Physics, VI. Fluid Mechanics*, Pergamon Press, New York, 1987.
- [115] J. P. Reilly, A. Ballantyne, and J. A. Woodroffe, AIAA J. **17**, 1098(1979).
- [116] W. W. Duley, *UV Lasers: effects and applications in material science*, Cambridge University Press, 1996.
- [117] A. Gupta, B. Braren, K. G. Casey, B. W. Hussey, and R. Kelly, App. Phys. Lett. **59**, 1302(1991).
- [118] J. D. Fast, *Interaction of Metals and Gases Vol. 1*, Philips Technical Library, 1965.
- [119] R.G.Root. Modeling of Post-Breakdown Phenomena. In L. J. Radzinski and D. A. Cremers, editors, *Laser-Induced Plasmas and Applications*. Marcel Dekker Inc., New York and Basel, 1992
- [120] Y.A. Zel'dovich and Yu. P. Raiser, *Physics of Shock Waves and High Temperature Hydrodynamics Phenomena* (Academic, New York, 1966), Col. I, pp. 93-101.
- [121] D.A. Freiwald, J. Appl. Phys. **43**, 2224(1972).

- [122] R. F. Wood, J. N. Leboeuf, D. B. Geohegan, A. A. Puretzky, and K. R. Chen, Phys. Rev. B **58**, 1533 (1998).
- [123] K. R. Chen, T. C. King, J. H. Hes, J. N. Leboeuf, D. B. Geohegan, R. F. Wood, Phys. Rev. B **60**, 3873 (1999).
- [124] X. Mao, W. T. Chan, M. Caetano, M. A. Shannon, and R.E. Russo, Appl. Surf. Sci. **96 - 98**, 125 (1996).
- [125] W. Pietsch, J. Appl. Phys. **79**, 1250 (1996).
- [126] S. S. Mao, X. Mao, R. Greif, and R. E. Russo, Appl. Phys. Lett **77**, 2464 (2000).
- [127] K. Sokolowski-Tinten, J. Bialkowski, A. Cavalleri, D. Von der Linde, A. Oparin, J. Meyer-ter-Vehn and S. I. Anisimov, Phys. Rev. Lett. **81**, 224 (1998).
- [128] T. D. Bennett, D. J. Krajnovich, and C. P. Grigoropoulos, Phys. Rev. Lett **76**, 1659 (1996).
- [129] V. Schmidt, W. Husinsky and G. Betz, Phys. Rev. Lett. **85**, 3516 (2000).
- [130] P. L. Morton, SLAC-PUB-3176, August (1983).
- [131] L. Rissanen, M. Neubauer, K.-P. Lieb, and P. Schaaf, J. Alloys Comp. **274**, 74 (1998).
- [132] Y. Yamada, H. Shimasaki, Y. Okamura, Y. Ono, and K. Katsumata, Applied Radiation and Isotopes **54**, 21 (2001).
- [133] I. N. Mihailescu, N. Chitica, and J. Hermann etc., J. Appl. Phys. **74**, 5782 (1993).
- [134] E. D'Anna, G. Leggieri and S. Ganatsios etc., J. Appl. Phys. **69**, 1687 (1991).
- [135] J. Pelleg, L. Z. Zevin, S. Lungo and N. Croitora, Thin Solid Films, **197**, 117 (1991).

- [136] D. K. Inia, Ph.D. thesis, University of Utrecht, 1997.
- [137] R. F. Service, *Science* **278**, 2056 (1996).
- [138] R. Jordan and J. G. Lunney, *Appl. Surf. Sci.* **127 - 129**, 968 (1998).
- [139] J. S. Lash, R. M. Gilgenbach, and H. L. Spindler, *J. Appl. Phys.* **79**, 2287 (1996).
- [140] J. Hermann, A. L. Thomann and I. N. Mihailescu, *etc.*, *J. Appl. Phys.* **77**, 2928 (1995).
- [141] M. Hatano, S. Moon, M. Lee, K. Suzuki and C. P. Grigoropoulos, *J. Appl. Phys.* **87**, 36 (2000).
- [142] D. B. Geohegan, A. A. Puretzky, G. Duscher, and St. J. Pennycook, *Appl. Phys. Lett.* **72**, 2987 (1998).
- [143] W. P. Leung and A. C. Tam, *Appl. Phys. Lett.* **60**, 23 (1992).
- [144] J.Y. Tsao, S.T. Picraux, P.S. Peercy and M.O. Thompson, *Appl. Phys. Lett.* **48**, 278 (1986).
- [145] H.A. Atwater, J.A. West, P.M. Smith, M.J. Aziz, J.Y. Tsao, P.S. Peercy and M.O. Thompson, *Mater. Res. Soc. Symp. Proc.* **157**, 369 (1990).
- [146] P.M. Smith and M.J. Aziz, *Acta Metall. Mater.* **42**, 3515 (1994).

Acknowledgement

First of all I would like to give my sincere thankfulness to Prof. Klaus-Peter Lieb, my supervisor, for his many suggestions, critical insights, constant supports and growing interests during this research.

I am very indebted to Dr. Peter Schaaf, for his guidance through the early years of chaos and confusion. He always provided a motivating, enthusiastic, and critical atmosphere in many of our discussions and in our group's Tuesday meetings.

Needless to say, that I am grateful to all of my colleagues at the II. Physics Institute. Among them are my close Chinese friend Kun Zhang, he gave me plenty of generous helps, and the energetic Ettore Carpane, who always be ready to produce new ideas and jokes at any time. Steffen Wagner is very helpful in many of my laser experiments, I also enjoy a lot from the Kicker game with him. The past group alumni Dr. Felix Landry and Dr. Leena Rissanen are really very "nett", I can never forget them. I would say lots of thanks to Dr. Sankar Dhar, Alexander Müller, Galindo Edgar, Marius Hausmann and the cheerful ladies of Stanislawa Gasiorek and Annika Lohstroh, they produced a wonderful atmosphere.

Special thanks to Marcus Schwickert, for his hard work in maintaining the whole computer system in our institute, also for his excellent problem solving skills in tracing the leaks in the Magnetron sputtering chamber.

I want to thank all of the coworkers in the workshop, they have unbelievable patience and sophisticated skills to fix so much defects that last in the past years. I am particularly indebted to Detlef Purschke, he spends so many hours with me in the noisy IONAS but always produce the best beam quality.

The *Volkswagen Fellowship*, which was awarded to me for the period 1999–2001, also the financial aids from SFB345, were crucial to the successful completion of the Ph.D project. I am very grateful to DAAD (Deutscher Akademischer Austauschdienst) for their friendly and efficient supports.

I am so grateful to my parents, also my wife's parents for their continuous encouragement and *love*. Especially my dear wife, LIU Man, who makes the rough time bearable, and the good time great. Without them surely that I could not achieve anything. I agree with Richard Feynman: "Physics is not the most important thing. Love is".

Han Meng

October 1, 2001

Curriculum Vitae

Personal Data

- *name*: Meng HAN
- *place and date of birth*: Ruzhou, P.R.China, 05.Dec.1972
- *citizenship*: P.R.China
- *marital status*: married

Education

- 1978 - 1983 Primary school (Luozhou affiliated school)
- 1983 - 1986 Middle school (Luozhou affiliated school)
- 1986 - 1990 High school (Ruzhou No.1 high school)
- 1990 - 1994 B.S. in Physics, Lanzhou University, P.R.China
- 1994 - 1998 M.S. in Physics, University of Science and Technology of China(USTC)
- 1998 - 2001 Ph.D student, II. Phy. Inst. University of Göttingen, Germany

Experience and awards

1995 - 1998 Teaching and research assistant in Particle Physics Lab. of USTC

1995 GuangHua Graduate Scholarship

1998 Admitted by Texas A&M University, Houston University with full scholarship

1998 - 2001 Volkswagen Fellowship, 5 of national wide